

# **Fabrication and Characterisation of Ferroelectric Lead Zirconate Titanate and Strontium Bismuth Tantalate Thin Films**

**Dissertation**

zur Erlangung des akademischen Grades

**Doktoringenieur  
(Dr.-Ing.)**

von M.Sc. Serhiy Matichyn

geb. am 14.07.1979 in Rachiw

genehmigt durch die Fakultät für Elektrotechnik und Informationstechnik  
der Otto-von-Guericke-Universität Magdeburg

Gutachter: Prof. Dr. E. P. Burte

Prof. Dr. F. T. Edelmann

Promotionskolloquium am 25. Juli 2006

---

## **Content**

<b>1. Introduction</b>	<b>1</b>
1.1 Purpose of Research	1
1.2 Requirements for the Processing of Ferroelectric Material	1
1.3 Choice of Bottom Electrodes	2
1.4 Objectives of Research	2
<b>2. Fundamentals</b>	<b>3</b>
2.1 Ferroelectric Memories	3
2.2 About Ferroelectric Materials	4
2.3 Writing and Reading Cell Data	9
2.4 Reliability of Ferroelectrics	13
2.4.1 Data Retention Characteristics	13
2.4.2 Fatigue Characteristics	14
2.4.3 Relaxation Characteristics	15
2.5 Crystal Structure of $\text{Pb}(\text{Zr},\text{Ti})\text{O}_3$ (PZT) Films	15
2.6 Strontium Bismuth Tantalate as an Alternative Material for FRAMs	19
2.7 Electrode Materials for Ferroelectric Capacitors	22
<b>3. Liquid Delivery Metalorganic Chemical Vapour Deposition Technique</b>	<b>23</b>
3.1 Introduction	23
3.2 Experimental Equipment	24
3.2.1 Equipment Advantages	26
3.2.2 Equipment Setup	26
3.3 Selection of the Precursors for PZT Film Deposition	28
<b>4. Experimental Procedure</b>	<b>33</b>
4.1 Deposition of Single-Metal-Oxide Films	33
4.2 Deposition of the Ferroelectric Thin PZT Films by LD-MOCVD	35
4.3 LD-MOCVD of the Ferroelectric Thin SBT Films	36
4.4 Fabrication of Substrate Wafers	38
4.4.1 Wet Cleaning of the Silicon Wafers	39
4.4.2 Thermal Oxidation	40

---

4.4.3	<i>Deposition of the TiO<sub>2</sub>/Ir Stack Electrode</i>	41
4.5	<i>Fabrication of Test Devices (Capacitors)</i>	42
4.6	<i>Characterization of Grown Films</i>	43
4.6.1	<i>Structural Properties</i>	43
4.6.1.1	<i>Ellipsometry</i>	43
4.6.1.2	<i>X-ray Photoelectron Spectroscopy (XPS)</i>	44
4.6.1.3	<i>Microstructure</i>	46
4.6.1.4	<i>X-ray Diffraction (XRD)</i>	47
4.6.2	<i>Electrical Properties</i>	48
<b>5.</b>	<b><i>Results and Discussion</i></b>	<b>54</b>
5.1	<i>Lead Zirconate Titanate</i>	54
5.1.1	<i>Growth Kinetics</i>	54
5.1.2	<i>Films Structure</i>	60
5.1.2.1	<i>X-ray Photoelectron Spectroscopy Investigation of the Deposited Films</i>	60
5.1.2.2	<i>Investigation of the Crystal Structure by X-ray diffraction</i>	70
5.1.2.3	<i>Atomic Force Microscopy</i>	74
5.1.3	<i>Electrical Characterization</i>	77
5.1.3.1	<i>Ferroelectric Properties</i>	78
5.1.3.2	<i>Fatigue Properties</i>	83
5.1.3.3	<i>Dielectric Properties</i>	84
5.1.4	<i>Summary</i>	87
5.2	<i>Strontium Bismuth Tantalate</i>	88
5.2.1	<i>Deposition Kinetics</i>	88
5.2.2	<i>Chemical Composition</i>	94
5.2.3	<i>Structural Characterization</i>	96
5.2.4	<i>Electrical Characterization</i>	99
5.2.5	<i>Summary</i>	103
<b>6.</b>	<b><i>Conclusions</i></b>	<b>104</b>
<b>7.</b>	<b><i>References</i></b>	<b>106</b>

---

### ***Physical Symbols and Abbreviations***

SRAM – static random access memory;

DRAM – dynamic random access memory;

FRAM – ferroelectric random access memory;

EEPROM – electrical erasable programmable read only memory;

PZT – lead zirconate titanate;

SBT – strontium bismuth tantalate;

$P_r$  – remanent polarization;

$P_{sat}$  – saturated polarization;

$E_c$  – coercive field;

$Q$  – polarized electric charge;

$V_f$  – voltage applied to the ferroelectric capacitor;

$V_c$  – coercive voltage;

$V_{cc}$  – saturated voltage ;

$Q_s$  – saturated polarization charge;

WL – word line;

BL – bit line;

PL – plate line;

$V_L$  – low voltage;

$V_H$  – high voltage;

$V_{ref}$  – reference voltage;

$V_{BL}$  – voltage applied to the bit line;

$V_{PL}$  – voltage applied to the plate line;

DRO – destructive read out;

NDRO – non-destructive read out;

LD-MOCVD – liquid delivery metalorganic chemical vapor deposition;

$Pb(Et)_4$  – tetraethyllead;

$Zr(OBu^t)_4$  – zirconium tetrabutoxide;

TIP – titan isopropoxide;

BLT – bismuth lanthanum titanate;

1T/1C – one transistor/one capacitor;

IC – integrated circuit;

PLZT – lanthanum doped lead zirconate titanate;

PNZT – niobium doped lead zirconate titanate;

---

SBTN – niobium doped strontium bismuth tantalate;  
Pt – platinum;  
RuO<sub>2</sub> – ruthenium oxide;  
IrO<sub>2</sub> – iridium oxide;  
ABO<sub>3</sub> – perovskite structure, where A and B are metal ions;  
MPB – morphotropic phase boundary;  
ULSI – ultra large scale integration;  
SBN – strontium bismuth niobate;  
CMOS – complimentary metal-oxide-semiconductor;  
RF – radio frequency;  
MOD – metalorganic decomposition;  
LSMCD – liquid source misted chemical deposition;  
AVD – atomic vapour deposition;  
LDS – liquid delivery system;  
LFC – liquid flow controller;  
MFC – mass flow controller;  
M – mol;  
PVD – physical vapor deposition;  
UV-VIS – ultraviolet-visible;  
NIR – near infrared ;  
XPS – X-ray photoelectron spectroscopy;  
UPS – ultraviolet photoelectron spectroscopy;  
AES – Auger electron spectroscopy;  
AFM – atomic force microscopy;  
R<sub>a</sub> – average roughness;  
R<sub>q</sub> – root mean square average roughness;  
R<sub>sk</sub> – skewness;  
SEM – scanning electron microscopy;  
EDX – energy dispersive X-ray spectroscopy;  
XRD – X-ray diffraction.

## List of Figures

<b>Figure 1-1:</b>	Schematic cross section of a FRAM unit cell [1T/1C].	1
<b>Figure 2-1:</b>	ABO <sub>3</sub> perovskite unit cell.	6
<b>Figure 2-2:</b>	Hysteresis loop and ferroelectric capacitor polarization conditions.	8
<b>Figure 2-3:</b>	Fundamentals of writing a 1T/1C cell.	10
<b>Figure 2-4:</b>	Reading a 1T/1C cell.	10
<b>Figure 2-5:</b>	Behavior of the hysteresis loop during reading a 1T/1C cell.	11
<b>Figure 2-6:</b>	Rewriting a 1T/1C cell.	12
<b>Figure 2-7:</b>	Schematic view of a NDRO FRAM structure.	13
<b>Figure 2-8:</b>	Data retention characteristics.	14
<b>Figure 2-9:</b>	Fatigue characteristics.	14
<b>Figure 2-10:</b>	Hysteresis loop.	15
<b>Figure 2-11:</b>	Crystal structure of PZT films in dependence on temperature and zirconium content x of Pb(Zr <sub>x</sub> Ti <sub>1-x</sub> )O <sub>3</sub> .	16
<b>Figure 2-12:</b>	Coupling coefficient k <sub>p</sub> and permittivity ε <sub>r</sub> values in dependence on zirconium content x of Pb(Zr <sub>x</sub> Ti <sub>1-x</sub> )O <sub>3</sub> .	17
<b>Figure 2-13:</b>	Lattice parameters of Pb(Zr <sub>1-x</sub> Ti <sub>x</sub> )O <sub>3</sub> bulk and thin films in dependence on titanium content.	18
<b>Figure 2-14:</b>	Unit cell structure of bismuth layered oxide (shown SrBi <sub>2</sub> Ta <sub>2</sub> O <sub>9</sub> ).	19
<b>Figure 3-1:</b>	TriJet™ injector.	26
<b>Figure 3-2:</b>	Photo of Tricent® reactor (AIXTRON AG).	26
<b>Figure 3-3:</b>	Block diagram of process module.	27
<b>Figure 3-4:</b>	Dual-flow showerhead.	27
<b>Figure 3-5:</b>	Molecular structure of tetraethyllead.	29
<b>Figure 3-6:</b>	Molecular structure of zirconium tetrabutoxide.	30
<b>Figure 3-7:</b>	Molecular structure of titanium isopropoxide.	31
<b>Figure 3-8:</b>	Dependencies of the vapour pressure on the ambient temperature of different precursors.	31
<b>Figure 4-1:</b>	Schematic diagram of MOCVD system.	34
<b>Figure 4-2:</b>	Typical experimental conditions and introduction sequence for PZT film deposition.	36
<b>Figure 4-3:</b>	Typical experimental conditions and introduction sequence for SBT film deposition.	38

---

<b>Figure 4-4:</b>	Schematic view of the hot wall tube reactor used for growth of the field oxide.	40
<b>Figure 4-5:</b>	Schematic view of an e-beam evaporation system.	41
<b>Figure 4-6:</b>	Used test structure of a ferroelectric capacitor.	43
<b>Figure 4-7:</b>	Geometry of an ellipsometric measurement.	44
<b>Figure 4-8:</b>	Schematic representation of the electronic levels involved in the photoemission process from a solid and the measurement of the electron energy by an analyser.	45
<b>Figure 4-9:</b>	Parallel rays reflected from points on neighbored partially reflecting planes are in phase when Bragg's law is obeyed.	47
<b>Figure 4-10:</b>	Schematic view of the used measurements system.	49
<b>Figure 4-11:</b>	Circuit for display of dielectric hysteresis (after Sawyer and Tower).	50
<b>Figure 4-12:</b>	Schematic view of the system used for the hysteresis measurements.	51
<b>Figure 4-13:</b>	Excitation signal for hysteresis measurement.	51
<b>Figure 4-14:</b>	Nomenclature used within the TF Analyzer 1000 system.	52
<b>Figure 4-15:</b>	Typical excitation signal.	53
<b>Figure 5-1:</b>	Temperature dependence of the deposition rate of the single metal-oxide films for two parameter sets of the Trijet injection system.	55
<b>Figure 5-2:</b>	Film thickness map of PZT films deposited at different pressures: a) 1.5 mbar and b) 0.5 mbar.	58
<b>Figure 5-3:</b>	Dependence of the film thickness on the position at the wafer for a PZT film grown at 550 °C and a pressure of 0.5 mbar.	59
<b>Figure 5-4:</b>	XPS spectra of a PZT thin film taken from a) the as-deposited surface and b) the surface after Ar <sup>+</sup> -ion sputtering (60 s).	60
<b>Figure 5-5:</b>	Fitted details of the XPS spectrum of a PZT thin film; a) C (1s) and b) O (1s).	62
<b>Figure 5-6:</b>	XPS spectra showing the Zr (3d) peak (a) and the Ti (2p) peaks (b). Included in (b) is a fit of the two Ti (2p) peaks.	63
<b>Figure 5-7:</b>	XPS spectra of the Pb (4f) peak of a PZT thin film; a) before and b) after sputtering. Included in the figure are also fits of these peaks.	64
<b>Figure 5-8:</b>	XPS depth profiles of a PZT film grown on Ir/TiO <sub>2</sub> /SiO <sub>2</sub> /Si substrate at 550 °C.	65
<b>Figure 5-9:</b>	SEM picture of surface of a PZT film in the case of a huge excess of lead (Pb: 73 at%).	66

---

<b>Figure 5-10:</b> XPS depth profiles of a PZT film grown on a Ir/TiO <sub>2</sub> /SiO <sub>2</sub> /Si substrate at 550 °C.	67
<b>Figure 5-11:</b> XPS spectra of a PZT thin film with a morphotropic composition.	68
<b>Figure 5-12:</b> SEM image of the substrate surface in the case of a negligible excess of lead in the film. Pb concentration is 21 at%.	69
<b>Figure 5-13:</b> Cross-sectional view of an amorphous PZT film deposited on a Ir/TiO <sub>2</sub> /SiO <sub>2</sub> /Si substrate. Pb concentration is 17 at%.	69
<b>Figure 5-14:</b> XRD patterns of PZT films deposited on Ir coated Si substrates for different concentrations of lead.	70
<b>Figure 5-15:</b> XRD patterns of PZT films with deficiency of lead before and after annealing.	72
<b>Figure 5-16:</b> XRD pattern of PZT films with a composition close to the stoichiometric before and after annealing.	73
<b>Figure 5-17:</b> AFM images (plan view) of PZT (Pb: 17 at%) thin film surfaces before (a) and after annealing at 800 °C (b).	75
<b>Figure 5-18:</b> AFM images (tilted view) of PZT (Pb: 17 at%) thin film surfaces before (a) and after annealing at 800 °C (b).	75
<b>Figure 5-19:</b> AFM images (plan view) of PZT (Pb: 21 at%) thin film surfaces before (a) and after annealing at 800 °C (b).	76
<b>Figure 5-20:</b> AFM images (tilted view) of PZT (Pb: 21 at%) thin film surfaces before (a) and after annealing at 800 °C (b).	77
<b>Figure 5-21:</b> Hysteresis loop of a capacitors with an as-deposited PZT film which exhibits an additional PbO phase.	78
<b>Figure 5-22:</b> Hysteresis loop of an as-grown PZT film showing no PbO phase.	79
<b>Figure 5-23:</b> Ferroelectric hysteresis loop (a) and I-V characteristic (b) of a PZT film on an Ir/TiO <sub>2</sub> /SiO <sub>2</sub> /Si substrate after annealing at 520°C.	80
<b>Figure 5-24:</b> Typical polarization vs. applied electric field curve of a PZT film annealed at 600 °C. The Pb content is 21 at%.	81
<b>Figure 5-25:</b> Typical polarization vs. applied electric field curve of an as-deposited PZT film with 17 at% lead.	82
<b>Figure 5-26:</b> Dielectric constant of an as-deposited lead zirconate titanate film of 21 at% lead vs. the applied electric field.	84
<b>Figure 5-27:</b> Dielectric properties of PZT (Pb: 21 at%) thin film at different annealing temperatures.	85

---

- 
- Figure 5-28:** Dielectric constant vs. electric field of lead zirconate titanate (Pb: 21 at%) capacitors measured at 100 kHz in dependence on annealing temperature. 86
- Figure 5-29:** Leakage current density vs. electric field characteristics of PZT (Pb: 21 at%) capacitors annealed at different temperatures. 86
- Figure 5-30:** Growth rate of  $\text{Bi}_2\text{O}_3$ ,  $\text{SrTa}_2\text{O}_6$ , and SBT thin films as a function of the substrate temperature at 0.35 mbar pressure:  
a) for triphenylbismuth and b) for triallylbismuth. 89
- Figure 5-31:** Growth rate of  $\text{Bi}_2\text{O}_3$ ,  $\text{SrTa}_2\text{O}_6$ , and SBT thin films as a function of the substrate temperature at 0.35 mbar pressure for tributylbismuth. 90
- Figure 5-32:** Growth rate of strontium tantalate and SBT thin films as a function of the pressure at substrate temperature of a) 450 °C and b) 550 °C. 91
- Figure 5-33:** SBT film thickness as a function of the position on the wafer. The flow rate ratio of the Sr-Ta (0.1M) precursor to tributylbismuth (0.1M) is 1:1 in a) and 1:2 in b). 92
- Figure 5-34:** SBT film thickness as a function of the position on the wafer (150 mm diameter) after optimization of the injection conditions. 93
- Figure 5-35:** Elemental composition of SBT-2 thin film (measured by XPS) as a function of  $\text{Ar}^+$  ion sputtering time. 94
- Figure 5-36:** XPS peaks of Sr 3d, Bi 4f, Ta 4f, Pt 4f, O 1s, and C 1s after different  $\text{Ar}^+$  ion sputtering times. 96
- Figure 5-37:** XRD pattern of a SBT thin film deposited at 470°C; as deposited - fluorite phase → annealed at 750°C - perovskite phase. 97
- Figure 5-38:** SEM picture of a SBT thin film grown on a Ir/TiO<sub>2</sub>/SiO<sub>2</sub> bottom electrode and annealed at 750 °C. 99
- Figure 5-39:** Typical hysteresis loop of SBT films (Bi/Ta ratio – 0.4) deposited from triallylbismuth and annealed at 750 °C temperature in air. 100
- Figure 5-40:** Hysteresis loops of SBT films deposited from tributylbismuth and annealed at different temperatures in an oxygen containing ambient. 100
- Figure 5-41:** Fatigue characteristic of a SBT film annealed at 750 °C. 101
- Figure 5-42:** Dielectric constant of SBT films annealed at 800°C versus the applied voltage, #15 – contact in the center of the chip, #20 – contact in the corner of the chip. 102
- Figure 5-43.** Leakage current density of  $\text{Sr}_{0.9}\text{Bi}_{1.2}\text{Ta}_2\text{O}_9$  thin films annealed at 750 °C. 103
-

***List of Tables***

<b>Table 2-1.</b>	Thin film properties of PZT and SBT families.	5
<b>Table 3-1.</b>	Representative volatile MOCVD precursors used in PZT thin-film deposition and their vaporization properties.	28
<b>Table 4-1.</b>	Deposition conditions of bismuth oxide and strontium tantalate oxide thin films.	34
<b>Table 4-2.</b>	Deposition conditions of SBT thin films.	37
<b>Table 4-3.</b>	Ir thin film e-beam conditions.	42

## ***Zusammenfassung***

Das Hauptziel der vorliegenden Arbeit war die Entwicklung eines Abscheideprozesses unter Einsatz von flüssigen metallorganischen Ausgangsmaterialien (liquid delivery metal organic vapor deposition LD-MOCVD) für die Herstellung von ferroelektrischen Schichten für Anwendungen in FeRAM Bauelementen und deren Charakterisierung hinsichtlich ihrer strukturellen und elektrischen Eigenschaften. Zwei unterschiedliche Materialien wurden hierbei untersucht, Blei-Zirkonat-Titanat (PZT) und Strontium-Bismut-Tantalat (SBT).

Mit Hilfe des MOCVD-Prozesses und nach anschließendem Ausheizen bei 520 °C konnten stark orientierte PZT-Schichten auf Ir/TiO<sub>2</sub>/SiO<sub>2</sub>/Si-Substraten erhalten werden. Die strukturellen und elektrischen Eigenschaften in Abhängigkeit von deren chemischer Zusammensetzung wurden systematisch untersucht.

Der Gehalt an Blei in den PZT-Schichten spielt eine herausragende Rolle für ihre ferroelektrischen Eigenschaften. Die abgeschiedenen Schichten sind amorph, wenn die Bleikonzentration geringer als 20%, der stöchiometrischen Bleikonzentration in PZT, ist. Ein anschließendes Ausheizen der Schichten mit unterstöchiometrischer Bleikonzentration führt zur Bildung einer nicht-ferroelektrischen pyrochlaren Kristallstruktur. Dabei wurden so hohe Leckströme in den ausgeheizten Schichten gefunden, dass die Hystereseschleife eine elliptische Form zeigte, die charakteristisch ist für Kondensatorstrukturen mit hohen Leckströmen.

Bei einer zu hohen Bleikonzentration treten polykristalline Schichten und die Bildung einer zweiten Phase auf. Eine Röntgen-Diffraktionsanalyse (XRD) zeigte, dass diese zweite Phase aus Bleioxid gebildet wird. Im Falle eines sehr starken Bleiüberschusses ist die Oberfläche der abgeschiedenen Schichten aufgrund von sich bildenden blättchenartigen Bleioxidkristallen sehr rau. Schichten mit solcher Oberflächenstruktur sind für eine Herstellung von Testkondensatoren ungeeignet und wurden daher nicht hinsichtlich ihrer elektrischen Eigenschaften untersucht.

Ein geringfügiger Überschuss an Blei erweist sich als erforderlich, um die gewünschte Perowskit-Struktur der abgeschiedenen PZT-Schichten zu stabilisieren. Wie oben erwähnt, führt der Überschuss von Blei zwar zur Bildung einer separaten Bleioxid-Phase in den abgeschiedenen Schichten. Jedoch zeigten Untersuchungen mittels Röntgen-Photoelektronenspektroskopie (XPS) und Rasterelektronenspektroskopie (SEM), dass die Bildung dieser Phase nur in Inseln an der Schichtoberfläche auftritt. Nach einem Ausheizen

---

bei 520°C sind die PZT-Schichten vorrangig (101)-orientiert unter vollständiger Rückbildung der zusätzlichen zweiten Phase.

Da die Flüchtigkeit von PbO bei 600°C stark ansteigt, erscheint nach Ausheizen der PZT-Schichten bei dieser Temperatur ein zusätzlicher Peak in den XRD-Spektren, der der pyrochlaren Phase zugeordnet werden kann. Die pyrochlore Phase wird im Falle eines Bleidefizits gebildet. Ein Ausheizen bei noch höherer Temperatur führt zu weiterem Rückgang der Bleikonzentration und somit zu einer Erhöhung des Anteils der pyrochlaren Phase in den Schichten. Sowohl der Überschuss als auch der Mangel an Blei in den Schichten führt zu einer Verschlechterung von deren ferroelektrischen Eigenschaften, so dass eine sorgfältige Einstellung und Kontrolle der Herstellungsparameter erforderlich ist.

Die optimierten PZT-Schichten auf Ir/TiO<sub>2</sub>/SiO<sub>2</sub>/Si-Substraten zeigen gute ferroelektrische Eigenschaften. Eine remanente Polarisierung  $P_r$  von 60  $\mu\text{C}/\text{cm}^2$  und eine Koerzitivfeldstärke  $E_c$  von 200 kV/cm wurden erhalten. Bei einer angelegten Spannung von 150 kV/cm trat hierbei nur eine geringe Leckstromdichte von  $1 \cdot 10^{-6} \text{ A}/\text{cm}^2$  auf.

Die bismuthaltige Verbindung SBT (SrBi<sub>2</sub>Ta<sub>2</sub>O<sub>9</sub>) wurde auf Iridium-beschichteten Silizium und auf (100)-Silizium bei geringen Temperaturen von 450°C durch LD-MOCVD erfolgreich abgeschieden.

Die daraus hergestellten ferroelektrischen Testkondensatoren besitzen hervorragende dielektrische, isolierende und ferroelektrische Eigenschaften.

Typische gemessene Werte von  $2P_r$  und  $E_c$  sind 7  $\mu\text{C}/\text{cm}^2$  und 100 kV/cm bei einem angelegten elektrischen Feld von 500 kV/cm. Bei dieser Feldstärke ist die Leckstromdichte geringer als  $10^{-6} \text{ A}/\text{cm}^2$ . Die Dielektrizitätszahl der SrBi<sub>2</sub>Ta<sub>2</sub>O<sub>9</sub>-Schichten ist dabei im Bereich um die 300. Nach  $10^9$  Umschaltzyklen der Polarisierung ergibt sich eine Verschlechterung der remanenten Polarisierung von nur 4% infolge Ermüdung.

Die SBT-Schichten auf Ir-beschichteten Substraten zeigen eine zufällige Orientierung ihrer polykristallinen Körner im gesamten Bereich der chemischen Zusammensetzung. Die SBT-Schichten, die mittels konventioneller MOCVD auf (100)-Silizium abgeschieden wurden, zeigen keine ferroelektrischen Eigenschaften, wahrscheinlich als eine Folge von extrinsischem Stress und extrem kleiner Korngrößen.

Geringe Abscheidetemperaturen, gute strukturelle, isolierende und ferroelektrische Eigenschaften der SBT-Schichten sind viel versprechende Ergebnisse im Hinblick auf eine künftige Integration von ferroelektrischen SBT-Kondensatoren in höchstintegrierten nicht-flüchtigen Speicherzellenstrukturen.

## Chapter 1 Introduction

### 1.1 Purpose of Research

The current research is an effort to tackle and to solve the problems which can be related to the fabrication of a ferroelectric capacitor for use in high density ferroelectric random access memory (FRAM) cells. In a high density memory structure, the ferroelectric capacitor is fabricated on the top of a plug, which in turn is connected to the drain of the transistor, as shown in figure 1-1. Such a configuration would result in the requirement for (a) processing of ferroelectric material and (b) in the choice of bottom and top electrode materials.

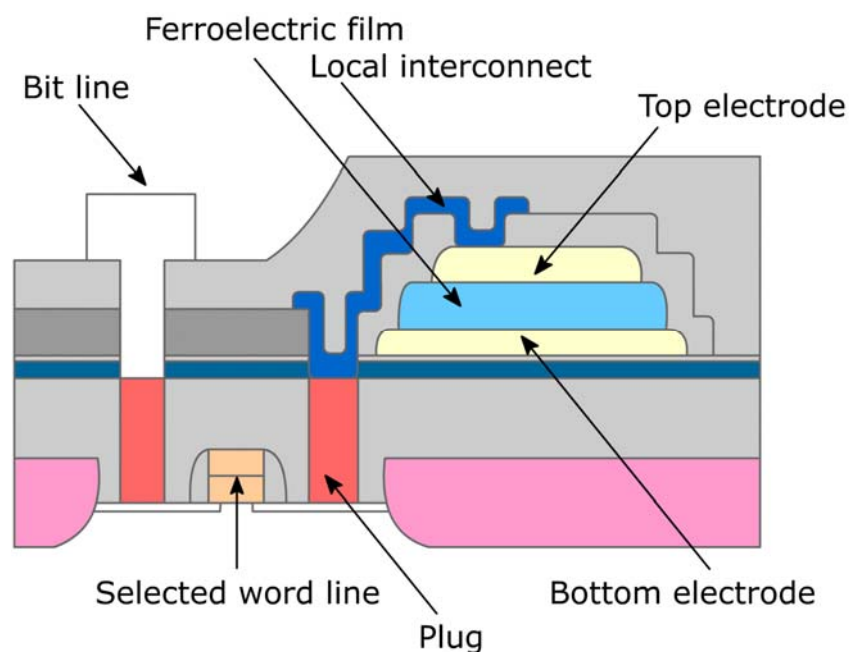


**Figure 1-1:** Schematic cross section of a FRAM unit cell [1transistor/1capacitor].

### 1.2 Requirements for the Processing of Ferroelectric Material

- 1) In a high-density memory configuration, transistor is fabricated prior to the fabrication of the capacitor. In order to preserve the integrity of the transistor, the processing temperature of the ferroelectric capacitor should be as low as possible.
- 2) Even at low processing temperatures, a ferroelectric capacitor should exhibit well defined ferroelectric properties.
- 3) The ferroelectric capacitor should possess high remanent polarization so that the memory stored in these capacitors could be read in an unambiguous manner.
- 4) Coercive field required to switch the memory from one state to the other state should be as low as possible.

- 5) The ferroelectric capacitor should possess reproducible properties.
- 6) The ferroelectric capacitor should possess minimal fatigue while maintaining low leakage current density.

### ***1.3 Choice of Bottom Electrodes***

Suitable bottom electrodes should be chosen that would enable the integration of the capacitor on the top of the poly-silicon plug. Bottom electrode structures have to fulfill the most stringent requirements in order to maintain a conductive path between a transistor and a capacitor and preserve the integrity of the devices during the fabrication of the memory structures. The electrode structures which enable the integration of the capacitor on top of the transistor should satisfy the following conditions:

- 1) Should be resistant to the formation of an insulating oxide and remain electrically conductive after fabrication of the dielectric.
- 2) Should act as a barrier to oxygen diffusion.
- 3) Should act as a barrier to silicon diffusion.
- 4) Should not interact with the dielectric or with the plug material (silicon), or the interaction should be limited and the product of the interaction should be electrically conductive.
- 5) Should act as a diffusion barrier to the elements in the ferroelectric materials.
- 6) Should maintain interface smoothness during the fabrication process.
- 7) Should maintain low leakage currents through the capacitor.
- 8) Should prevent the fatigue of the ferroelectric capacitor.
- 9) Should promote the crystallization of the ferroelectric material.

### ***1.4 Objectives of Research***

The objectives of this research are outlined as follows:

- 1) Developing a low temperature deposition process of ferroelectric thin films based on the understanding of the transformation kinetics.
- 2) Characterization of structural and electrical properties of the as-deposited and annealed layers.
- 3) Investigation of the effect of compositional ratio on the structural and electrical properties of ferroelectric thin films.
- 4) Demonstration of the compatibility of ferroelectric films to existing barrier layers.

---

## **Chapter 2 Fundamentals**

### **2.1 Ferroelectric Memories**

In the present time fourteen generally different kinds of digital memories are used for storage of information in computers and other devices. These memories range from slow, inexpensive tapes or discs used for archival storage to fast but expensive static random access memories (SRAMs) and dynamic random access memories (DRAMs). All kinds of memories can be divided into the general categories of volatile memory, which loses stored data without an external power source, and non-volatile memory, which stores recorded data even after the external power source has been switched off. For example, magnetic disks are non-volatile. However, magnetic disks are large and mechanically fragile, consume a lot of power and have the disadvantage of slow access speeds during writing and reading data. In case of a DRAM, the data is stored in the form of charge in a linear capacitor. In order to safely maintain the stored data, it is necessary to supply a constant voltage to the capacitors, which are recharged hundreds times per second by a refresh circuitry. If the power is interrupted, a DRAM loses all data stored in it; this means a DRAM is volatile. In contrast, data in ferroelectric capacitors are stored as remanent polarization states of the ferroelectric material itself. A ferroelectric capacitor has a nonlinear dielectric property with permanent charge retention capabilities after the voltage application. The stored data do not disappear, even though the power is turned off, that is, a FRAM is nonvolatile.

To account for power turned off or outages, some of the more expensive memories use internal electrical erasable programmable read only memories (EEPROMs), that store data as electrical charges in floating-gate electrodes, back up in SRAMs or use a battery to create a non-volatile RAM for data backup. However, EEPROMs take long time to write data, and have limits on the number of times that data can be rewritten. These drawbacks can be completely eliminated if SRAMs, EEPROMs and flash memories can be replaced by ferroelectric random access memories (FRAMs) which can be tailored to possess longer lifetimes and higher speeds.

In the current time, non-volatile memories, as flash memories and EEPROMs, are widely used. These non-volatile memories have an inherent limitation, their relatively low lifetime. For example, the number of times a memory bit could be written into a flash memory is limited to a maximum of only  $10^5$ . In terms of lifetime, FRAMs have been shown to be potential candidates for non-volatile random access memories, where the lifetime could be extended to a value of at least  $10^8$  cycles [1].

When one considers all the selection requirements for a nonvolatile memory, namely fast read/write, radiation hardness, cost effectiveness and compatibility with currently used integrated circuit (IC) processing technology, high endurance and retention, and nondestructive readout capability, the ferroelectric memory stands out as the logical choice.

In the current commercial world, the use of FRAMs is limited to applications which include low density memories in video game devices, TV sets, FAX machines, printers, mobile phones and fully embedded ferroelectric memories in silicon microprocessors and microcontrollers. Some of the state-of-art FRAMs, available commercially, are 4 Mbit RAMs from Samsung [2], 1Mbit RAMs from NEC and 256 kbit RAMs from Matsushita [3]. However, currently available commercial FRAMs are limited to low density structures, in which one transistor/one capacitor structures (1T/1C) are used with the capacitor being located adjacent to the transistor [4]. FRAMs could possess an appreciable market in the field of non-volatile memories, provided high density FRAMs are commercialized. In order to realize high density FRAM structures (in the Gigabit range), a FRAM cell is required in which the capacitor is on top of the transistor. Current research focuses on the fabrication of ferroelectric capacitors which could be integrated directly on top of the transistor. While the transistor in the 1T/1C memory structure acts as an access switch to the capacitor, the data bit is stored in the ferroelectric capacitor.

In principle, FRAMs could replace EPROMs (erasable programmable read only memory), EEPROMs (electronically erasable programmable ROM), SRAMs (static RAM), and DRAMs. Furthermore, if high density FRAMs could be developed and the production cost could be reduced down to the level of magnetic cores, then FRAMs could also replace the hard disk as the mass storage device, due to their faster access speed and the absence of mechanical wear problems [5].

## ***2.2 About Ferroelectric Materials***

Two families of materials, lead zirconate titanate (PZT) and strontium bismuth tantalate (SBT), have been widely investigated for memory applications. Their electrical characteristics can be modified by dopant addition (PLZT, PNZT: La or Nb doped PZT, SBTN: Nb doped SBT); advantages and disadvantages of both materials are listed up in table 2-1. PZT films grown on Pt electrodes show fatigue problems, that is, the remanent polarization value decreases with read/write repeating cycles [6]. This problem can be over come by replacing the metallic Pt electrode with a metal oxide electrode such as  $\text{RuO}_2$ ,  $\text{IrO}_2$  and  $\text{La}_{0.5}\text{Sr}_{0.5}\text{CoO}_9$  or with a multi-electrode like  $\text{RuO}_2/\text{Pt}$ . Practically,  $\text{IrO}_2/\text{Pt}$  and  $\text{IrO}_2/\text{Ir}$  multi-electrode systems are being used in FRAM industries [2].

The bismuth layered structure SBT films are attractive because of their good fatigue properties. Therefore, the use of SBT films instead of PZT films can simplify the integration process. However the process temperatures are high in relation to the standard silicon process and, therefore, SBT films are not applicable to high density FRAM fabrication at present. Many efforts have been directed to reduce the formation temperature in terms of process optimization, precursor system, and solid-solution method [7].

In this thesis, PZT and SBT thin films have been selected as ferroelectric materials for FRAM capacitors. The three arguments for PZT are the following:

- Remanent polarization ( $P_r$ ) values in PZT capacitors are larger than in SBT capacitors.
- The formation temperature of a PZT film is considerably lower than that of an SBT film.
- PZT films show relatively stronger endurance against hydrogen-induced damage compared with SBT films [8, 9].

SBT thin film structures have also been investigated since SBT is a further promising material for FRAM memory applications because of its low leakage current, good fatigue and retention characteristics. Furthermore:

- SBT based capacitors do not require the use of sophisticated metal oxide or hybrid-metal oxide-metal electrodes and exhibit negligible fatigue and imprint even when the simpler Pt electrode technology is used.
- SBT based capacitors do not involve chemicals, which may be related to contamination and hazardous problems during fabrication.
- SBT layers maintain good electrical properties even when they are very thin (<100 nm).

**Table 2-1.** Thin film properties of PZT and SBT families.

	PZT families	SBT families
Crystal Structure	ABO <sub>3</sub> type perovskite	Bi layered structure
Formation temperature (°C)	600 – 700	750 – 850
Switching polarization( $\mu\text{C}/\text{cm}^2$ )	30 – 60	5 – 10
Coercive field (kV/cm)	50 – 70	30 – 50
Dopants	Nb, La	Nb
Dielectric constants	400 – 1500	200 – 300
Fatigue (Pt electrode)	Poor (oxide needed)	Good
Curie temperature (°C)	400 – 500	~ 310

Ferroelectric materials are characterized by a reversible spontaneous polarization in the absence of an electric field. Spontaneous polarization in a ferroelectric arises from a non-centrosymmetric arrangement of ions in its unit cell that produces an electric dipole moment. Adjacent unit cells tend to polarize in the same direction and form a region called a ferroelectric domain. The most common ferroelectrics have the  $ABO_3$  perovskite structure shown in figure 2-1. The perovskite structure belongs to the tetragonal crystal system with a preferred axis, the (001) orientation in figure 2-1.

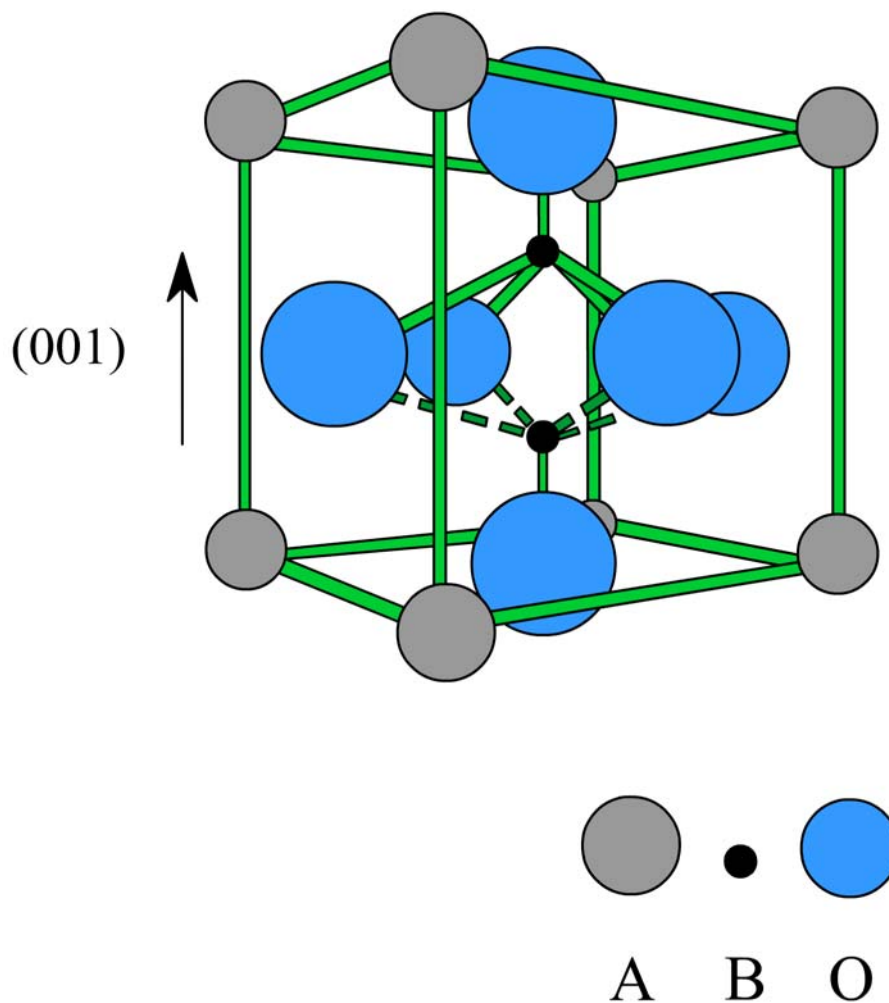


**Figure 2-1:**  $ABO_3$  perovskite unit cell.

In this extended (001) orientation, the displacement of positive ions (A and B), negative ions and their valence electrons separates the center of gravity of the positive and negative electric charges, which allows an electrical polarization moment to occur. The charge amount of the electrical polarization moment per unit area is the electrical polarization ( $\mu\text{C}/\text{cm}^2$ ).

The extended (001) orientation is called the c axis, while the a axis has (100) and the b axis has (010) orientations. Electrical polarization only occurs along the c axis orientation.

Above the Curie temperature, these materials have a centrosymmetric structure and, therefore, lose all spontaneous polarization. In this state, the material is termed paraelectric. When the temperature decreases below the Curie point, a phase transformation takes place from the paraelectric state to the ferroelectric state. The center ion is displaced from its body-centered position and the cubic unit cell deforms to assume one of the non-centrosymmetric structures such as tetragonal, rhombohedral or monoclinic.

When an alternating electric field is applied to the ferroelectric material, the polarization shows a hysteresis behavior in dependence on the applied field (figure 2-2). The B atom, which has two thermodynamically stable positions inside the oxygen octahedra, is displaced relative to the oxygen atoms upward or downward, depending on the polarity of the electric field. This displacement generates a dipole moment inside the oxygen octahedra, which is called the saturated polarization  $P_{\text{sat}}$ . In this state, the ferroelectric domains which are oriented favorably with respect to the applied field direction grow at the expense of other domains. This continues until total domain growth and reorientation have occurred.

If the applied electric field is then removed, the B atom remains in the displaced position (some of the domains do not return to random configurations and orientations) and generates a residual polarization in the absence of an applied electric field. The polarization in this case is called the remanent polarization,  $\pm P_r$ .

The strength of the electric field required to return the polarization to zero is the coercive field,  $E_c$ . The basic characteristics of a ferroelectric material are its ability to retain two stable remanent polarization values at zero field, thus providing non-volatility. The state of polarization can be controlled and sensed by reversing the polarization from up (1) to down (0) or vice versa as a function of the applied voltage.

Although these features of a ferroelectric material could be used in a wide range of applications the primary focus of the recent research is directed towards the development of non-volatile random access memories.

The FRAM is a memory which uses the advantage of the polarization phenomenon of ferroelectrics. To understand the principles of a FRAM cell operation, at first the characteristics of ferroelectrics or the hysteresis characteristics which exhibit a voltage dependency of a polarized electric charge  $Q$ , and, secondly, the correspondence of these characteristics with the polarization conditions of a ferroelectric capacitor have to be taken into consideration.

If the voltage applied to the ferroelectric capacitor is  $V_f$ , and the voltage level of the bottom electrode is plus (+) with respect to the top electrode, the charge accumulates in the ferroelectric capacitor. Figure 2-2 depicts the relationship between the hysteresis loop and the charge that accumulates in the capacitor.

In this figure, six points are marked on the hysteresis loop, indicating the condition of a ferroelectric capacitor. At  $V_f = 0V$ , points A and D describe different polarization conditions with a remanent polarization of  $\pm P_r$ . At  $V_f = \pm V_c$ , points B and E indicate a polarization of 0, and the points C and F describe the conditions of  $V_f = \pm V_{cc}$ .

When the applied voltages vary from  $0V$  to  $+V_{cc}$ , and from  $0V$  to  $-V_{cc}$ , the polarization changes around the loop from point A  $\rightarrow$  point B  $\rightarrow$  point C, and from point D  $\rightarrow$  point E  $\rightarrow$  point F, respectively. At points C and F, the polarization charges are  $Q_s$  and  $-Q_s$ , respectively. This is known as the saturated polarization charge. Points C and F correspond to the material state, when all domains are reoriented favorably with respect to the applied field direction.

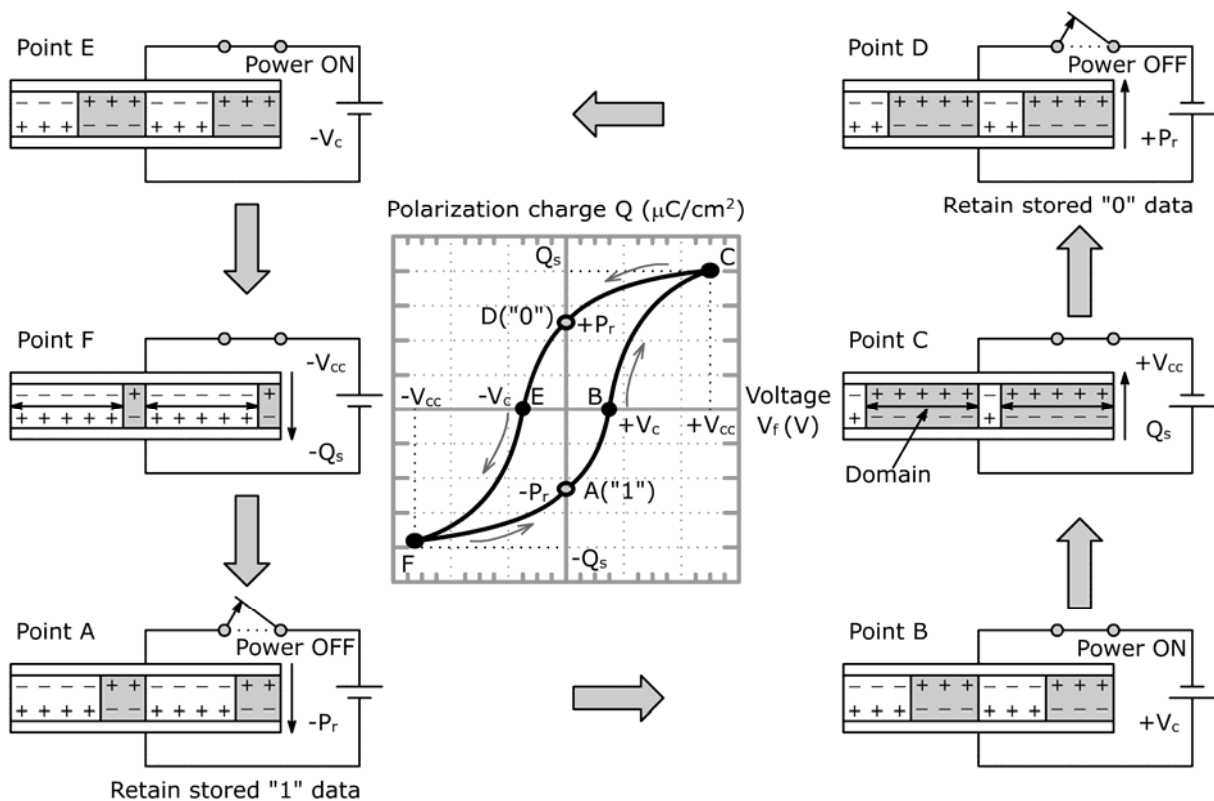


**Figure 2-2:** Hysteresis loop and ferroelectric capacitor polarization conditions.

If the applied voltages are then changed, from  $+V_{cc}$  to  $0V$  and from  $-V_{cc}$  to  $0V$ , the polarization value also changes, moving from point C to point D, and from point F to point A, respectively in the hysteresis loop of figure 2-2. In this situation, the polarization charge decreases slightly, without reversing the direction of the polarity. Thus, applying a voltage of  $0V$  (power off) to the ferroelectric capacitor results a remanent polarization charge  $\pm P_r$  in figure 2-2 either in point D or in point A of the hysteresis loop depending on the starting position. Furthermore, these two states of polarization are both stable. Either of these two states could be encoded as a "1" or a "0" and since no external field is required to maintain these states, the memory device is nonvolatile. Obviously to switch the state of the device a threshold electric field higher than the coercive field is required. Since ferroelectric materials have very high coercive fields (in the order of  $kV/cm$ ), it is necessary to fabricate these materials in the form of thin films in order to be able to switch the domains from one orientation to the other.

If a voltage is applied to a ferroelectric capacitor in a direction opposite to that of previous voltage the remanent domains will switch, requiring a compensating charge to flow to the capacitor plates. If the field is applied in the direction of the previously applied field, no switching takes place, no change occurs in the compensating charge and hence a much reduced amount of charge flow to the capacitor takes place. This phenomenon can be used to read the state or write a desired state into a ferroelectric storage device.

### **2.3 Writing and Reading Cell Data**

Writing "1" or "0" data to a cell requires the application of the voltage  $+V_{cc}$  or  $-V_{cc}$  to the ferroelectric capacitor.

Figure 2-3 helps to explain the writing of the 1T/1C cell (comprising one transistor and one ferroelectric capacitor). The word line (WL) is selected (meaning that the transistor is "on") and a voltage ( $V_{cc}$ ) is applied between the bit line (BL) and the plate line (PL). Applying of this voltage to the ferroelectric capacitor causes writing of data. Writing "0" data is accomplished by making  $BL = 0V$  and  $PL = V_{cc}$ , whereas "1" data is written by making  $BL = V_{cc}$  and  $PL = 0V$ .

After writing, data is retained even if the selected word line becomes unselected (meaning that the transistor is "off"). In other words, the data is non-volatile. As described above, the polarity remains as remanent polarization ( $+P_r$ ,  $-P_r$ ) even if the applied voltage is removed.

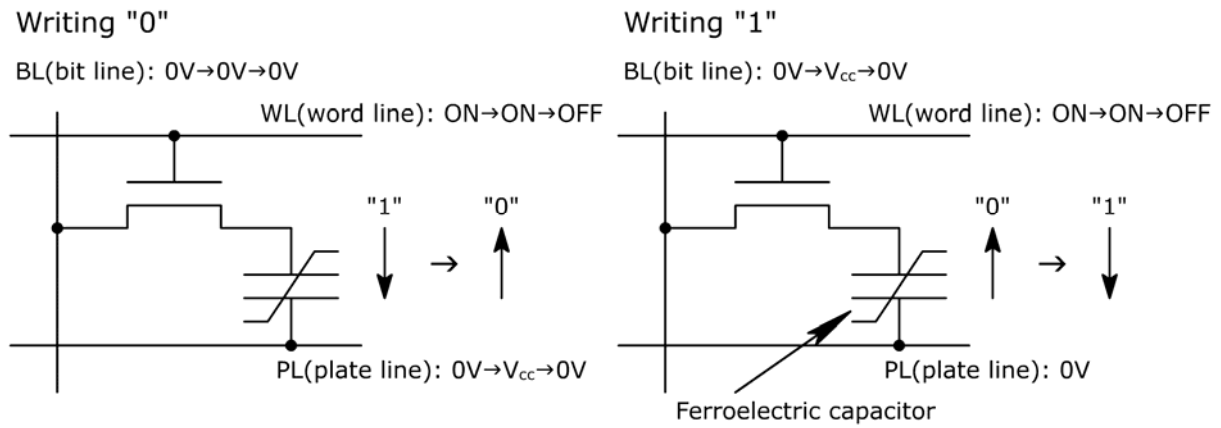


**Figure 2-3:** Fundamentals of writing a 1T/1C cell.

The FRAM devices are divided into two categories, based on the readout technique: destructive read-out (DRO) FRAM and non-destructive read-out (NDRO) FRAM. In a DRO FRAM device, the ferroelectric thin film is used as a capacitor dielectric. This capacitor is connected to the drain of a complementary metal-oxide-semiconductor (CMOS) transistor. The basic unit of DRO FRAM devices is, therefore, 1 transistor and 1 capacitor (1T/1C). The stored information is read by sensing the electrical charge created by switching the polarization of ferroelectric materials in the capacitor. After the reading operation, the polarization state is changed from  $+P_r$  to  $-P_r$  or vice versa. Thus, the information must be rewritten for restoring the polarization state after every read operation.

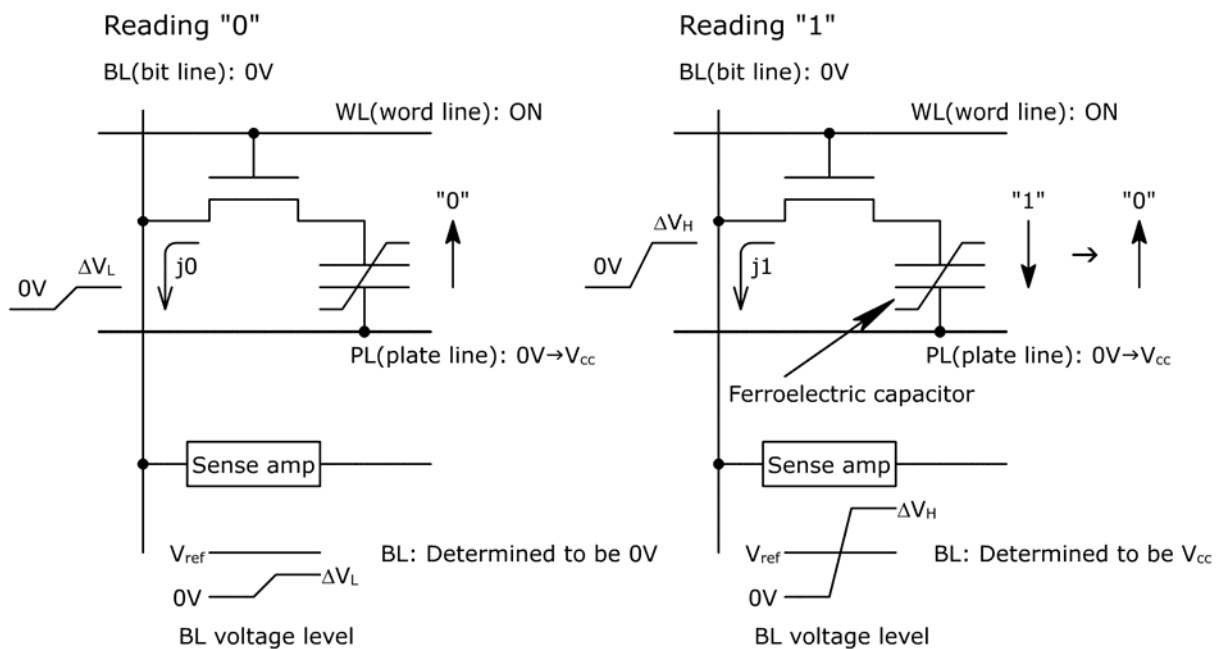


**Figure 2-4:** Reading a 1T/1C cell.

During reading “1” or “0” data from a cell, prior to selecting the word line, the bit line must be switched to 0V to retain the high-impedance condition. Next, the word line is selected and  $V_{cc}$  is applied to the plate line. By applying a voltage to the ferroelectric capacitor, the data can be read out (see figure 2-4).

As figure 2-5 indicates, if the cell holds “0” data, the polarization is not reversed but the relatively slight movement of the electric charge ( $j_0$ ) causes the bit line to charge up to a certain value. Since the value of voltage induced by charging of the bit line is relatively low, the value of the bit line is marked with  $V_L$ .

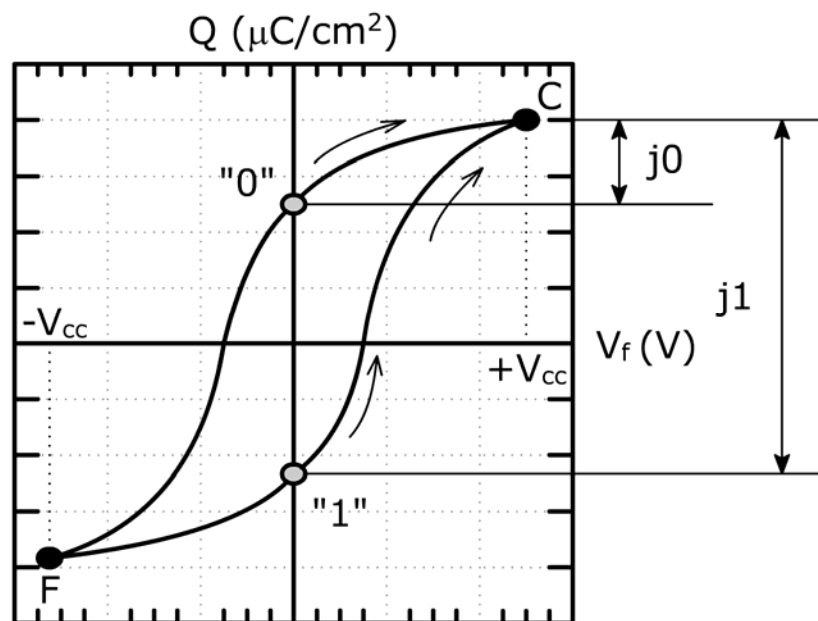


**Figure 2-5:** Behavior of the hysteresis loop during reading a 1T/1C cell.

If the cell holds “1” data, polarization is reversed, causing a major movement of the electric charge ( $j_1$ ).

The flow of the high charge current  $j_1$  corresponds to a high value  $V_H$  of the bit line. The sense amp, which holds the reference voltage ( $V_{ref}$ ) adjusted to a value between  $V_L$  and  $V_H$ , is connected to the bit line. In this manner,  $V_L$  – which has a lower voltage level than  $V_{ref}$  – can be further reduced to 0V, and  $V_H$  – which has a higher voltage level than  $V_{ref}$  – can be raised further to  $V_{cc}$ .

The post amplification bias states of the ferroelectric capacitor are: when reading “0”,  $V_f = +V_{cc}$  (the same state as for writing “0”) with  $V_{BL} = 0V$  and  $V_{PL} = V_{cc}$ . When reading “1”,  $V_f = 0V$ , meaning that the cell has a 0 (zero) bias, with  $V_{BL} = V_{cc}$ .

Since no reversal of polarity occurs, during reading of “0” data, the data is not destroyed and a value of “0” is retained.

During reading “1” data, the reversal of polarity causes destroying of the data and a “0” data state is created. The “1” data needs to be written again to restore the data to its correct value before the next reading.

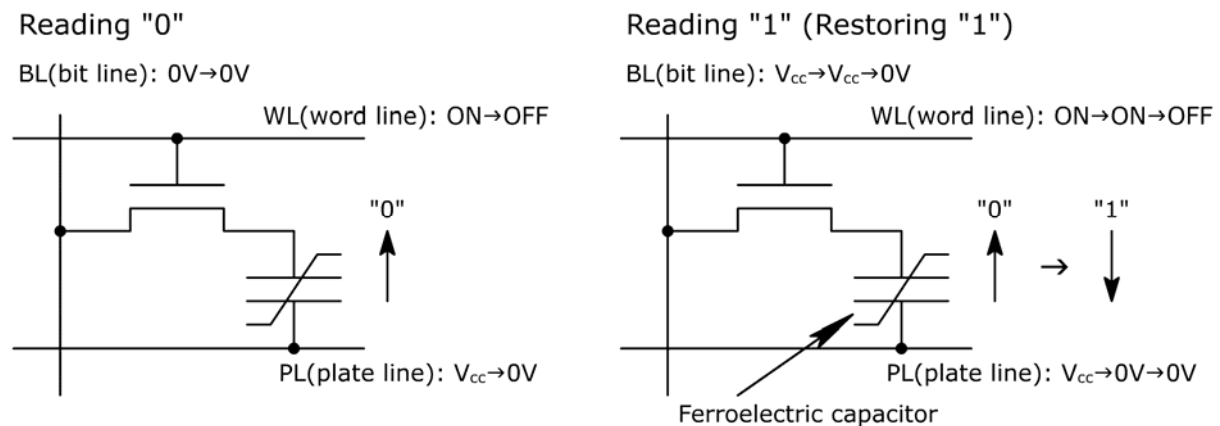


**Figure 2-6:** Rewriting a 1T/1C cell.

After reading of “1” data, the bit line voltage level is  $V_{cc}$  (see figure 2-6). At this time, the plate line voltage level becomes 0V, causing rewriting of “1” data. When the word line is turned off, the bias of the ferroelectric capacitor becomes “0”, and the “1” data is stored. In this way, the stored data returns to the original “1” data. Thus, a reset procedure is required to restore the switched polarization state to the original position and secure the stored information. Even though this DRO FRAM needs a reset pulse, it has the advantage of a very fast access speed in comparison to the NDRO FRAM.

On the other hand in the NDRO FRAM the ferroelectric thin film is used as the gate material in the transistor, and thus, no additional capacitor is needed. The basic unit of a NDRO FRAM device is one transistor. Figure 2-7 shows how a NDRO device stores and reads information.

Since the surface conductivity of the silicon depends on the direction of the remanent polarization, an “on” or “off” channel region is generated at the surface of the silicon. If the ferroelectric film is prepared on p-type Si, and a positive voltage is applied to the films, the direction of the polarization is directed downwards (see figure 2-7) and induces negative charges at the surface of the silicon (inversion layer of electrons) giving rise to a conductive channel (“on”). Even though the applied voltage is removed, the “on” channel is maintained due to the remanent polarization of the ferroelectric film. In case of applying a negative voltage positive charges (accumulation state) are induced at the surface of the silicon,

generating a non-conductive (“off”) channel. These “on” and “off” channels work as binary “0” and “1” in the memory logic.

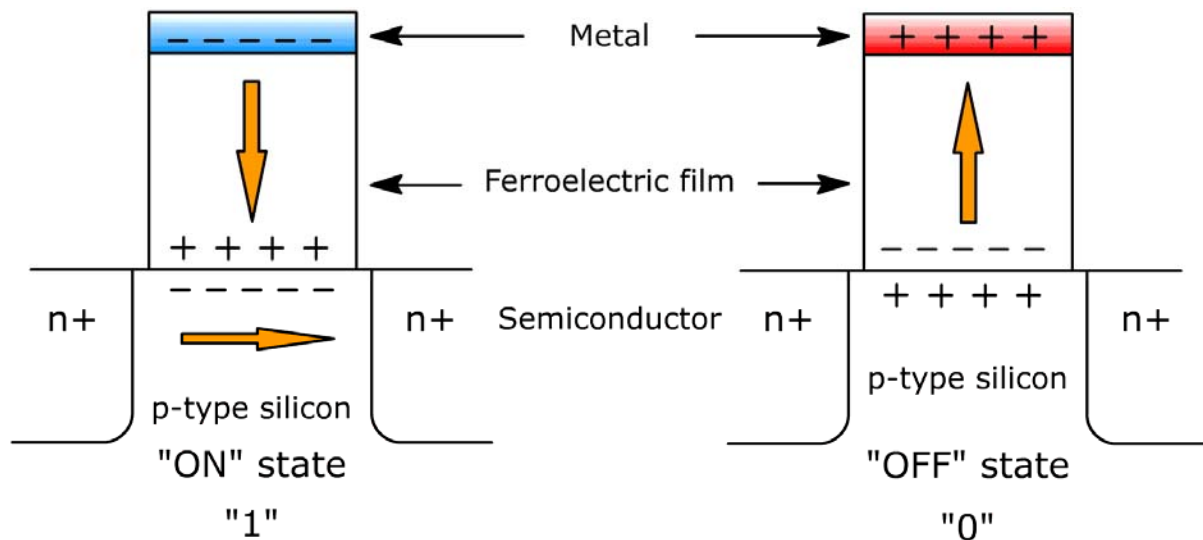


**Figure 2-7:** Schematic view of a NDRO FRAM structure.

The reading operation is thus carried out by identifying whether the current flows from source to drain or not. This reading method provides a privilege of non-destructive readout and eliminates the reset procedure. Therefore, the information can be read over and over again until the next write operation.

## 2.4 Reliability of Ferroelectrics

The ferroelectric materials used for FRAM cells have three main characteristics which affect the reliability of data retention.

### 2.4.1 Data Retention Characteristics

Figure 2-8 depicts the data retention characteristics. As time  $t$  elapses, the polarization charge  $Q$  decreases. This characteristic determines the data retention capability of a non-volatile memory. It can be acceleration tested by increasing the temperature of operation and is predominantly affected by material properties. From the view of circuit design, this characteristic can be improved by optimizing the write voltage value of the ferroelectric capacitor.

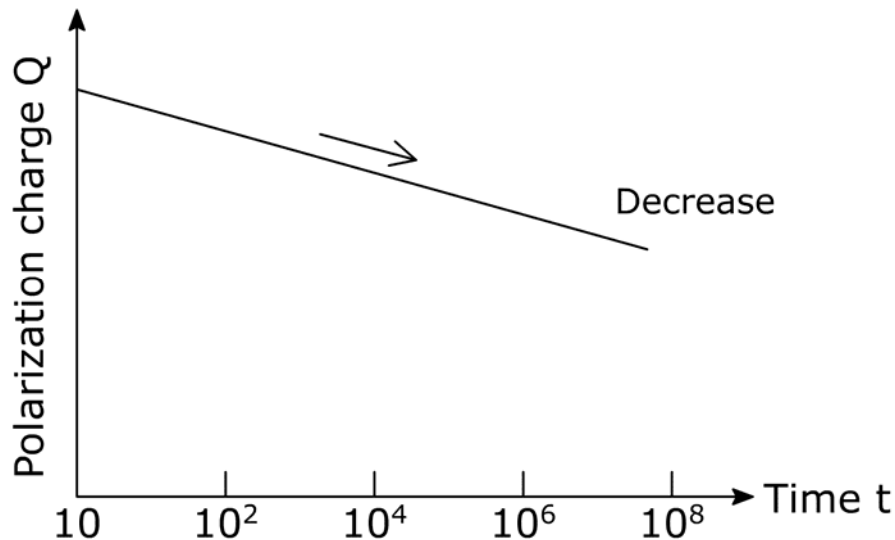


**Figure 2-8:** Data retention characteristics.

### 2.4.2 Fatigue Characteristics

The fatigue characteristics refer to the tendency of the polarization charge  $Q$  to decrease as a result of repeated polarization reversals, as can be seen in figure 2-9. The horizontal axis of this graph indicates the number of times the polarization is reversed, while the ordinate shows the polarization charge. Fatigue characteristics are reported to be highly dependent on the operating voltage value, with deterioration occurring faster at higher operating voltages [10]. For a FRAM a data rewriting is necessary not only when writing but also when reading; this results in an increase in the number of polarization switching cycles. Considering the retention described above as a FRAM operating mode, ideally write/read should be operated with a voltage as low as possible.

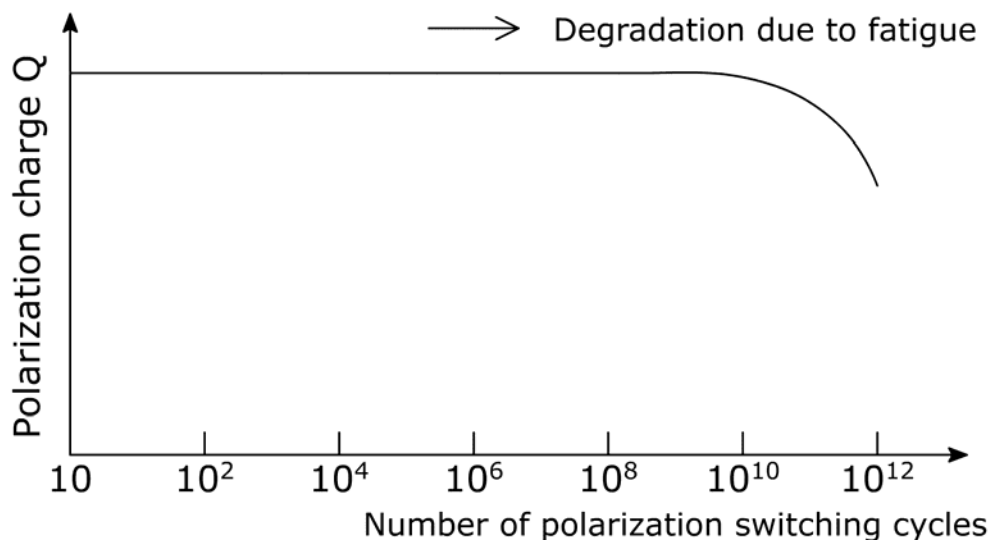


**Figure 2-9:** Fatigue characteristics.

### 2.4.3 Relaxation Characteristics

Up to now, a hysteresis characteristic of a ferroelectric capacitor has been considered to be ideal and its time dependency has been neglected. A real hysteresis characteristic follows the curve depicted in figure 2-10 [10]. At  $V_f = 0V$ , the point of remanent polarization, the polarization charge decreases a little bit in dependence of time, this means,  $P_r$  decreases from “F” to “A” and from “C” to “D” in figure 2-10, respectively. This is a short term decrease in  $Q$  while the retention characteristics describe the loss of  $Q$  over a long period of time.

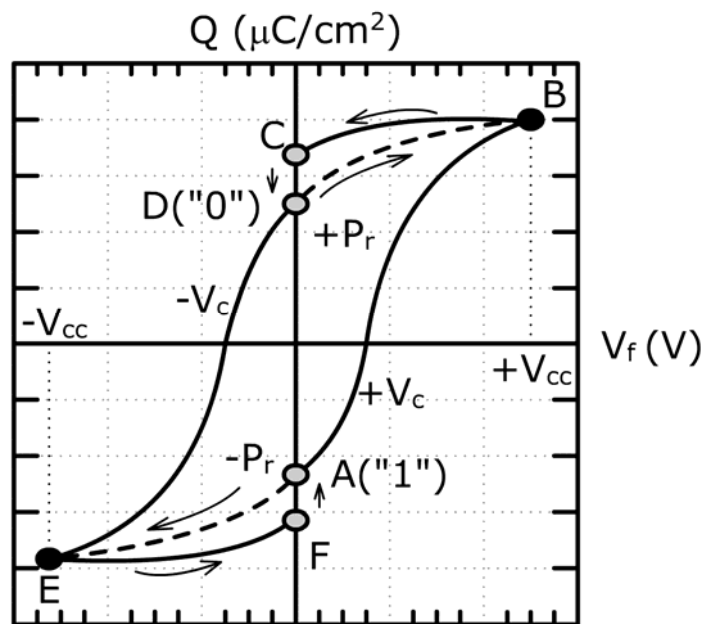


**Figure 2-10:** Hysteresis loop.

### 2.5 Crystal Structure of $Pb(Zr,Ti)O_3$ (PZT) Films

In the 1950s the solid solution system lead zirconate titanate  $Pb(Zr,Ti)O_3$  (PZT), which has a perovskite crystal structure, was found to be ferroelectric. Lead zirconate titanate of various compositions are now the most widely investigated of all piezoelectric ceramics [11].

The solid-solution PZT has a wide range of ferroelectric phase transition temperatures (Curie-temperatures) and two different ferroelectric structures, depending on the Zr/Ti composition ratio [12]. Figure 2-11 shows the triangulation lead zirconate – lead titanate of the ternary system PZT. If the Ti content is higher than 0.47 and the Zr content lower than 0.53, PZT transforms from the cubic structure to the tetragonal structure at temperatures ranging from 370 to 490 °C. If the Ti content is lower than 0.47, there is a cubic to rhombohedral transition with Curie-temperatures ranging from 230 to 370 °C.

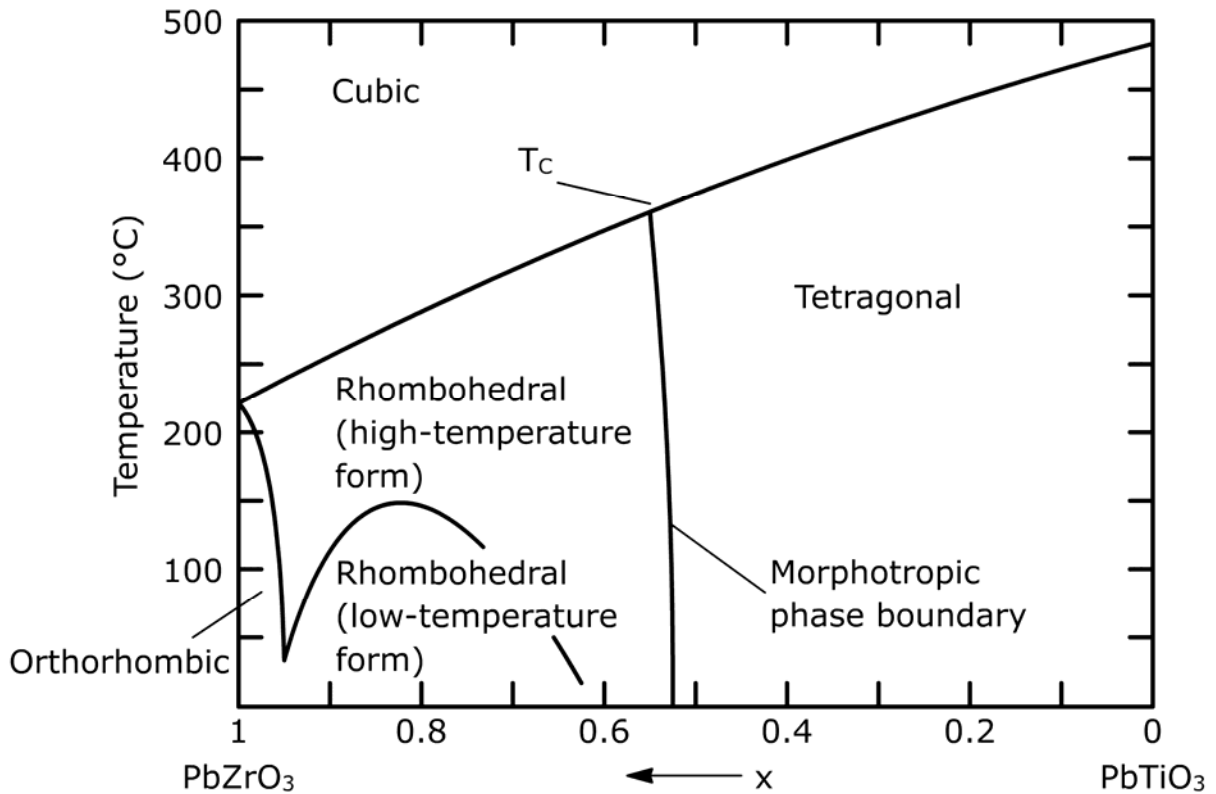


**Figure 2-11:** Crystal structure of PZT films in dependence on temperature and zirconium content  $x$  of  $\text{Pb}(\text{Zr}_x\text{Ti}_{1-x})\text{O}_3$ .

The crystal phase diagram clearly shows that the Curie-temperatures of PZT increase with an increase of the Ti content. A ferroelectric memory needs to have a wide range of operating temperatures within which the electrical properties are maintained constant.

A significant feature of the phase diagram of figure 2-11 is the presence of the morphotropic phase boundary (MPB). The MPB denotes an abrupt structural change with composition at constant temperature in the solid solution range. The MBP composition range has been believed to be quite narrow, but in practice the MPB has a wide range of compositions over which the tetragonal and rhombohedral phases coexist in ceramics [13-16]. Both the dielectric constant and the piezoelectric coefficients near the MPB are enhanced due to the metastable coexistence of tetragonal and rhombohedral phases resulting in a maximum poling efficiency and electromechanical activity. Also, the mixture of the tetragonal and rhombohedral structures in MPB region gives good ferroelectric properties to the PZT films at  $\text{Ti} = 0.47$ .

Since all properties take extreme values near MPB (see figure 2-12), the width of the MPB has been investigated by many authors and found to be related to the heterogeneous distribution of  $\text{Zr}^{4+}$  and  $\text{Ti}^{4+}$  cations on the B-site of the perovskite lattice ( $\text{ABO}_3$ ) [13].

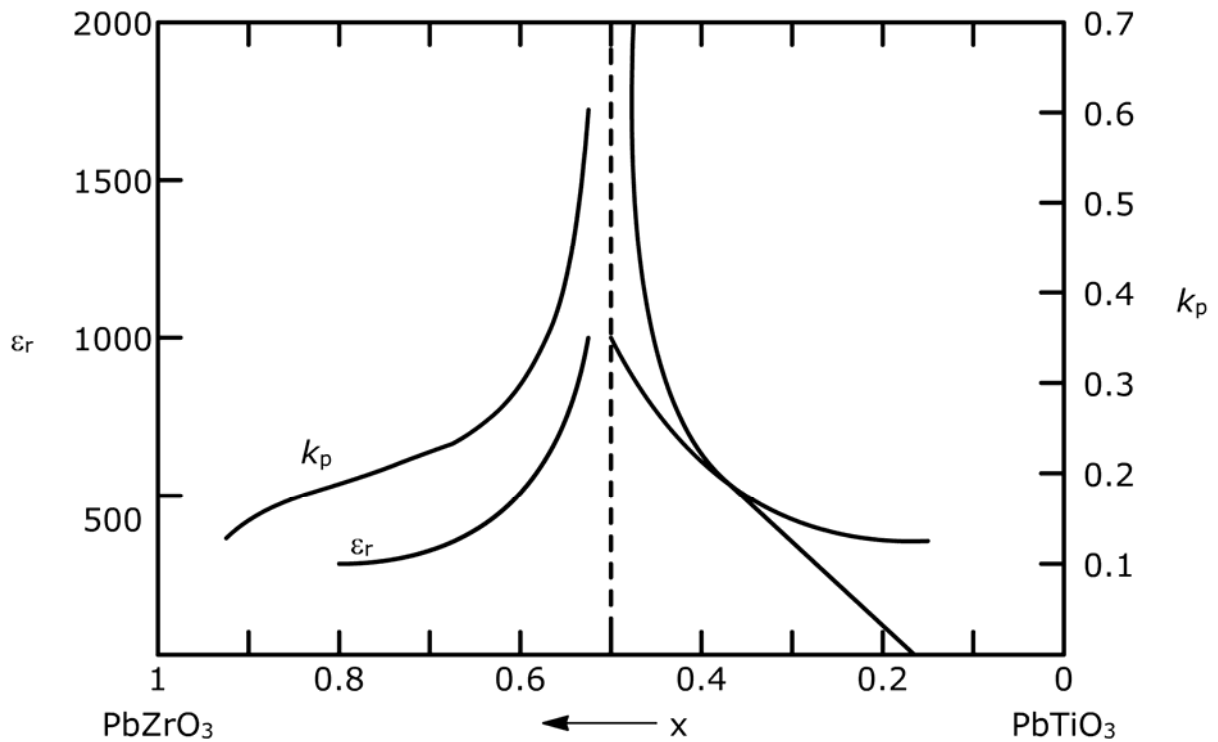


**Figure 2-12:** Coupling coefficient  $k_p$  and permittivity  $\epsilon_r$  values in dependence on zirconium content  $x$  of  $\text{Pb}(\text{Zr}_x\text{Ti}_{1-x})\text{O}_3$ .

The coexistence of two phases over a range of compositions close to the MPB was demonstrated by S. Zhao *et al.* [14].

The lattice parameters of the tetragonal structure of  $\text{Pb}(\text{Zr}_{1-x}\text{Ti}_x)\text{O}_3$  films are changed as a function of the titanium content  $x$  too. It was observed that the  $c/a$  lattice ratio decreased as the Ti content  $x$  increased [15].

Figure 2-13 shows the dependence of the lattice parameters on the titanium content  $x$  in  $\text{Pb}(\text{Zr}_{1-x}\text{Ti}_x)\text{O}_3$  films. The corresponding thin films and bulk data are given for comparison. The  $a$ -axis and  $b$ -axis lattice parameters of lead zirconate titanate thin films almost correspond to those of the bulk ceramics, whereas the lattice constants of the  $c$ -axis are slightly smaller than those of the bulk. This difference might be attributed to the orientation of the PZT thin films and/or to the stress caused by the difference in thermal expansion coefficients between the films and Pt substrate rather than to the deviation of composition [15]. The Ti-rich PZT films show a tetragonal structure whose unit cell distortion, i.e. the  $c/a$  ratio, increases as the Ti content increases. A transition from the tetragonal to the rhombohedral phase has been observed as the Zr/Ti ratio increases [14,16]. Moreover, the polar axis changes from the [001] to the [111] direction if the crystal structure changes from tetragonal to rhombohedral.

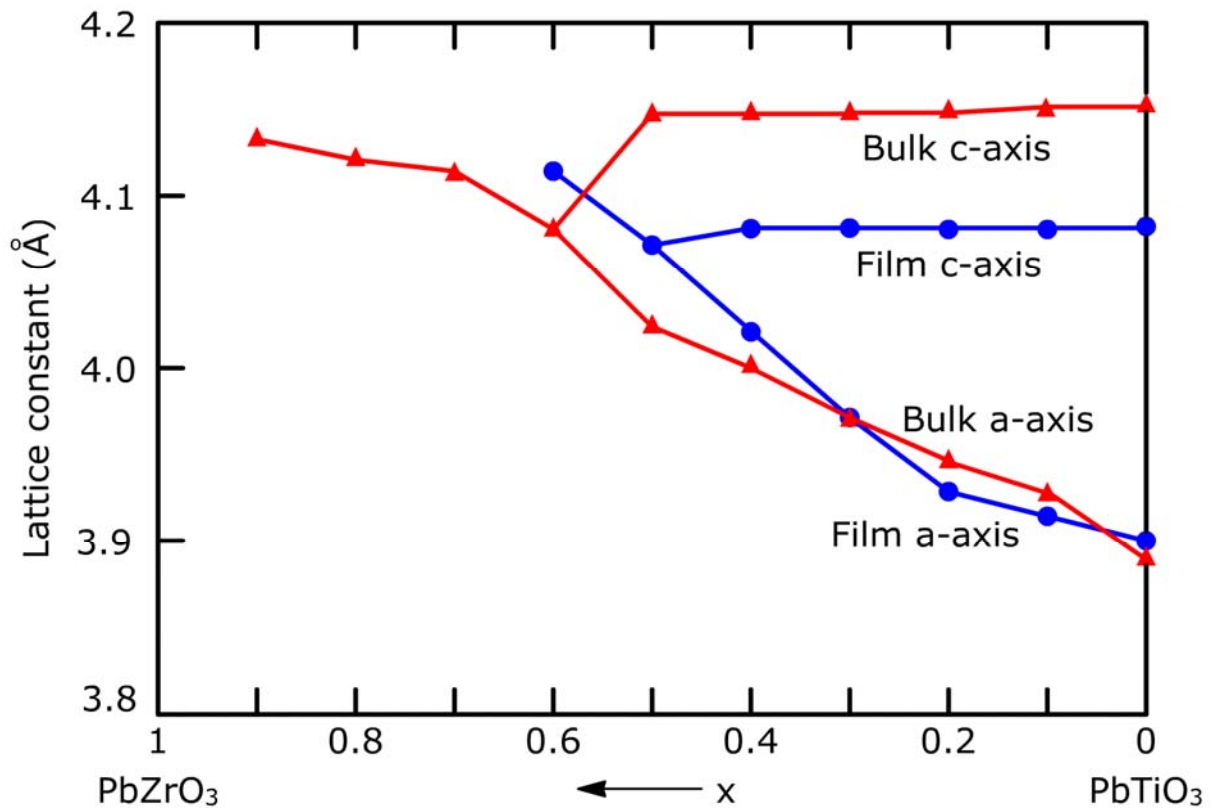


**Figure 2-13:** Lattice parameters of  $\text{Pb}(\text{Zr}_{1-x}\text{Ti}_x)\text{O}_3$  bulk and thin films in dependence on titanium content.

The PZT oxide system is a solid solution of the perovskite ferroelectric  $\text{PbTiO}_3$  and the anti-ferroelectric  $\text{PbZrO}_3$ . Lead zirconate titanates with Zr/Ti ratios of about 92/8 up to 0/100 show ferroelectric phases. Principally, lead zirconate titanate with Zr/Ti ratios in this range can be used in ferroelectric applications.

A lot of research work has been carried out on PZT films with various Zr/Ti composition ratios [17-22]. But practically, as the ferroelectric properties strongly depend on the composition, it is necessary to find the optimum composition for every special application. In general, the PZT films with a 53/47 Zr/Ti ratio (MPB region) have been intensively investigated for memory application, because these films exhibit the largest values of remanent polarization ( $P_r$ ) and the lowest values of coercive field ( $E_c$ ), which are very important for FRAM application [23-25].

The Ti-rich lead zirconate titanate films are also considered to be very attractive for process integration due to their low crystallization temperatures. Therefore, an objective of this work is to prepare Ti-rich PZT films which can be annealed at lower temperatures and to investigate their structural and electrical properties after various annealing treatments.

### 2.6 Strontium Bismuth Tantalate as an Alternative Material for FRAMs

The necessity of the investigation of new materials for memory devices is briefly described in the first chapter of this work. For memory applications, the development of optimum ferroelectric thin film fabrication techniques which are compatible with the latest ULSI manufacturing technologies is of crucial importance, especially in the low-temperature range. Low-temperature growth of ferroelectric thin films can prevent the degradation of the ferroelectrics/metal/semiconductor interfaces or ferroelectrics/insulator/semiconductor interfaces caused by thermal damage and mutual diffusion.

The layered perovskite materials are attractive for memory application because of their low leakage current, good fatigue, retention, and electrical characteristics [1,26,27]. Bismuth oxide layered ferroelectric thin films have attracted considerable attention for application to non-volatile ferroelectric random-access memories because of their good fatigue and retention characteristics comparable with the lead based ferroelectrics [1].

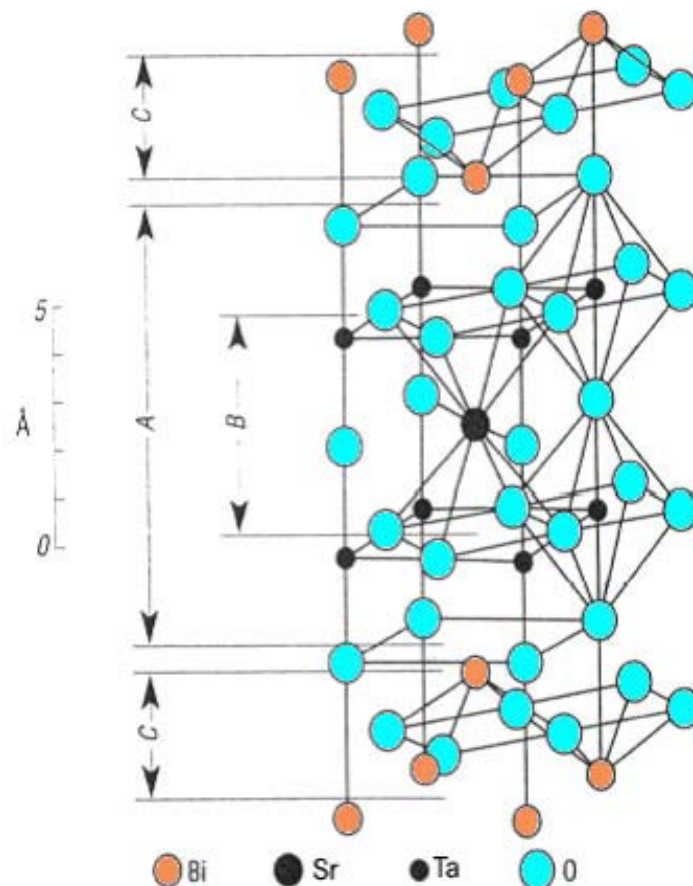


**Figure 2-14:** Unit cell structure of bismuth layered oxide (shown SrBi<sub>2</sub>Ta<sub>2</sub>O<sub>9</sub>).

SrBi<sub>2</sub>Nb<sub>2</sub>O<sub>9</sub> (SBN), SrBi<sub>2</sub>Ta<sub>2</sub>O<sub>9</sub> (SBT), Bi<sub>4</sub>Ti<sub>3</sub>O<sub>12</sub>, and SrBi<sub>4</sub>Ti<sub>4</sub>O<sub>15</sub> are part of so-called Aurivillius phases with general formulas:



where

A = mono-, di-, or trivalent ions,

B = Ti<sup>4+</sup>, Nb<sup>5+</sup>, Ta<sup>5+</sup> etc., single or in combination,

m = 2, 3, and 4 [28,29].

Recently such films have been found to show very high fatigue resistance, especially when applied together with conductive oxide electrodes [30-32].

SBT has a highly anisotropic orthorhombic or pseudotetragonal structure with lattice constants  $a = 5.5306 \text{ \AA}$ ,  $b = 5.5344 \text{ \AA}$ , and  $c = 24.9839 \text{ \AA}$  at room temperature [33]. In this structure, perovskite Sr-Ta-O octahedral blocks are stacked between non-ferroelectric Bi-O layers (figure 2-14). The remanent polarization of this oxide is negligible along the c-axis due to the presence of the non-ferroelectric Bi<sub>2</sub>O<sub>2</sub><sup>2+</sup> layers in the structure, which means that the direction of maximum remanent polarization lies within the a-b plane [33]. This dependence of the ferroelectric properties on the anisotropy makes it essential to study epitaxial SBT films of different crystallographic orientations. Besides, material and electrical properties of the SBT films are known to be sensitive to composition, especially to the content of bismuth in the deposited films [34,35].

At present, the main limitations for the use of SBT films in FRAMs are the limited value of the remanent polarization, the high crystallization temperature of about 800 °C, and the low Curie temperature. These properties make the direct integration of SBT in high density CMOS devices extremely difficult.

The advantages and disadvantages of PZT and SBT based capacitor technologies are:

- PZT based capacitors have a larger switchable polarization (40–60 μC/cm<sup>2</sup>) than the polycrystalline SBT-based capacitors (~10 μC/cm<sup>2</sup>).
- PZT layers with a pure perovskite structure and good electrical properties can be generally produced at lower temperatures (600-700 °C) than SBT layers (750-850 °C) (depending on the particular film deposition technique).
- PZT based capacitors require oxide or hybrid-metal-oxide electrode technologies to yield negligible fatigue and imprint two important electrical properties for FRAMs. Such electrodes are more complicated to fabricate than pure metal electrodes.

- PZT based capacitors involve Pb, which may represent a source for contamination and hazardous and environmental problems.
- SBT based capacitors exhibit negligible fatigue and imprint using the simpler Pt electrode technology.
- SBT layers maintain good electrical properties even when they are very thin ( $< 100$  nm).

The major problems which have to overcome in order to realize high density ferroelectric memory devices are:

- SBT based capacitors have lower polarization values than PZT based capacitors. Intrinsic high polarization values may be necessary to further scaling down capacitors to submicron dimensions.
- The growth of SBT layers with the appropriate layered perovskite structure requires high temperatures (750-800 °C) depending on the film deposition technique. The processing temperatures are rather high as atoms of the electrode metal may diffuse into the bulk silicon giving rise to reduced minority carrier life times.
- The Curie temperature of SBT is low (about 310 °C). A higher Curie temperature is desired for memory applications as the ferroelectric properties are strongly dependent on the Curie temperature. When the operating temperature approaches the Curie temperature the ferroelectric polarization decreases rapidly. Therefore, the Curie temperature should be much higher than the operating temperature to ensure a stable constant polarization.

### 2.7 Electrode Materials for Ferroelectric Capacitors

Platinum (Pt) films are widely used as electrodes for the evaluation of ferroelectric thin films because Pt does not readily form an oxide, also not in an oxidizing ambient. However, platinum has some serious drawbacks with respect to its application. Lead can diffuse into the platinum during the PZT fabrication process [36]. This leads to deviations in the film composition and to a contamination of the integrated circuits of the device. Platinum normally contains the radioactive isotope  $\text{Pt}^{190}$  with a concentration of 0.01%. This  $\text{Pt}^{190}$  isotope emits an alpha particle with a kinetic energy of 3.18 MeV. By local ionization an  $\alpha$ -particle can change the charge stored in a DRAM capacitor, thereby inducing soft errors [37]. The  $\text{Pt}^{190}$  isotopes can be removed to obtain non-radioactive platinum.

Recently, iridium (Ir) has become a promising candidate as ferroelectric capacitor electrode material. In the case of PZT formed on an iridium substrate, lead can not diffuse into the iridium layer [36]. The barrier effect has been explained by the formation of iridium oxide at the surface. A radioactive isotope of iridium does not exist. As no  $\alpha$ -radiation is emitted, the probability of soft errors occurring in DRAMs with ferroelectric materials is expected to be reduced drastically by using Ir electrodes.

Furthermore, Ir electrodes improve endurance properties (switching of the polarization (see section 2.4)) of ferroelectric structures in comparison to platinum electrodes by about two orders of magnitude [38].

Thus, iridium appears to be superior to platinum with regard to its application as electrode layer in ferroelectric storage devices.

---

## ***Chapter 3 Liquid Delivery Metalorganic Chemical Vapour Deposition Technique***

In this chapter the experimental equipment used for the deposition of thin ferroelectric PZT and SBT films and the main principles of the liquid delivery metalorganic chemical vapor deposition (LD-MOCVD) are described.

### ***3.1 Introduction***

Ferroelectric thin-film technology has been investigated intensively since the 1960s because of the promising properties of ferroelectric materials for the application to nonvolatile memory devices. In particular, PZT based destructive readout ferroelectric random access memories (DRO FRAMs) have received great attention because of their low operating voltage, their radiation hardness and their high-speed. Currently, mega-bit density FeRAMs have been successfully fabricated on a research level; low-density FeRAMs (below 256 kbit) are already commercially available [39-41].

In order to be compatible to the generally used semiconductor processes, the PZT processing temperature should be decreased below 550 °C. But typical annealing temperatures of PZT films with a ratio of Zr/Ti of about 53/47 are ranging from 650 °C to 750 °C. At an annealing temperature lower than 550 °C, PZT films usually do not exhibit well pronounced hysteresis loops as the formation of the perovskite phase is insufficient [42]. Thus, it is desirable to develop a low temperature processing which improves the integration of PZT films in high density CMOS devices.

For the deposition of ferroelectric thin films, a plenty of techniques, such as activated reactive evaporation [43], sputtering (ion-beam, RF diode, RF magnetron) [44], laser ablation [45], sol-gel [46], metalorganic decomposition (MOD) and metalorganic chemical vapor deposition (MOCVD) [47] have been reported. Among these techniques, the MOCVD method has an excellent potential because of its good compositional control, its high film density, high film uniformity, high deposition rate, possibility of low processing temperature and its good compatibility to Si ultra large scale integration (ULSI) processes. Moreover, MOCVD can offer good step coverage characteristics, which are very important for deposition on three-dimensional surfaces.

Unlike conventional CVD, PZT MOCVD has the fundamental problem that a stable delivery of precursors is hard to achieve with conventional bubbler technology [48-51].

The volatility of precursors can be enhanced by elevating the temperature of the delivery system to about 200°C. Precursors, however, tend to degrade gradually at elevated temperatures for extended periods becoming nonvolatile. Furthermore, the vapor pressure in the bubbler varies with time, and, therefore, a constant delivery is hard to achieve [52]. In order to overcome these limitations, liquid delivery has been suggested and exhibits promising results, although it still requires a higher reproducibility for mass production [53-55]. In order to realize a reliable PZT film deposition process, the impact of process parameters on deposition was investigated in this study.

Over the years, various deposition techniques for preparing SBT films have been studied including sputtering, laser ablation, metalorganic deposition (MOD), liquid source misted chemical deposition (LSMCD), and metalorganic chemical vapor deposition (MOCVD) [56-60]. Although SBT films prepared by MOD method have shown excellent properties, it is essential to study the MOCVD technique in order to improve the integrability into a silicon device process. MOCVD offers the advantages of good conformability, excellent step coverage, and thickness uniformity. However, most of the MOCVD-grown SBT thin films suffer from a composition of Bi, Sr, and Ta atoms which is not the desired one. This is due to the complexity of this ternary system.

To solve this problem, liquid delivery systems such as the TriJet system have been studied (TriJet is a system of Aixtron AG). The structure of Bi-layered ferroelectrics has the general formula  $(\text{Bi}_2\text{O}_2)^{2+}(\text{A}_{m-1}\text{B}_m\text{O}_{3m+1})^{2-}$ . This means, SBT films consist of  $\text{SrTa}_2\text{O}_7$  perovskite and  $\text{Bi}_2\text{O}_2$  layers. A new precursor, strontium-bis[tantalum(pentaethoxide)(2-methoxyethoxide)]  $\text{Sr}[\text{Ta}(\text{OEt})_5(\text{OC}_2\text{H}_4\text{OMe})]_2$ , has already the desired ratio of Sr and Ta atoms within itself; this may assist the formation of the perovskite structure ( $\text{SrTa}_2\text{O}_7$ ) in the SBT films.

### **3.2 Experimental Equipment**

The film deposition was carried out in an AIXTRON Tricent MOCVD system.

Conventional CVD processes using gaseous precursors generally offer easy composition control, uniform deposition over large areas and good step coverage. Unless appropriate gaseous precursors are available – as for the metals of ferroelectric materials – solid/liquid metalorganic compounds are used as sources (MOCVD). Many of them are characterised by low volatility, low thermal stability and instability in air.

In classical MOCVD, the precursors are stored in containers, which are heated to a precisely controlled temperature. The vapour obtained is then transported by a carrier gas through heated gas lines to the heated substrate in the reaction chamber. However, many complex precursor sources, e.g. those for PZT, SBT or bismuth lanthanum titanate (BLT), change their evaporation rates if heated over an extended period of time, leading to irreproducible process results.

Liquid precursor delivery systems have been developed in order to overcome this deterioration problem. It was proved that such thermal instability issues were overcome by direct introduction of liquid precursors or precursor solutions (dissolved in an appropriate solvent) kept at ambient temperature prior to injection into a heated vaporiser. However, most of the commercial vaporiser concepts rely on evaporation via direct contact to a heated surface, often leading to undesirable particle formation and memory effects. Therefore, non-contact evaporation seems to be a key element to ensure reproducible film formation.

The Aixtron MOCVD system uses a delivery and evaporation unit (TriJet™), developed by the French company J.I.P.ELEC, which has proved to give a stable performance over time. The module enables highly repeatable film depositions that satisfy the stringent requirements of full-scale production. In contrast to other commercial systems which have been thoroughly evaluated by AIXTRON, the TriJet™ system offers repeatable performance which is primarily based on a contactless evaporation of the precursor materials completely avoiding residual material on a hot (evaporating) surface. It has been observed that residual material may give cause to the creation of particles and to "memory effects", negatively affecting the repeatability of results. In the TriJet™ system, the precursors are injected into the evaporator in precisely controlled doses and are efficiently evaporated without any residue. The amount of liquid injected into the evaporator is precisely controlled by fine adjustments of the opened valve. The opening time of the injectors can be varied from 0.5 to 10000 ms and the opening frequency from 0.1 to 50Hz, respectively. The TriJet Liquid Precursor Delivery and Evaporation System module is part of the AIXTRON Tricent MOCVD System.

Aixtron's Atomic Vapour Deposition (AVD) is a unique MOCVD based deposition concept. Non-surface-contact evaporation is achieved by controlled injection of small quantities of (diluted) liquid precursors into the heated carrier gas prior to entering the cold wall Tricent® reactor chamber (figures 3-1 and 3-2).



**Figure 3-1:** TriJet™ injector.



**Figure 3-2:** Photo of Tricent® reactor (AIXTRON AG).

### 3.2.1 Equipment Advantages

The used 150 mm single wafer MOCVD reactor system offers the following features:

- atomic precision of layer composition by controlled micro-droplet injection of metalorganic precursor solutions;
- long term process stability by direct evaporation of droplets in the heated carrier gas, avoiding particle and memory effects of hot surface-evaporation systems;
- effective utilization of the precursors by cold wall design and by room temperature storage of precursor solutions;
- availability of a manual wafer load lock or a high throughput cluster tool (for production) in order to avoid contact to room ambient.

### 3.2.2 Equipment Setup

For PZT and SBT growth, three independently controlled precursor injectors were used, one for each metal, i.e. in the case of PZT one for lead, one for zirconium and one for titanium and in the case of SBT one for strontium-tantalum and one for bismuth precursor (figure 3-3).

In this way, the important lead (Pb) content in the PZT-layer could be optimized for the best electrical performance as well as the bismuth (Bi) content in the SBT films.

A dual-flow, temperature-controlled showerhead, shown in the figure 3-4, was used for separate and highly reproducible introduction of precursors and oxide agents. Thus, the metal precursors can react with oxygen only on the substrate surface and the formation of unwanted products can be neglected.

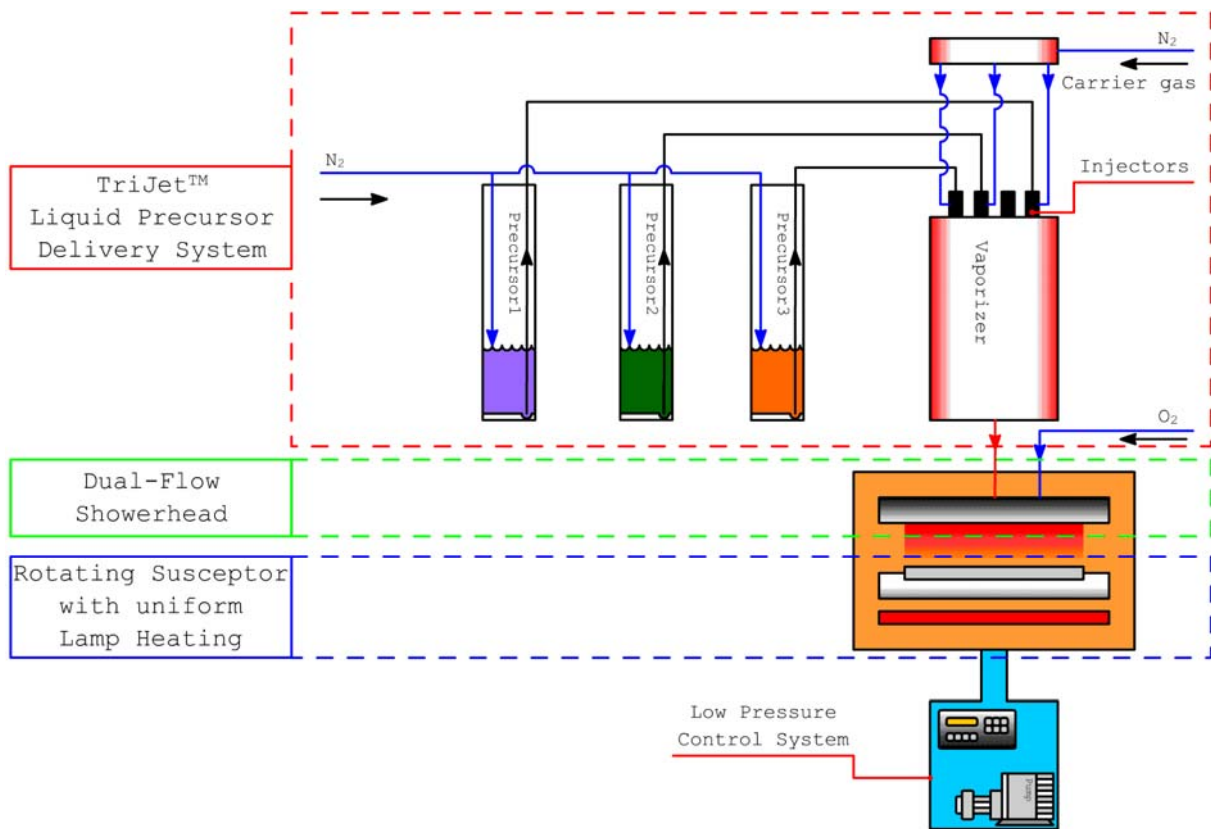


**Figure 3-3:** Block diagram of process module.

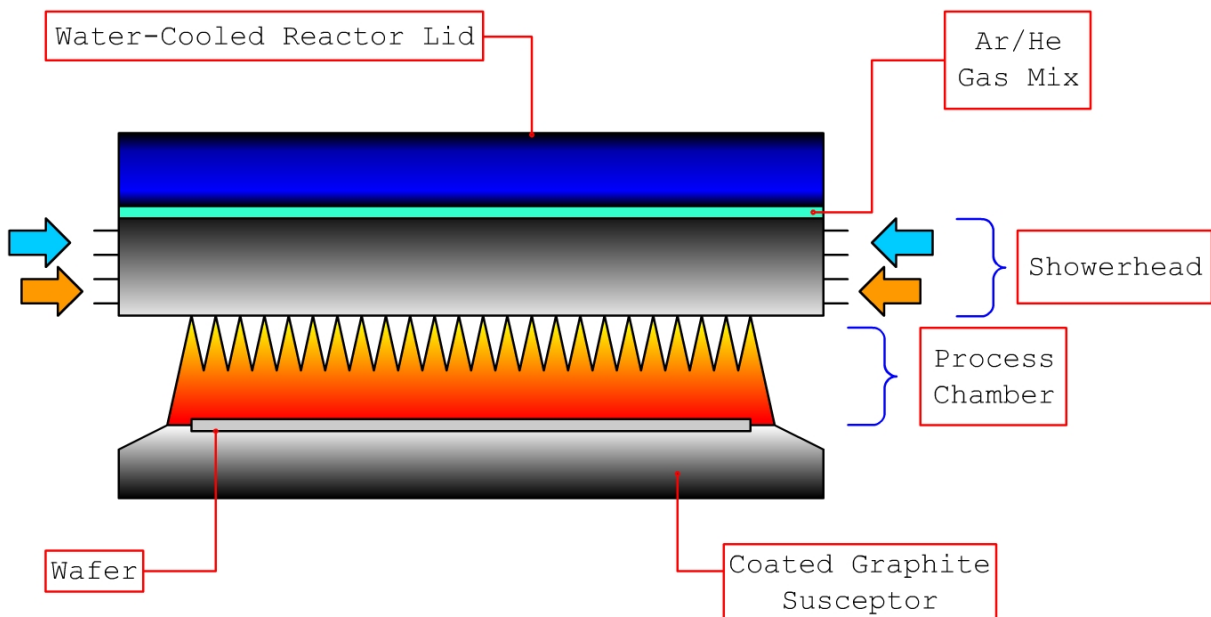


**Figure 3-4:** Dual-flow showerhead.

### 3.3 Selection of the Precursors for PZT Film Deposition

Promising characteristics of metal organic chemical vapor deposition (MOCVD), such as better step coverage, easy scale-up, and easy control of composition and thickness, have led to the conclusion that the MOCVD technique may be the best suited for the commercial production of thin ceramic films. This technique, however, relies largely on the availability of precursors of high volatility, low toxicity, and adequate stability. The list of most utilized precursors for MOCVD and their properties are listed in Table 3-1.

A lead alkyl such as tetraethyllead,  $\text{Pb}(\text{Et})_4$  (figure 3-5), has been used as the lead source because of its high volatility and its high vapor pressure. Furthermore,  $\text{Pb}(\text{Et})_4$  is not sensitive to light, air and moisture. Lead alkoxides and carboxylates are known to hydrolyze easily. Lead  $\beta$ -diketonates are rather stable and less toxic, but also less volatile.

Zr-precursors used for MOCVD of  $\text{Pb}(\text{Zr,Ti})\text{O}_3$  include zirconium alkoxides, zirconium  $\beta$ -diketonates and fluorinated  $\beta$ -diketonates. Although many of the problems associated with the vapour-phase transport of these low vapour pressure precursors can be solved by the use of liquid injection MOCVD, there remain a number of drawbacks associated with their use.

**Table 3-1.** Representative volatile MOCVD precursors used in PZT thin-film deposition and their vaporization properties. [53]

Compound	Phase	Melting point ( °C)	Vapor pressure
$(\text{C}_2\text{H}_5)_4\text{Pb}$	Liquid	-136	2.00 torr at 50 ° C
$\text{Pb}(\text{TMHD})_2$	Solid	126-128	0.05 torr at 180 ° C
$(\text{C}_6\text{H}_5)_4\text{Pb}$	Solid	229-230	0.05 torr at 230 ° C
$\text{Ti}[\text{OCH}(\text{CH}_3)_2]_4$	Liquid	19	5.00 torr at 92 ° C
$\text{Ti}[\text{OC}(\text{CH}_3)_3]_4$	Liquid		0.20 torr at 70 ° C
$\text{Ti}[\text{OC}(\text{CH}_3)_3]_2(\text{TMHD})_2$	Solid	220	1.00 torr at 240 ° C
$\text{Zr}[\text{OC}(\text{CH}_3)_3]_4$	Liquid		1.00 torr at 65 ° C
$\text{Zr}(\text{TMHD})_4$	Solid	308	0.10 torr at 180 ° C

For example, the  $\beta$ -diketonates  $\text{Zr}(\text{acetylacetonate})_4$  and  $\text{Zr}(\text{trifluoroacetylacetonate})_4$  lead to carbon or fluorine incorporation into the film, respectively [54]. Although higher purity  $\text{ZrO}_2$  can be deposited from  $\text{Zr}(\text{thd})_4$  (thd = 2,2,6,6,-tetramethyl-3,5-heptanedionate) [55,61], the high thermal stability of the precursor demands substrate temperatures higher than 600 °C in order to obtain a diffusion controlled oxide growth. Such high deposition temperatures are incompatible with the low growth temperatures (lower than 500 °C) required for the majority of microelectronics applications.

The high thermal stability of  $\text{Zr}(\text{thd})_4$  relative to  $\text{Pb}(\text{Et})_4$  can also lead to problems during the growth of  $\text{Pb}(\text{Zr,Ti})\text{O}_3$  by liquid injection MOCVD. The high substrate temperature required to optimise oxide deposition from  $\text{Zr}(\text{thd})_4$  results in a loss of lead in the film by desorption. The use of a higher Zr precursor flow rate or an increased evaporator temperature in order to enhance Zr incorporation at lower substrate temperatures leads either to the blocking of the reactor lines with  $\text{Zr}(\text{thd})_4$  or the decomposition of  $\text{Pb}(\text{Et})_4$  in the evaporator.

Alternative zirconium oxide precursors are required, which are more volatile than  $\text{Zr}(\text{thd})_4$  and which also have a lower thermal stability, more compatible to  $\text{Pb}(\text{Et})_4$ . Zirconium alkoxides (figure 3-6),  $\text{Zr}(\text{OR})_4$  ( $\text{R}=\text{Pr}^i, \text{Bu}^t$ ), mostly satisfy these requirements because of their significantly lower thermal stability and higher volatility in comparison to  $\text{Zr}(\text{thd})_4$ .

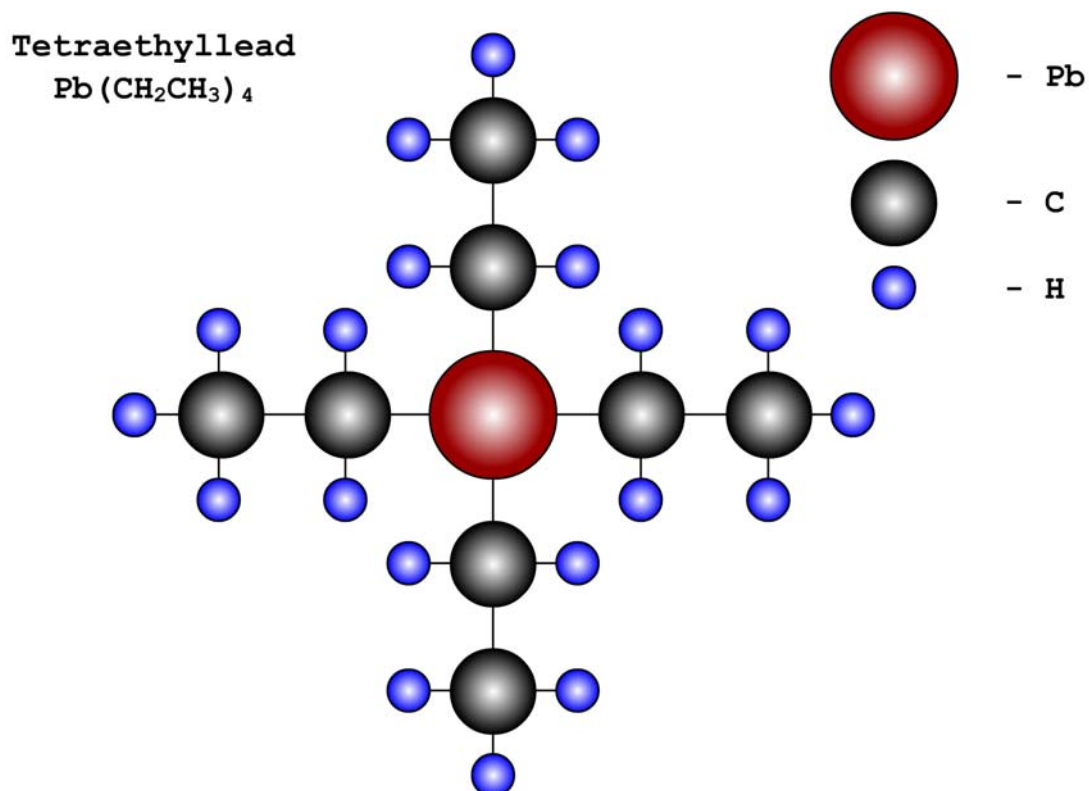


**Figure 3-5:** Molecular structure of tetraethyllead.

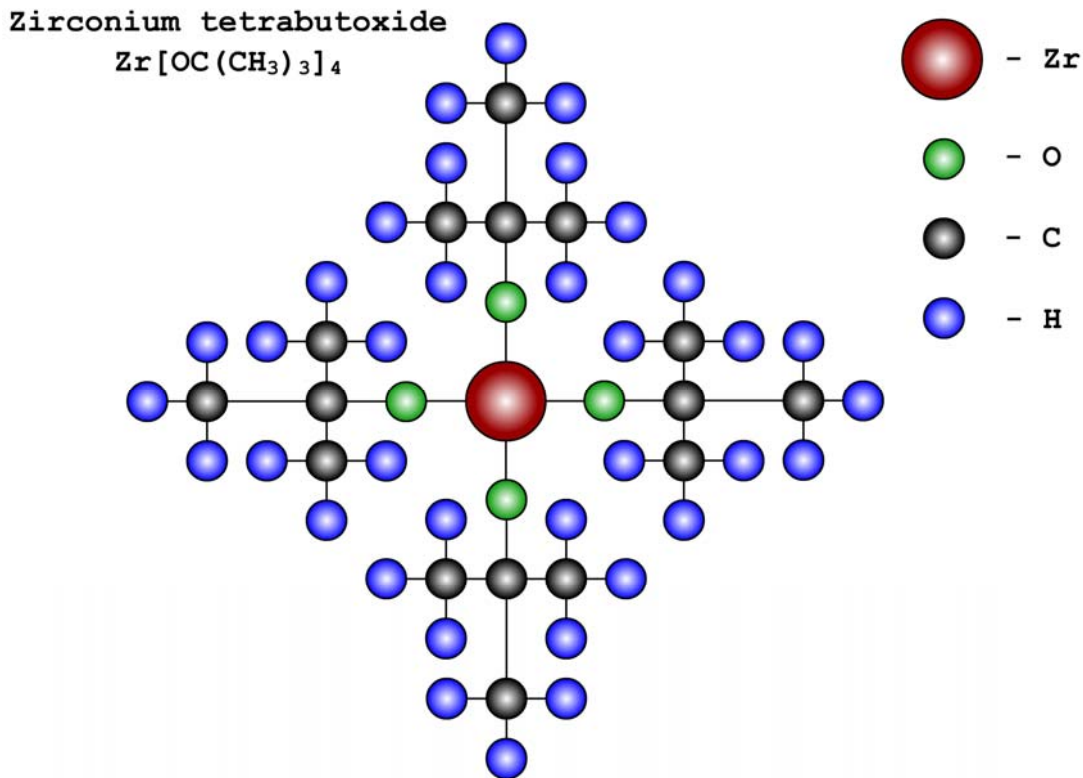


**Figure 3-6:** Molecular structure of zirconium tetrabutoxide.

Only their high sensitivity to air and moisture which may also result in a reduced shelf-life (the length of time for which a precursor may be stored without becoming unsuitable for use) must be taken into account in solution-based liquid injection MOCVD applications.

The MOCVD of  $TiO_2$  has been studied using a variety of precursors, focusing primarily on titanium tetrachloride ( $TiCl_4$ ) plus water or titanium alkoxides [ $Ti(OR)_4$ , where R=ethyl or isopropyl] [62].

Besides the contamination of the deposited films with Cl, titanium tetrachloride is very irritating to the eyes, skin, mucous membranes, and the lungs. Breathing in large amounts can cause serious injury to the lungs. The formation of hydrochloric acid during hydrolysis of titanium tetrachloride is an additional drawback of this precursor:



As it can be seen in a Table 3-1, the vapor pressure of the  $Ti(OBu^t)_4$  is not high enough for MOCVD in comparison to Pb- and Zr-precursors.

Alkoxide precursors, such as the titanium tetra isopropoxide (TIP) (figure 3-7) which is used in this study, are very volatile at low temperature and the contamination from TIP is small.

**Titanium isopropoxide**  
 $\text{Ti}[\text{OCH}(\text{CH}_3)_2]_4$

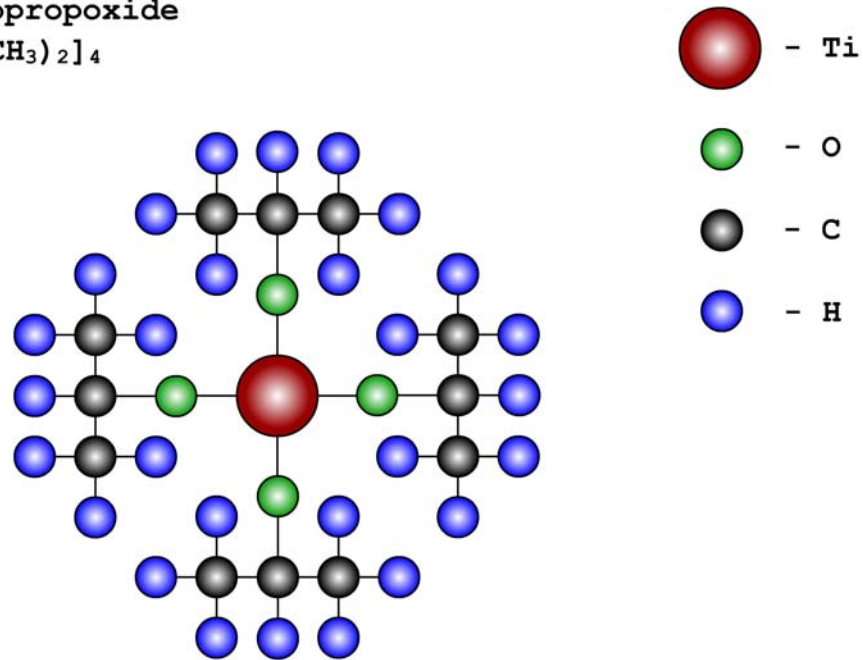


**Figure 3-7:** Molecular structure of titanium isopropoxide.

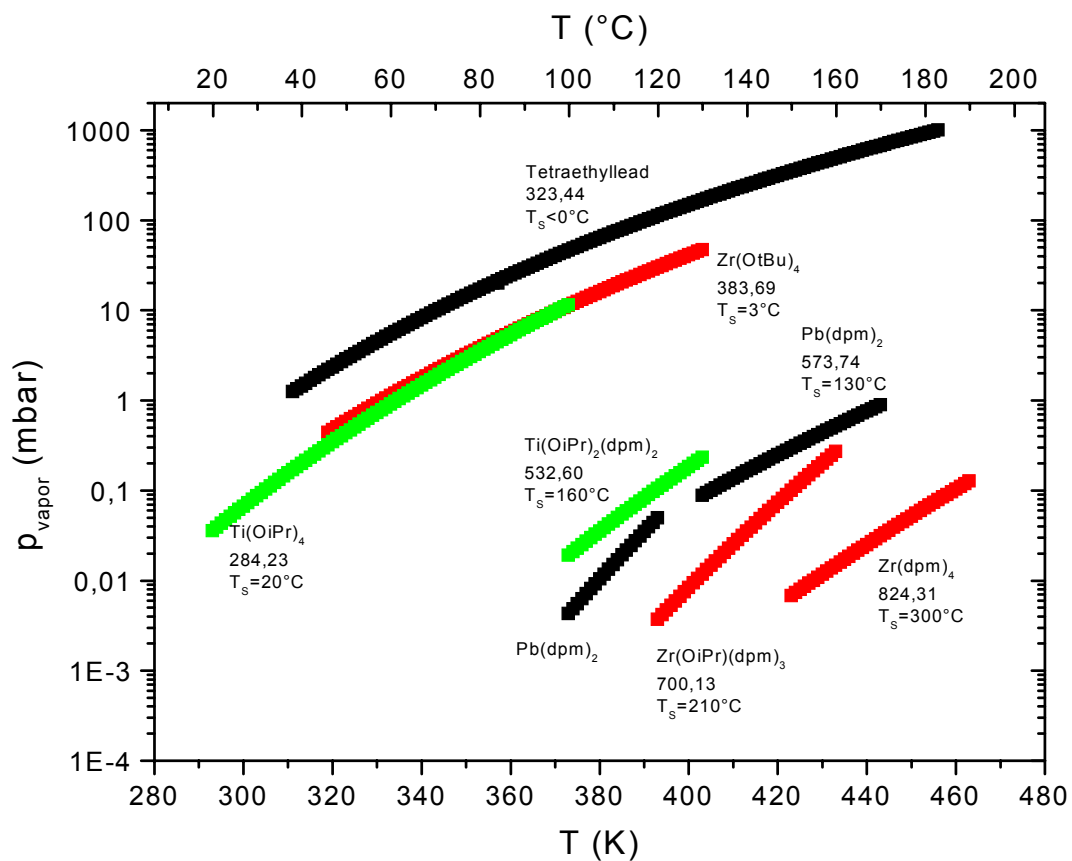


**Figure 3-8:** Dependencies of the vapour pressure on the ambient temperature of different precursors.

Air- and moisture-sensitive precursors require an inert atmosphere for their handling. TIP decomposes into solid metal oxide TiO with water and isopropanol as vapor by-products [63].

The important properties of the precursors such as melting-points and molecule masses can be determined from the “vapor pressure-temperature” dependencies which can be seen in figure 3-8.

This figure shows the process parameters which are required to transfer the precursors from the liquid to the gas phase. TIP (green) and Zr(OBu<sup>t</sup>)<sub>4</sub> (red) coincide in the figure. The vapor pressure of the Pb(Et)<sub>4</sub> at a fixed temperature is definitively higher than those of the shown Ti- and Zr-precursors. This fact indicates that the phase transfer of tetraethyllead needs to be performed at lower temperatures.

## **Chapter 4 Experimental Procedure**

This chapter describes in detail the deposition parameters of PZT and SBT films and the main techniques used for structural and electrical characterization of the deposited films.

### **4.1 Deposition of Single-Metal-Oxide Films**

Before starting the deposition of the ferroelectric films consisting of three-metal oxides, the pressure and the temperature dependencies of the deposition rates of each single metal oxide component were investigated. Deposition of the single-metal-oxide films was carried out in order to get more insight into the deposition processes and to find a common process window.

Single metal oxides PbO, ZrO<sub>2</sub> and TiO<sub>2</sub> films were deposited by LD-MOCVD using tetraethyllead - Pb(Et)<sub>4</sub>, zirconium tetrabutoxide - Zr(OBu<sup>t</sup>)<sub>4</sub> and titan isopropoxide – TIP precursors, respectively. Deposition rate and homogeneity across the wafer of the PbO, ZrO<sub>2</sub> and TiO<sub>2</sub> films were investigated as a function of deposition temperature and pressure in the reactor.

In order to estimate the SBT deposition rate and elemental composition, the MOCVD process was investigated for the Bi precursor and the Sr-Ta precursor in different runs. Triallylbismuth, triphenylbismuth, or tributylbismuth, and strontium bis[tantalum (pentanethoxy)(2-methoxyethoxide)] (Sr-Ta) were used as Bi precursors and as Sr-Ta precursor, respectively.

Investigation of the temperature and pressure dependencies of the deposition rates of bismuth oxide and strontium tantalate oxide was made using the MOCVD system shown in figure 4-1.

A liquid delivery system (LDS) was used to supply and to vaporize the precursor into the reactor. The flows of the precursors were adjusted using liquid flow controllers (LFC). The temperature of the evaporator was varied from 140 °C to 180 °C.

The precursor vapors were carried by nitrogen gas set to a flow rate of 50 sccm to the hot-box that was heated to 160 °C where they were mixed with the oxygen which was supplied with a flow rate of 50 sccm. The flows of the gases were controlled by mass flow controllers (MFC). The connecting lines between the evaporator, the hot-box, and the reactor were heated to 160 °C in order to prevent the condensation of the precursor.

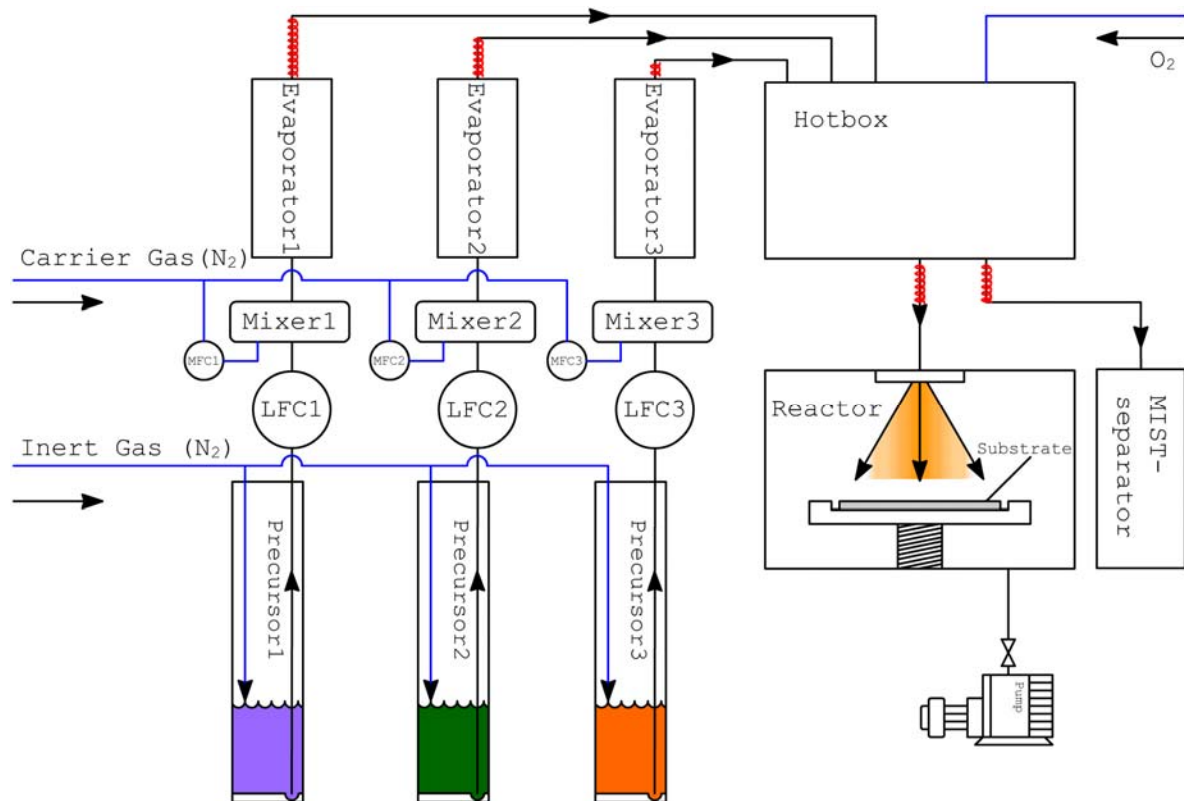


**Figure 4-1:** Schematic diagram of MOCVD system.

The deposition zone was resistively heated to the deposition temperatures ranging from 350 to 650 °C. The MOCVD reactor was equipped with a vacuum pump system and a motor driven pendulum valve to adjust the pressure during the deposition process in a range between 0.35 and 7 mbar. During the film deposition, the reactor wall temperature was kept between 60 and 80 °C. The deposition conditions are summarized in table 4-1.

**Table 4-1.** Deposition conditions of bismuth oxide and strontium tantalate oxide thin films.

Bi-1 (0.05 M) precursor	Triphenylbismuth $\text{Bi}(\text{C}_6\text{H}_5)_3$ in toluene(0.05mol/l)
Bi-2 (0.05 M) precursor	Triallylbismuth $\text{Bi}(\text{CH}_2\text{CH}=\text{CH}_2)_3$ in toluene (0.05 mol/l)
Bi-3 precursor	Tributylbismuth ( $\text{Bi}(\text{C}_4\text{H}_9)_3$ ) pure
Sr-Ta (pure or 0.05 M) precursor	Strontium bis[tantalum(pentan-ethoxy) (2-methoxyethoxide)] $\text{Sr}[\text{Ta}(\text{OEt})_5(\text{OC}_2\text{H}_4\text{OMe})_2]$ pure or in toluene (0.05 mol/l)
Deposition temperature	350 – 650°C
Deposition pressure	0.35 – 7 mbar
Vaporizer temperature	140 – 200°C
Carrier ( $\text{N}_2$ )gas flow rate	25 – 250 sccm
Reactant gas flow rate	25 – 250 sccm
Precursor flow rate	0.1 – 2 g/h

In result, the optimum conditions for the deposition of PZT films as well as SBT films were determined.

#### **4.2 Deposition of the Ferroelectric Thin PZT Films by LD-MOCVD**

Film deposition was carried out in a Tricent<sup>®</sup> CVD reactor (AIXTRON AG). The MOCVD apparatus is equipped with a precisely controllable TriJet<sup>™</sup> system, which allows carrying out a "flash"-evaporation of a liquid precursor. Using of a non-contact evaporation system and a temperature-controlled twin-flow-showerhead allows the Tricent<sup>®</sup> equipment to provide a separate and highly reproducible supply of precursors and oxidation agents.

Organometallic compounds, such as tetraethyl lead ( $\text{Pb}(\text{C}_2\text{H}_5)_4$ ), zirconium tert-butoxide ( $\text{Zr}[\text{OC}(\text{CH}_3)_3]_4$ ) and titanium isopropoxide ( $\text{Ti}[\text{OCH}(\text{CH}_3)_2]_4$ ) were used as precursors. They were diluted by toluene as solvent with a concentration of 0.1M, 0.05M and 0.1M (M=mol), respectively. The precursors were stored in separate containers and not mixed. All these precursors are in the liquid phase at room temperature; the evaporation temperature of each of these is relatively low. A liquid delivery system (LDS) was used to supply the precursor to the vaporizer, the Trijet system. The precursor solution was vaporized in the evaporator, which was gradually heated from 110 °C at the inlet up to 150 °C at the outlet. Then the vapor passed the showerhead and was delivered into the reactor. In the presence of oxygen gas, adsorption and dissociation of the precursors at the substrate surface took place and the metal oxide film grew on the hot surface. The use of a showerhead supports to obtain an uniform distribution of the precursors across the wafer surface.

The short piping between evaporator and reactor was heated to 150 °C in order to prevent the condensation of the precursors. Since the temperature difference between condensation and dissociation of the precursor molecules is very small, the susceptor and all others surfaces of reactor, like top plate, reactor walls and showerhead, are precisely temperature controlled.

To obtain PZT thin films with high homogeneity the substrate was rotating during the process with 8 rounds per minute.

The substrate was heated to a temperature of 450 °C and the pressure in the reactor during deposition process was adjusted to 0.5 mbar up to 1.5 mbar. As the highest film thickness homogeneity across the wafer surface was obtained at a pressure of 0.5 mbar, this pressure was chosen for most of the deposition experiments.

PZT films were deposited on an Ir/Ti (100/10 nm) electrode which was evaporated on a 150 mm oxidized Si(100) wafer using PVD. Typical experimental conditions and introduction sequences of metalorganic sources for PZT thin film fabrication at the substrate temperature of 450 °C are shown in figure 4-2.

Substrate:	Ir/Ti/SiO <sub>2</sub> /Si(100) (100/10/200 nm)
Substrate temperature:	450 °C
Reactor pressure:	0.5 mbar
Vaporizer temperature:	110 - 150 °C
Pb source:	Pb(C <sub>2</sub> H <sub>5</sub> ) <sub>4</sub> 0.1 M
Zr source:	Zr[OC(CH <sub>3</sub> ) <sub>3</sub> ] <sub>4</sub> 0.05 M
Ti source:	Ti[OCH(CH <sub>3</sub> ) <sub>2</sub> ] <sub>4</sub> 0.1 M
Solvent:	Toluene
Oxidation gas:	O <sub>2</sub> 100 sccm
Transport gas:	N <sub>2</sub> 100 sccm

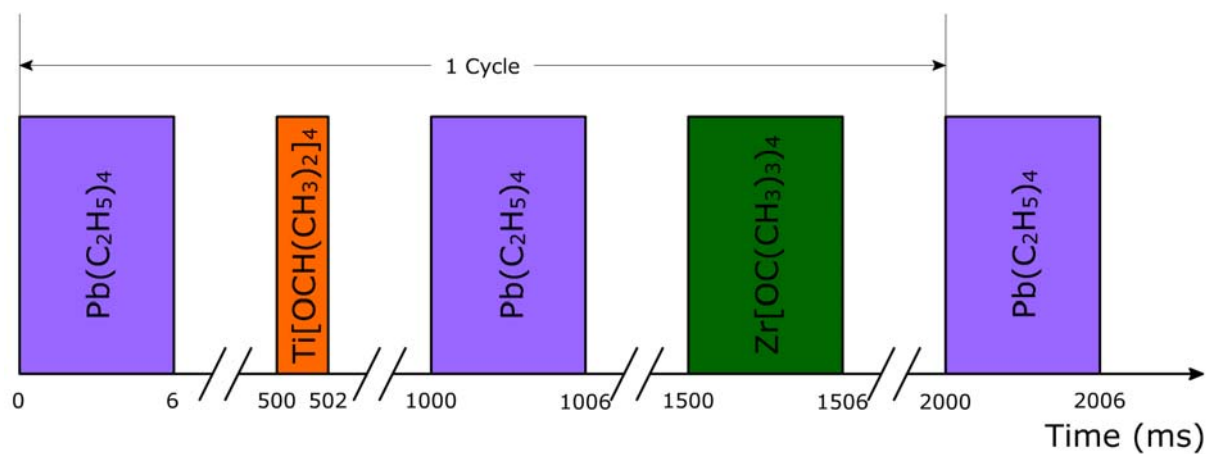


**Figure 4-2:** Typical experimental conditions and introduction sequence for PZT film deposition.

To obtain a suitable stoichiometry of PZT films, the injection parameters, such as impulse frequency and duration of the impulses, were varied.

#### 4.3 LD-MOCVD of the Ferroelectric Thin SBT Films

First SBT films were deposited using the laboratory MOCVD system described in section 4.1. Triphenylbismuth (Bi-1), triallylbismuth (Bi-2), or tributylbismuth (Bi-3), and strontium bis[tantalum (pentan-ethoxy)(2-methoxyethoxide)] (Sr-Ta) were used as Bi precursors and as Sr-Ta precursor, respectively. These three different bismuth precursors (Bi-1, Bi-2, or Bi-3) were used together with the same Sr-Ta precursor for three different SBT (SBT-1, SBT-2, and SBT-3) depositions. SBT thin films were deposited on 150 mm silicon

(100), Pt/TiO<sub>x</sub>/SiO<sub>2</sub>/Si or Ir/TiO<sub>x</sub>/SiO<sub>2</sub>/Si substrates by liquid-delivery MOCVD. A TiO<sub>x</sub> layer improves adhesion and electrical contact to the underlying silicon [64].

The flows of the precursors were adjusted using liquid flow controllers (LFC) with the aim to obtain SBT film with a suitable compositional ratio. Substrate temperature and reactor pressure were varied in the range between 350 °C and 650 °C and from 1.5 to 15 mbar, respectively. Nitrogen carrier gas was used to transport each source gas into the reactor. Oxygen gas was supplied with constant flow rate into the hot-box to form the three component oxide. The deposition conditions are summarized in table 4-2.

**Table 4-2.** Deposition conditions of SBT thin films.

Bi-1 (0.05 M) precursor	Triphenylbismuth Bi(C <sub>6</sub> H <sub>5</sub> ) <sub>3</sub> in toluene(0.05 mol/l)
Bi-2 (0.05 M) precursor	Triallylbismuth Bi(CH <sub>2</sub> CH=CH <sub>2</sub> ) <sub>3</sub> in toluene (0.05 mol/l)
Bi-3 precursor	Tributylbismuth (Bi(C <sub>4</sub> H <sub>9</sub> ) <sub>3</sub> ) pure
Sr-Ta (pure or 0.05 M) precursor	Strontium bis[tantalum(pentan-ethoxy) (2-methoxyethoxide)] Sr[Ta(OEt) <sub>5</sub> (OC <sub>2</sub> H <sub>4</sub> OMe)] <sub>2</sub> pure or in toluene (0.05 mol/l)
SBT-1 precursor	Bi-1 in toluene (0.1 mol/l) and Sr-Ta in toluene (0.05 mol/l)
SBT-2 precursor	Bi-2 in toluene(0.1 mol/l) and Sr-Ta in toluene (0.05 mol/l)
SBT-3 precursor	Bi-3 pure and Sr-Ta pure
Deposition temperature	350 – 600°C
Deposition pressure	0.35 – 7 mbar
Vaporizer temperature	140 – 200°C
Carrier (N <sub>2</sub> )gas flow rate	25 – 250 sccm
Reactant gas flow rate	25 – 250 sccm
Precursor flow rate	0.1 – 2 g/h
Deposition time	10 – 60 min

SBT thin films were also prepared on the AIXTRON Tricent MOCVD system using the novel double metal alkoxide precursor, strontium-bis[tantalum(pentaethoxide)(2-methoxyethoxide)]. Tributylbismuth (Bi(C<sub>4</sub>H<sub>9</sub>)<sub>3</sub>) was used as the bismuth precursor because the growth rate of bismuth oxide and SBT thin films deposited from triphenylbismuth and triallylbismuth were relatively low. Both precursors were diluted by toluene as solvent with a concentration of 0.1M and were stored in separate containers.

The deposition temperature was in the range between 300 °C and 550 °C and the deposition pressure was varied from 0.4 to 15 mbar. The injection parameters, such as impulse frequency and duration of the impulses, were varied with the purpose of obtaining the SBT thin films with good structural and ferroelectric properties.

Typical experimental conditions and introduction sequences of the metalorganic sources for SBT thin film fabrication are shown in figure 4-3.

Substrate:	Ir/TiO <sub>2</sub> /SiO <sub>2</sub> /Si(100) (100/10/200 nm)
Substrate temperature:	400 °C
Reactor pressure:	0.4 mbar
Vaporizer temperature:	150 °C
Bi source:	Bi(C <sub>4</sub> H <sub>9</sub> ) <sub>3</sub> 0.1 M
Sr/Ta source:	Sr[Ta(OEt) <sub>5</sub> (OC <sub>2</sub> H <sub>4</sub> OMe)] <sub>2</sub> 0.1 M
Solvent:	Toluene
Oxidation gas:	O <sub>2</sub> 500 sccm
Transport gas:	N <sub>2</sub> 100 sccm

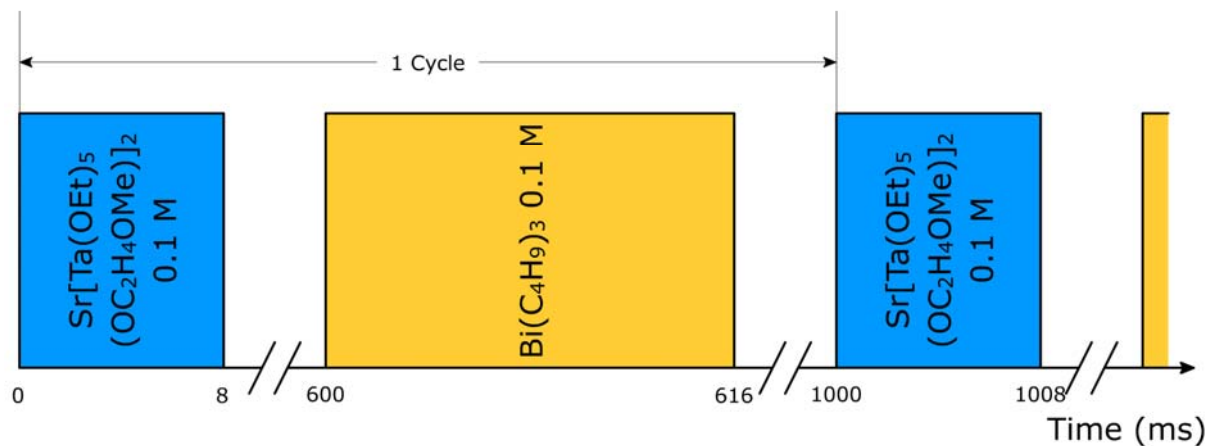


**Figure 4-3:** Typical experimental conditions and introduction sequence for SBT film deposition.

After deposition, the films were annealed for 15 minutes in oxidizing atmosphere at temperatures ranging from 500 °C to 1000 °C with the object to crystallize the as-deposited amorphous SBT films.

#### 4.4 Fabrication of Substrate Wafers

Cleaning processes are one of the key factors in achieving higher yield. About 80% of defects are due to particles on the substrate surface, which can be removed to a high extent by use of special cleaning agents. Therefore, prior to a growth or deposition process step the wafer surface has to be treated in a wet cleaning ambient.

Several wet cleaning steps are necessary to remove particles and contaminations from the substrate surface. During the last years wet chemical cleaning steps have been modified only slightly. It is common to these processes that water is used as solvent for the cleaning chemicals.

#### 4.4.1 Wet Cleaning of the Silicon Wafers

Immersion bath cleaning with Caro's acid removes organic and metallic contaminations and particles, while a dip in diluted hydrofluoric acid removes the thin oxide layer on the substrate surface and the metallic contaminations in this oxide layer. Rinsing with DI-water removes the cleaning chemicals from the substrate surface.

Wet immersion bath cleaning of the substrate surfaces, which was applied to the wafer, embraces the following steps:

##### 1. Caro's acid

Caro's acid is a mixture of 2 parts of concentrated sulfuric acid (96%) and 1 part of hydrogen peroxide (30%). The resultant solution is an equilibrium composition containing  $\text{H}_2\text{SO}_5$ ,  $\text{H}_2\text{SO}_4$ ,  $\text{H}_2\text{O}_2$  and  $\text{H}_2\text{O}$ :



Caro's acid was kept at a temperature of 120 °C. The wafers were immersed for 5 minutes.

Then they were taken out of the bath and rinsed in DI water until the resistance of the water exceeded 15 M $\Omega$ .

##### 2. HF-Dip

After the treatment with Caro's acid, the wafers were dipped for 1 min in diluted hydrofluoric acid (0.5% HF).

This HF-dip removes the native silicon oxide and the chemical silicon oxide which was grown in step 1. By removing the thin surface oxide all contaminants which were incorporated in it were also removed.

The reactions follow the equations:



After the HF-dip wafers were rinsed again in DI water until the resistance of the water exceeded 17 M $\Omega$ . Finally the silicon wafers were dried in a spin dryer.

#### 4.4.2 Thermal Oxidation

In the fabrication process of integrated circuits, a field oxide is used to isolate a device from the neighbored devices. In this work, a field oxide is used to isolate the bottom contact from the silicon substrate and to suppress interdiffusion between Ir and Si. An interdiffusion could result in the formation of an iridium silicide. The silicide formation temperature of Ir has been found to be 400 °C [65].

Wet oxidation was used to grow this field oxide in a Centrotherm hot wall oxidation furnace. The oxidation reaction follows the equation:



Silicon oxide films of 200 nm thick were grown at atmospheric pressure for 10 min. A schematic view of the furnace is shown in figure 4-4.

The hot wall tube reactor has three heating zones which can be controlled independently. For oxidation, all three zones were kept at the same temperature.

The standby temperature of the oxidation tube was 400 °C; at this temperature the boats with wafers were loaded. After loading, the furnace temperature was linearly increased up to 1100 °C in two hours. The wet atmosphere, i.e. the water vapor, was produced by pyrolysis of hydrogen:

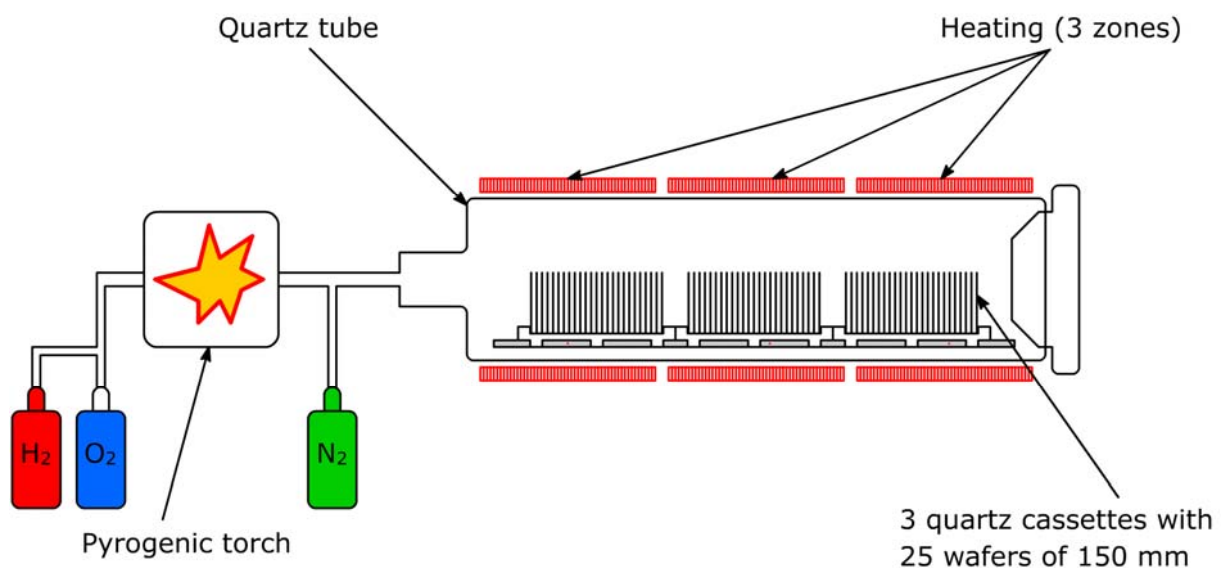


**Figure 4-4:** Schematic view of the hot wall tube reactor used for growth of the field oxide.

The oxygen flow was fixed slightly higher than half of the hydrogen flow to guarantee a total combustion and to avoid an accumulation of hydrogen in the scavenger box. The flows of oxygen and hydrogen were 3 slm and 5 slm, respectively.

#### 4.4.3 Deposition of the $TiO_2/Ir$ Stack Electrode

The deposition of iridium thin films on  $SiO_2/Si$  wafers was performed by using a Balzers electron beam evaporation system.

Figure 4-5 shows a schematic view of an e-beam evaporation system including e-beam, vacuum chamber, target and substrates, etc.

The substrates were mounted on a substrate holder designed to hold three 150 mm diameter substrates which was rotated at 12 rpm throughout the deposition to improve coating layer uniformity.

After the chamber was pumped down to the usual base pressure of  $4 \cdot 10^{-6}$  mbar with a cryopump (DE-208, Air Products, USA), a vapor flux of iridium atoms was generated with an electron beam evaporator (Baltzers, USA) and deposited on the substrates with a deposition rate of 1 nm/s.

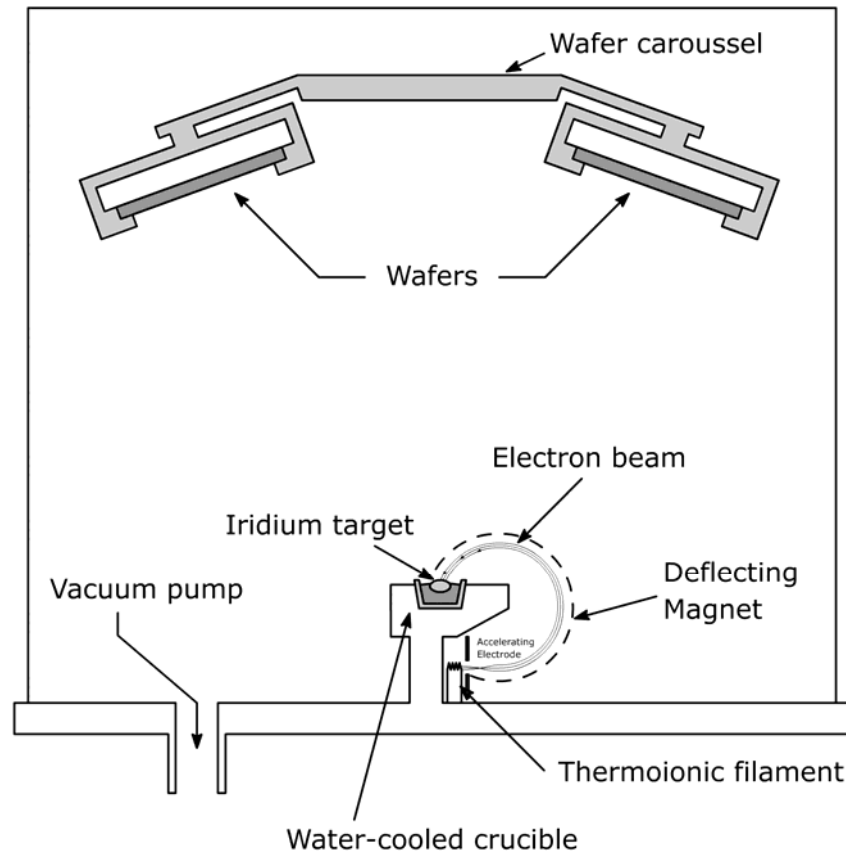


**Figure 4-5:** Schematic view of an e-beam evaporation system.

An *in-situ* quartz-crystal microbalance thickness monitor was used to measure the thickness of the deposited films. The quartz oscillates at a resonance frequency which is dependant on the thickness and the atomic mass of the film deposited onto it. If a voltage is applied across the surfaces of a properly shaped piezoelectric crystal, the crystal is distorted and changes shape in proportion to the applied voltage. At certain discrete frequencies of the applied voltage, a condition of very sharp and repeatable electro-mechanical resonance is seen. Quartz monitors are capable of measuring thickness of less than a single atomic layer with 0.5% accuracy.

Conditions for the deposition of the Ir thin films are listed in table 4-3.

**Table 4-3.** Ir thin film e-beam conditions.

Target	Ir (purity: 99.9%)
Substrate temperature	22 °C
Chamber pressure	$4.5 \cdot 10^{-6}$ mbar
Substrate	Ti/SiO <sub>2</sub> /Si
Film thickness	100 nm
Deposition rate	1 nm/s

A 10-nm-thick titan (Ti) buffer layer was deposited onto the SiO<sub>2</sub> film before deposition of the iridium film. This Ti buffer layer improves the crystallinity and the adhesion of the Ir bottom electrode, and also reduces the leakage current of the Ir/PZT/Ir structure [64,66].

#### **4.5 Fabrication of Test Devices (Capacitors)**

In order to investigate the electrical properties of PZT and SBT films test devices, i.e. capacitors, have been designed.

PZT and SBT films were grown on Ir coated substrate wafers. Then, a top Ir electrode of 100 nm thickness was e-beam evaporated through a shadow mask; alternatively sputtered Pt was used. The area of the circular dots was ranging from 0.03 to 0.785 mm<sup>2</sup>. After that, the wafer was divided into chips, which were annealed for 15 min in an oxidising atmosphere at temperatures ranging from 520 °C to 700 °C for PZT and from 700 °C to 1000 °C for SBT films. The final anneal is necessary to improve the crystal structure of the deposited films.

A cross sectional view of these test devices is shown schematically in figure 4-6.

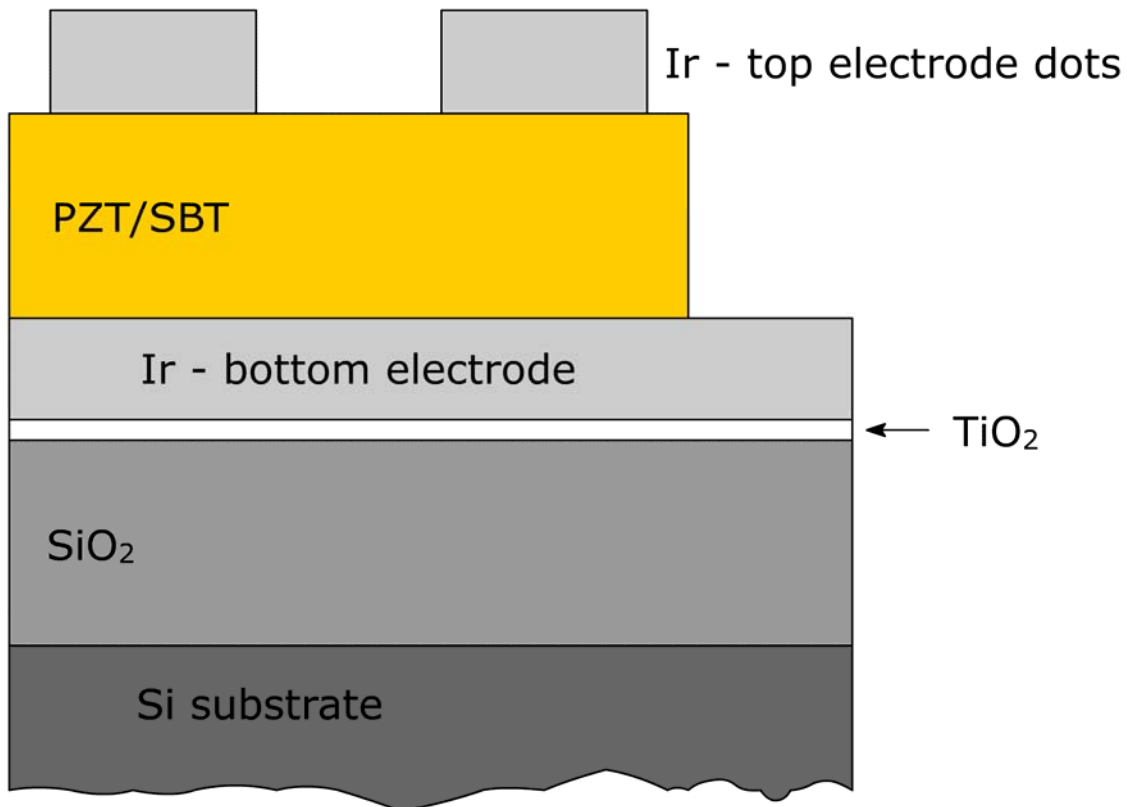


**Figure 4-6:** Used test structure of a ferroelectric capacitor.

#### 4.6 Characterization of Grown Films

The metrology procedures and tools which were used in this work in order to characterize the main material properties are briefly described below.

##### 4.6.1 Structural Properties

###### 4.6.1.1 Ellipsometry

The film thickness was measured using a spectroscopic ellipsometer (SE 850, Sentech, Germany). It is a high performance spectroscopic ellipsometer based on a fast diode array detection in the UV-VIS spectral range and interferometric modulated detection in the NIR spectral range, featuring both, fast data acquisition and full spectral resolution.

Figure 4-7 illustrates the basic principle of ellipsometry. The polarization state of the incoming light is known. This incident light interacts with the sample and is reflected at surface and interfaces. The interaction of the light with the sample causes a polarization change of the light from linear to elliptical polarization. The polarization change, or the change in the shape of the polarization, is then measured by analyzing the light reflected by the sample.

### 1. linearly polarized light...

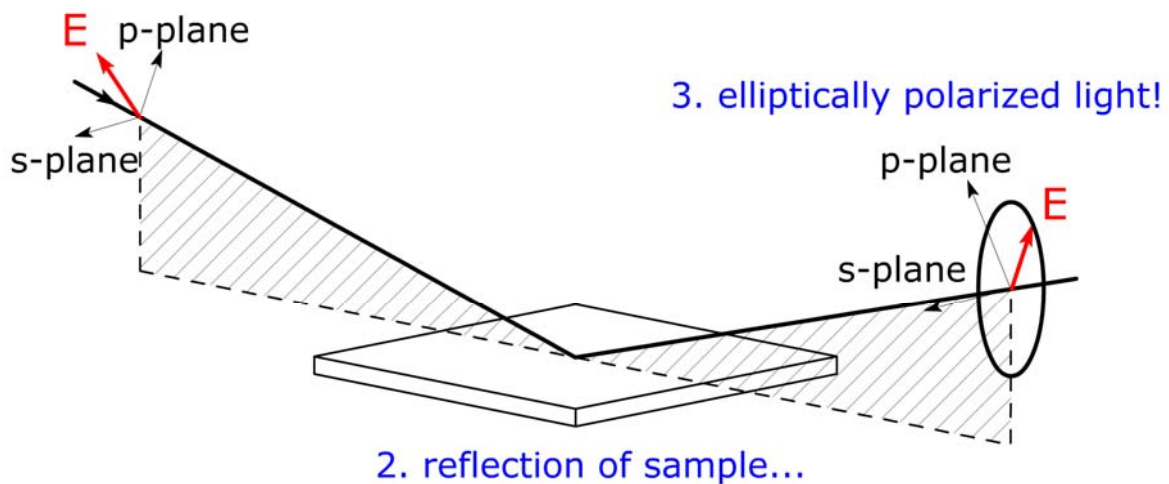


**Figure 4-7:** Geometry of an ellipsometric measurement.

Ellipsometry measures two values, Psi and Delta, which describe this polarization change. Because ellipsometry measures the ratio of two values, it can be highly accurate and very reproducible. The ratio is a complex number, thus it contains the “phase” information, delta, which makes the measurement very sensitive. Ellipsometric measurements were performed in the spectral range from 248 to 869 nm; a 75W xenon lamp and a halogen lamp were used as light sources. The uniformity of the film thickness was evaluated over the full wafer size using “Wafermap” mapping software of Boin GmbH.

#### 4.6.1.2 X-ray Photoelectron Spectroscopy (XPS)

The development and the implementation of advanced technologies require a thorough understanding of the effects of fabrication and processing on design and performance of a specific product. Measurements of the surface composition, elemental distributions, segregated impurity species, and interfacial chemical reactions are of fundamental importance in determining and understanding performance and possible failure mechanisms. X-ray photoelectron spectroscopy (XPS) has demonstrated its effectiveness in the solution of many of these technological problems.

XPS involves the energy analysis of photoemitted electrons from a sample with energies characteristic for the target elemental composition and its chemical state. Photoelectrons are emitted from the material (solid, liquid, or gas) as a result of absorption of a photon with the energy  $E = h\nu$ . The less tightly bound valence electrons and shallow core levels may be photoionized by UV photons (UPS), while deeper core-level electrons may be photoionized

by x-ray photons (XPS). Both types of photoelectrons are emitted with a discrete kinetic energy  $E_k$  given by:

$$E_k = h\nu - E_b - \phi_s \quad (6)$$

where  $h\nu$  is the energy of the incident photon,  $E_b$  is the binding energy of the photoelectron relative to the Fermi level, and  $\phi_s$  is the work function [67]. Figure 4-8 shows schematically electronic levels involved in the photoemission process. The Fermi level is used as the zero binding energy level by definition. Each photoelectron has a discrete energy characteristic for the element from which it was emitted, thus allowing to identify the present atomic species. Furthermore, the binding energy of an electron is influenced by its chemical surrounding resulting in a small energetic shift. This shift can be used to identify the chemical state of a given atom in the sample.

In addition to core-level ionization, x-ray induces the emission of Auger electrons due to relaxation processes after photoemission. Therefore, an XPS spectrum contains core-level emission and Auger emission spectral lines and provides information on both, the elemental composition and the chemical state of atoms in a given sample.

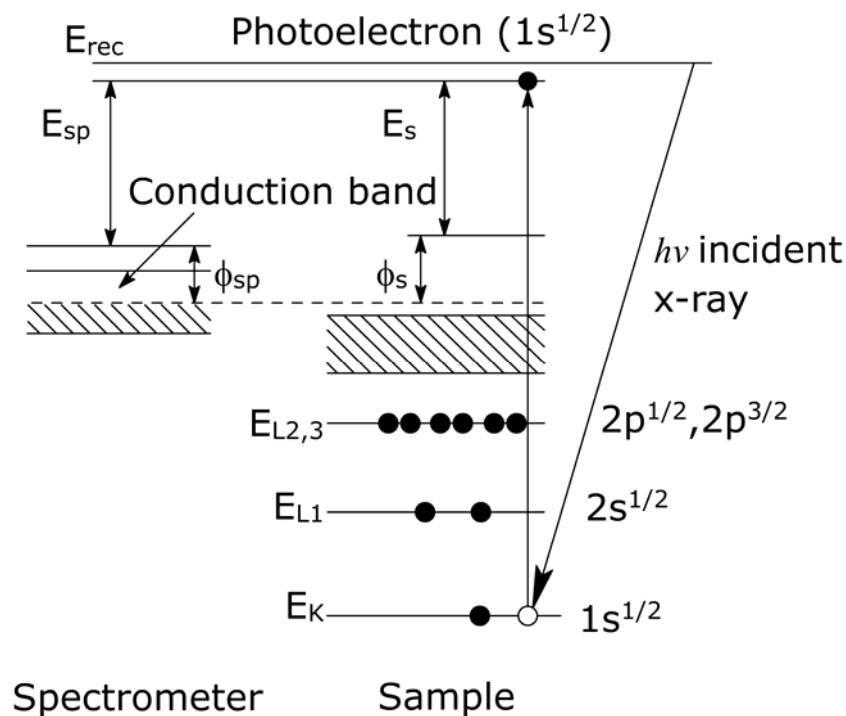


**Figure 4-8:** Schematic representation of the electronic levels involved in the photoemission process from a solid and the measurement of the electron energy by an analyser [68].

For quantifying XPS results two methods are in use. The peak heights method is analogous with the procedure used for AES in which the concentrations of each element present in the sample can be found from:

$$C_x = \frac{\frac{height_x}{sensitivity_x}}{\sum_{\substack{all \\ elements}} \frac{height_i}{sensitivity_i}} \quad (7)$$

where  $sensitivity_i$  is the relative sensitivity of Auger for each element which is available in graphs and tables.

The method based on the measurement of the peak area is the most accurate since this area exactly represents the photoelectrons emitted from a given transition. An accuracy of the quantitative compositional analysis of a materials is 0.5 at. %.

In our study XPS measurements have been carried out with a Perkin Elmer PHI 5600 ESCA system, using monochromatic Mg K $_{\alpha}$  (1253,6 eV) x-radiation with an input power of the excitation source of 400W. The emitted photoelectrons were collected over an area of 800  $\mu\text{m}$  in diameter and detected by an electron energy analyzer of SCA type. References for peak positions were taken from Moulder *et al.* [69] and compared with the results which were obtained elsewhere [70-72]. The analyzer's axis is located at an angle of 45° relative to the normal of the sample surface. Wide scans in the binding energy scale from 0 to 1100 eV at 50 eV analyzer pass energy were collected from the sample surface before and after sputter cleaning. The XPS depth-profiling was made by an ion bombardment with 4.5 keV Ar $^{+}$  ions. The peaks were referenced to the C (1s) peak at 284.6 eV for electrostatic charge correction.

#### 4.6.1.3 Microstructure

The microstructure of lead zirconate titanate films was characterized by atomic force microscopy (AFM). The atomic force microscope (Nanotop-206) was operated in contact and tapping modes. The average roughness ( $R_a$ ), the root-mean-square average roughness ( $R_q$ ), and skewness ( $R_{sk}$ ) of a surface were calculated from the integral of the roughness profile as follows:

$$R_a = \frac{1}{L} \int_0^L |r(x)| dx, \quad R_q = \sqrt{\frac{1}{L} \int_0^L r^2(x) dx}, \quad (8)$$

$$R_{sk} = \frac{1}{LR_q^3} \int_0^L r^3(x) dx. \quad (9)$$

$R_{sk}$  is a simple measure of the asymmetry of the amplitude distribution function, or, equivalent, it measures the symmetry of the variation of a profile along its mean line.

Cross-sectional scanning electron microscopy (SEM) was used for the investigation of the surface of the deposited films. Surface morphologies and film compositions were also analysed by scanning electron microscopy (Jeol JSM 5900) with EDX microanalysis.

#### 4.6.1.4 X-ray Diffraction (XRD)

Physical properties of the solids are in some way dependent from their crystal phase composition; therefore, an important goal of the materials science is the evaluation of the lattice structures.

X-ray diffraction is one of the most important characterization tools used in solid state chemistry and material science for studying the atomic and molecular structure of crystalline substances such as ceramics, stones, sediments, etc. The sample, a single crystal, a film or powder, is exposed to X-rays at various angles (figure 4-9).

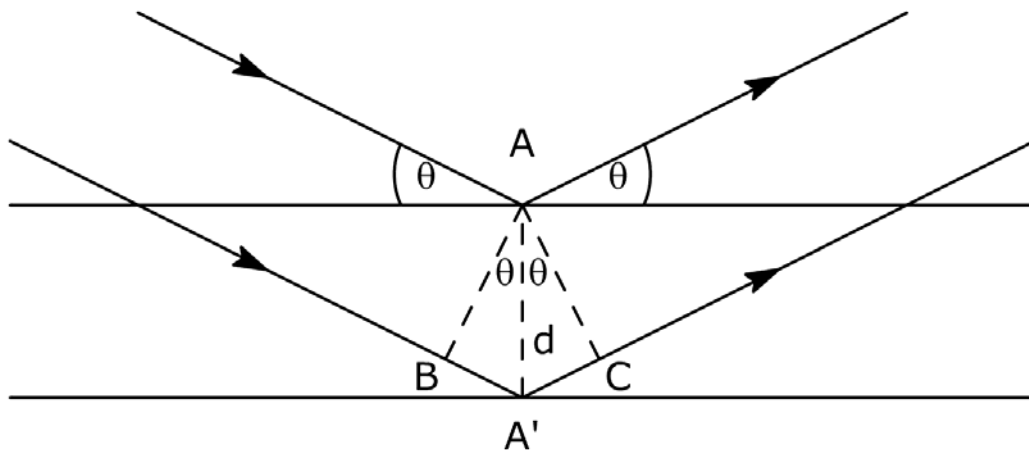


**Figure 4-9:** Parallel rays reflected from points on neighbored partially reflecting planes are in phase when Bragg's law is obeyed.

The condition for constructive interference of the reflected x-rays is given by:

$$BA' + A'C = n\lambda \quad (10)$$

where  $n$  is an integer.

From figure 4-9 it can be seen that:

$$BA' = A'C = d \cdot \sin\theta \quad (11)$$

giving:

$$2d \cdot \sin\theta = n\lambda \quad (12)$$

This expression is known as Bragg's law and it gives the permitted angles of reflection  $\theta$  in terms of wavelength  $\lambda$  and the spacing of the reflecting planes  $d$  [73].

Reflected rays are detected by a diffractometer; the obtained diffraction patterns are then compared with reference standards for identification. Each solid has its unique characteristic X-ray powder pattern which may be used as a "fingerprint" for its identification. Once the material has been identified, X-ray diffraction may be used to determine its crystalline or microcrystalline structure, i.e. the relative orientation of atoms in the crystal or crystallite, interatomic distances, angles etc. Furthermore, it is possible to determine the size and the shape of the unit cell for any compound easily using this method.

The crystal structure of as-deposited films and the phase change of these films after annealing were investigated by X-ray diffraction (XRD). The XRD spectra were recorded using the X-ray diffractometer DRON-3.0. X-ray tube 2.0 BSV- 24Cu with Cu anode was used as X-ray source. Ni filter was used to minimize  $\text{CuK}\beta$  radiation. The anode radiation wavelength was  $\lambda = 0.154178$  nm. The phase composition of the samples was revealed using a Fullprof software by comparing experimentally measured interplanar distances  $d$  and angles of the crystallographic plane reflections in the X-ray diffractogram with data of the JCPDS database.

#### 4.6.2 Electrical Properties

The electrical properties of ferroelectric films were characterized by measuring the polarization vs. electric field (P-E) hysteresis loops, the dielectric constant, the leakage current and the polarization fatigue. To study the leakage behaviour of the films, DC current-voltage (I-V) measurements were carried out. The dependence of the dielectric constant on the applied voltage was calculated from capacitance (C-V) measurements.

For the determination of the electrical parameters of PZT and SBT films several measurement systems were used outlined below in detail. These systems include a chuck connected with a thermal bath (Haake DC10, Thermo) which allows to adjust the chuck temperature from 20 °C to 120 °C, and, consequently, enables the measurements of the

electrical properties at different, well defined temperatures. Moreover, the chuck is connected to a vacuum pump which fixes the sample to the chuck.

Before electrical measurements were carried out, PZT and SBT films were etched partly at one corner of the chips in order to provide an electrical contact to the bottom electrode. The contact needles could be positioned precisely on the contact electrodes of the device under test by using a micromanipulator with a coaxial shielded needle.

Chuck, device under test and micromanipulator are mounted in a metallic box in order to shield the sample from external electro-magnetic radiation sources which may distort the measurements.

Further components of the measurement system are a Sub-Femtoampere Remote Source Meter (Keithley 6430, USA) and a Precision LCR Meter (Agilent 4284A, USA). A schematic view of the measurement set-up is given in figure 4-10.

The Model 6430 Sub-Femtoamp Remote Source Meter combines voltage/current source and measurement functions and exhibits sensitivity, noise, and input resistance specifications superior to electrometers. The wide 20 Hz to 1 MHz test frequency range and the test-signal performance of the Agilent 4284A allow to test the components of the most commonly used test standards.

All used measurement equipment was programmable and was connected to a PC using an IEEE interface bus system (IEEE-488). This allows the control of the instruments by a remote PC and automatic measurement procedures. Control of the measurement equipment, reading and evaluation of the data were realized by using the graphical programming environment Agilent VEE.

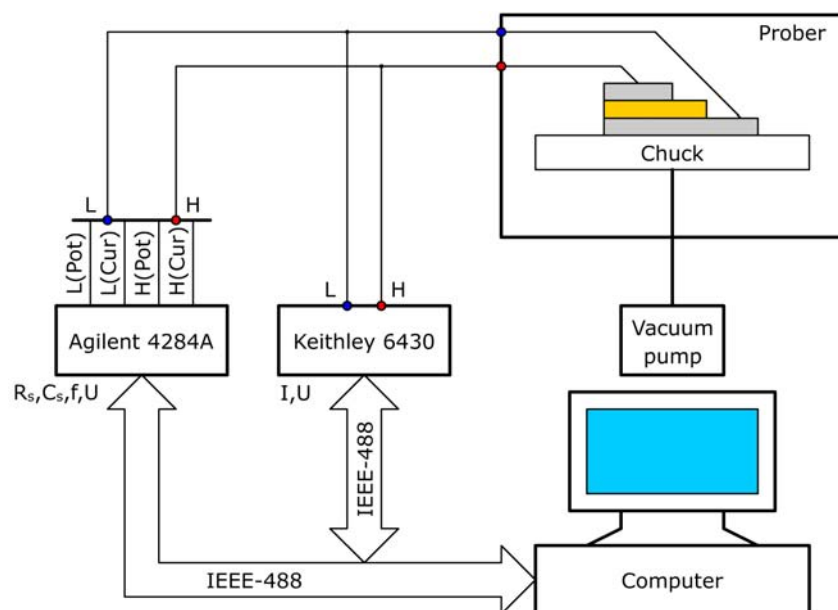


**Figure 4-10:** Schematic view of the used measurements system.

The commonly accepted criterion of ferroelectricity is the hysteresis loop on a D-E display. This method was introduced by Sawyer and Tower in 1930. Up to now this method remains the most applied method for investigating ferroelectric properties.

An alternative voltage is applied to the test device and the related stored charge is determined. In order to measure this charge a large integrating capacitor is connected in series to the test devices. The voltage decay across this capacitor  $C_0$  is a measure for their charge. This voltage decay is displayed on the vertical axis of an oscillograph. The applied external voltage is connected to the horizontal x-deflection. Figure 4-11 shows schematically this set-up. The experiment is usually run at rather low frequencies of about 60 cycles/sec or less.

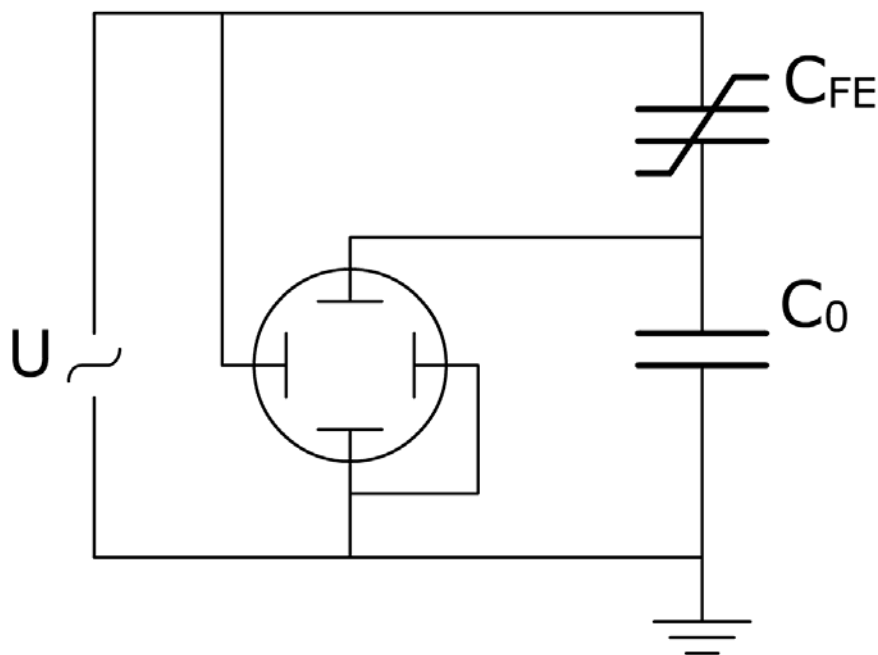


**Figure 4-11:** Circuit for display of dielectric hysteresis (after Sawyer and Tower) [74].

This method has few drawbacks as, for example, a parasitic capacitance. Additionally, it neglects the phase shift of the measured voltage (y-axis) which is due to the finite conductivity of the ferroelectric material and the flow of leakage currents. Therefore, this measurement set-up was not used for the investigations of the ferroelectric properties of the deposited films. The measurements of the P-E hysteresis loop and of the polarization fatigue were realized by using a commercially available characterisation system, the TF Analyzer 1000 (aixACCT Systems GmbH, Aachen, Germany), see figure 4-12.

The TF Analyzer 1000 includes a built-in function generator, an analog input board, and a wide bandwidth virtual ground amplifier with driving unit. This system offers hysteresis measurements from 1 Hz to 250 Hz bandwidth depending on the excitation voltage in virtual

ground mode. The arbitrary waveform generator applies the selected pulse sequence to the device under test. A Windows based graphical user interface ensures easy access to all operations.

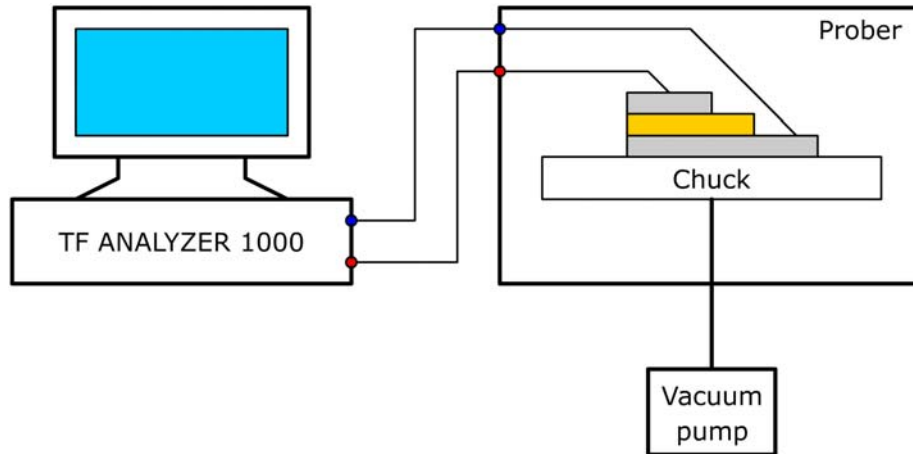


**Figure 4-12:** Schematic view of the system used for the hysteresis measurements.

The measured results can be graphically presented on the screen or saved in two different formats. Data files of the TF Analyzer 1000 system program use a specific file format which allows quick access to the data. The second format is used to export measurement data as an user readable ASCII-file. ASCII data files can be imported into any data presentation program. Ahead of each data section text lines are included which describe the type of data, sample data and measurement conditions.

The dynamic hysteresis measurements were performed at room temperature and an operating voltage in the range from  $-3$  to  $+3$  V. The prepolarization pulse establishes a defined polarization state, the negative state of relaxed remanent polarization. The prepolarization pulse is followed by three consecutive bipolar excitations signals, each signal separated by one second relaxation time. The voltage excitation signal is shown in figure 4-13 in the case of a triangular voltage excitation.

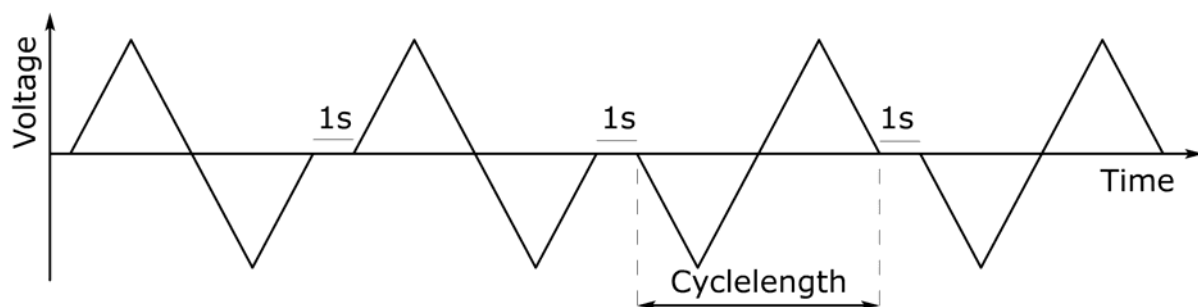


**Figure 4-13:** Excitation signal for hysteresis measurement.

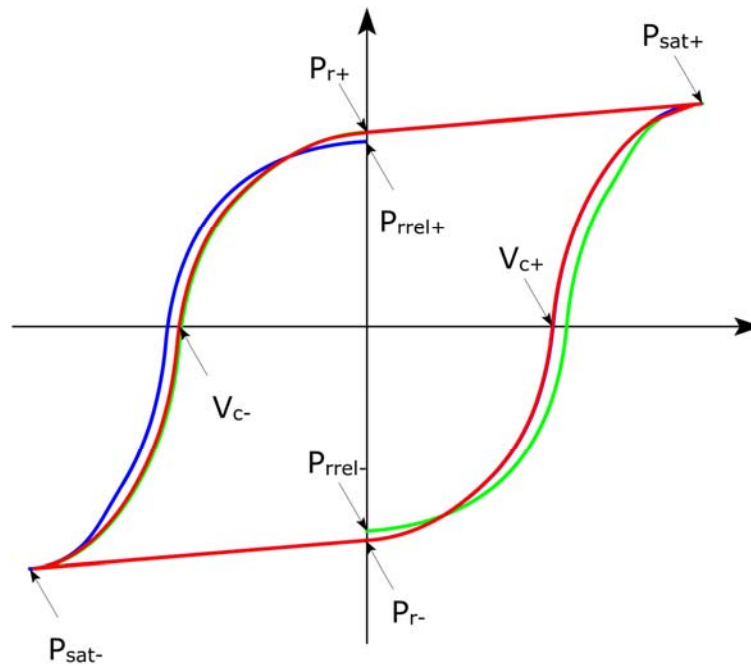


**Figure 4-14:** Nomenclature used within the TF Analyzer 1000 system.

The hysteresis loop corresponding to pulse no. 1 starts in the negative relaxed remanent polarization state ( $P_{rrel-}$ ) and turns into the positive saturation ( $P_{sat+}$ ) (figure 4-14). When the voltage is equal to zero the polarization reaches the positive remanent polarization state ( $P_{r+}$ ), afterwards it turns into the negative saturation ( $P_{sat-}$ ) and back to the remanent polarization state ( $P_{r-}$ ). This point is normally not equal to the starting point ( $P_{rrel-}$ ), because of the polarization loss over time.

The second loop pushes the sample into the positive remanent state without sampling data. The third loop starts in the positive relaxed remanent polarization state ( $P_{rrel+}$ ), and turns to the negative saturation ( $P_{r-}$ ).

Afterwards the sample is driven into the positive saturation ( $P_{sat+}$ ) and ends in the positive remanent polarization state ( $P_{r+}$ ) when the voltage is zero. Afterwards the hysteresis loop is balanced respectively to the values ( $P_{sat+}$ ) and ( $P_{sat-}$ ). From the data of the first loop the parameters  $V_{c-}$ ,  $P_{r-}$ ,  $P_{rrel-}$  are determined and from the data of the third loop the parameters  $V_{c+}$ ,  $P_{r+}$ ,  $P_{rrel+}$ . The closed hysteresis loop (red curve) is calculated from the second half of the first (green curve) and the second half of the third loop (blue curve).

The fatigue tests were performed under accelerated conditions using an externally generated triangle pulse with an amplitude of  $\pm 5$  V and a frequency of 100 Hz. After measuring an initial hysteresis the fatigue signal sequence (see figure 4-15) is applied to the sample.

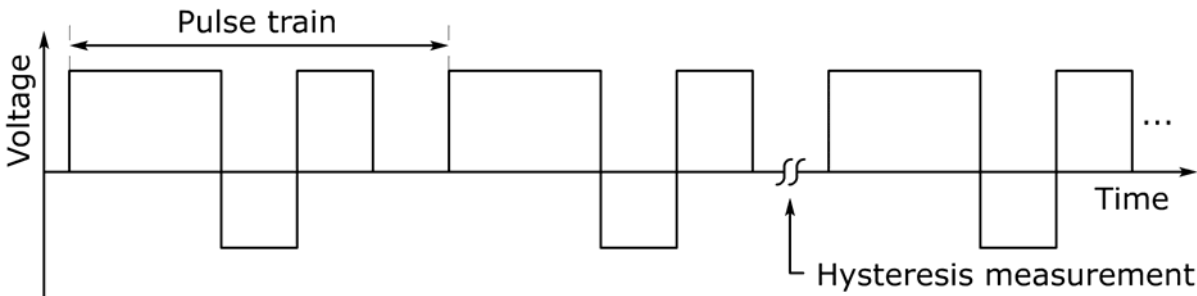


**Figure 4-15:** Typical excitation signal.

The fatigue treatment is interrupted regularly for hysteresis measurements. These intermediate hysteresis measurements are performed with time intervals in such a way that data points are depicted with an equal spacing in a logarithmic plot.

## ***Chapter 5 Results and Discussion***

The structural and electrical properties of LD-MOCVD grown  $\text{Pb}(\text{Zr},\text{Ti})\text{O}_3$  (PZT) and  $\text{SrBi}_2\text{Ta}_2\text{O}_9$  (SBT) thin films deposited on an Ir electrode, i.e. on Ir/ $\text{TiO}_2$ / $\text{SiO}_2$ /Si wafers have been investigated. The results of these investigations are presented and discussed in this chapter. The first part of this chapter deals with lead zirconate titanate films, the second with strontium bismuth tantalate films. Growth kinetics of the single oxide as well as of the three-metal oxide films are described in the first sections of this chapter. The second section is dedicated to the morphology of the deposited films. The influence of the deposition parameters, such as deposition pressure, substrate temperature, and injections parameters, on the film structure is considered. The last section of this chapter presents the results of the electrical measurements. The influence of the process parameters on the ferroelectric properties of the PZT and SBT films is discussed. In addition, the influence of the post-deposition annealing on the structural and electrical properties of the thin ferroelectric films is also lined out.

### ***5.1 Lead Zirconate Titanate***

#### ***5.1.1 Growth Kinetics***

In order to get more insight into the deposition behavior of the metalorganic sources which were chosen for the fabrication of lead zirconate titanate films, the growth of each single metal oxide was investigated in dependence on temperature.

Figure 5-1 shows the relationship between the deposition temperature and the deposition rate of each single metal oxide. The pressure in the reactor was adjusted to be 1.5 mbar. During the deposition of the metal oxides, each metalorganic source was supplied intermittently with an inlet frequency of 2 Hz for lead and zirconium oxides and 50 Hz for lead and titanium oxides.

The growth rate of each single oxide film strongly depends on the deposition temperature. In the case of tetraethyllead (0.1 mol/l), the deposition rate of the lead oxide increases from 0.1 nm/min at a deposition temperature of 350 °C up to 10 nm/min at 550 °C (figure 5-1a).

The increase of the deposition rate at higher temperatures is also observed for the titanium isopropoxide precursor (0.1 mol/l). The value of the growth rate of the titanium oxide changes from 20 to 80 nm/min whereby the substrate temperature has been increased from 400 to 500 °C (figure 5-1b).

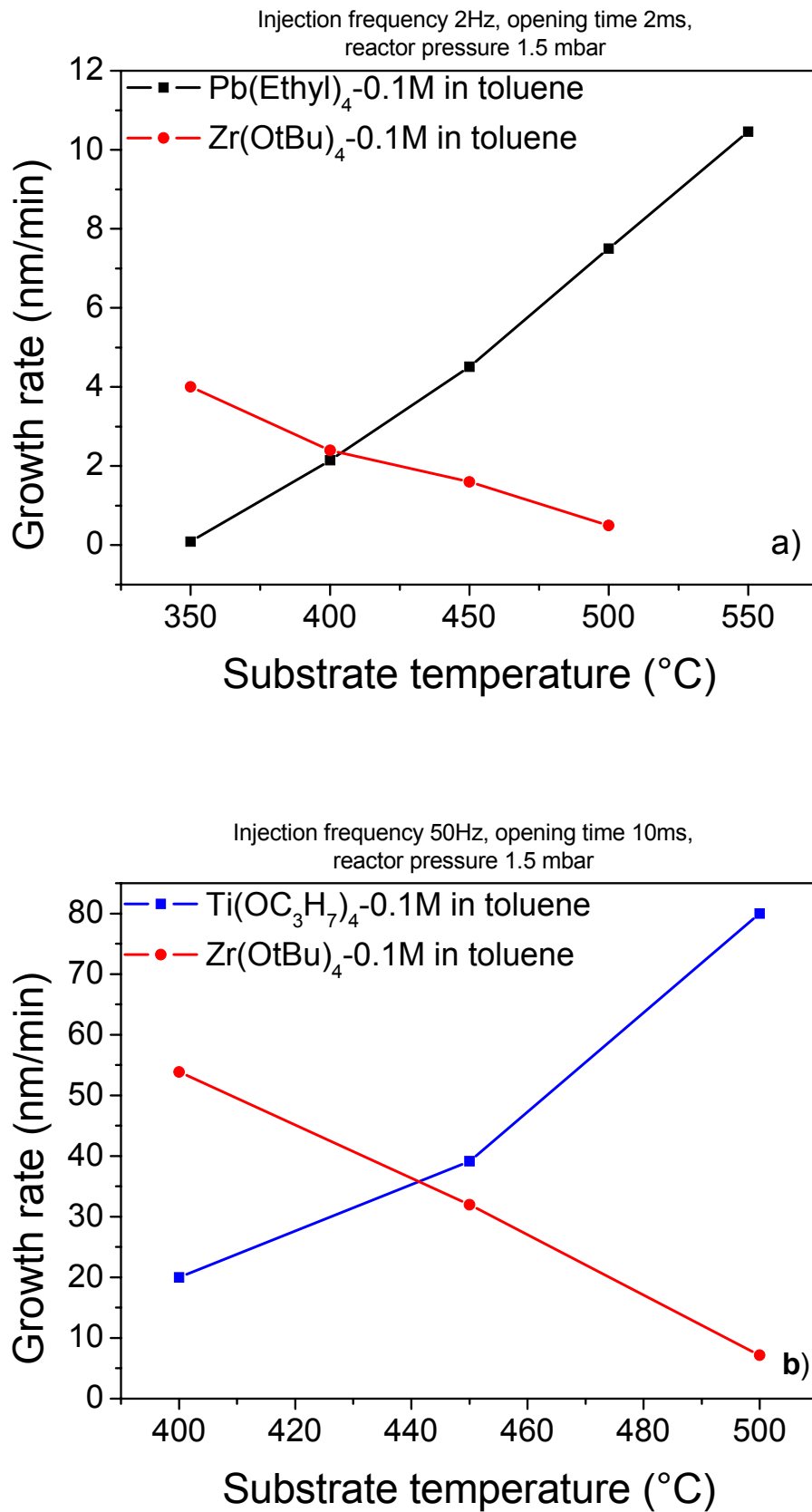


**Figure 5-1:** Temperature dependence of the deposition rate of the single metal-oxide films for two parameter sets of the Trijet injection system.

Such dependence of the film growth rate on the deposition temperatures can be explained by the growth rate of PbO and TiO<sub>2</sub> thin films being limited by the substrate temperature. This behavior is characteristic of a deposition process known as kinetically controlled deposition in which the surface decomposition of the precursor is the rate determining step [75,76]. A further increase growth rates of the oxides at higher temperatures and decomposition reaction controlled depositions have also been observed by Funakubo *et al.* [77,78] for lead oxide and by Krumdieck [79] and Kang [80] for titanium oxide.

On the contrary, for the zirconium tetrabutoxide precursor (0.05 mol/l) the growth rate of the zirconium oxide decreased from 4 to 0.5 nm/min (figure 5-1a) and from 54 to 7 nm/min (figure 5-1b) whereby the substrate temperature has been increased from 350 to 500 °C. A growth rate reduction at higher temperatures has also been reported by M. Cassir *et al.* [81] and M.A.Cameron *et al.* [82]. M.A. Cameron has supposed that the zirconium tetrabutoxide surface reaction may be partially poisoned by carbon at temperatures higher than 500 °C. After pyrolytic decomposition of the zirconium tetrabutoxide precursor on the ZrO<sub>2</sub> surface deposited carbon is unable to desorb at these growth temperatures and the carbon poisons the ZrO<sub>2</sub> growth. The lower ZrO<sub>2</sub> growth rates at higher temperatures may also be explained by a precursor-mediated adsorption mechanism [83,84]. In precursor-mediated adsorption, the zirconium tetrabutoxide reactant molecule reaches the ZrO<sub>2</sub> surface and is physisorbed. From this physisorbed state, the Zr(OtBu)<sub>4</sub> precursor can either desorb or react with the ZrO<sub>2</sub> surface to become adsorbed in a chemisorbed state. At low temperatures the surface species may preferentially react with the surface. At high temperatures desorption of the zirconium tetrabutoxide precursor may be the predominant mechanism, and the precursor desorption may significantly reduce the ZrO<sub>2</sub> growth rate. M. Putkonen writes in his dissertation that the decrease in the growth rate of ZrO<sub>2</sub> at higher temperatures is typical only for pulsed deposition and, probably, can be due to the completely decomposition of reactants before reaching the substrate [85].

The decrease of the zirconium oxide deposition rate due to carbon poisoning is unlikely in our case because of the use of lower deposition temperatures and the absence of the carbon contamination in the deposited films. The absence of the carbon in deposited zirconium oxide films is easy to explain due to the additional introduction of oxygen in the reactor. Carbon, which appears after zirconium tetrabutoxide decomposition, reacts with oxygen and desorbs from the substrate surface. According to the theory offered by Putkonen zirconium oxide films should not grow on the substrate but on the reactor walls; this effect has also not been

observed in our case. Therefore, the decrease of the zirconium oxide growth rate with increased temperatures can be explained by the desorption of reactants.

After deposition of the single oxides, a temperature of 450 °C appears to be the optimum temperature for the deposition of PZT thin films. At higher temperatures the deposition rate of  $ZrO_2$  is rather low, while at lower temperatures the deposition rates of  $TiO_2$  and  $PbO$  are not high enough.

The homogeneity of the deposited films plays an important role in the production of semiconductor devices. Therefore, the influence of the deposition pressure on the film homogeneity has also been investigated. Figure 5-2 shows the film thickness distribution across the wafer for PZT films grown at deposition pressures of 0.5 and 1.5 mbar.

As can be seen in the figure, an increase of the deposition pressure results in an increase of the deposition rate. But on the other hand, the uniformity of the film thickness over the wafer surface decreases and the value of the standard deviation significantly increases at higher deposition pressures.

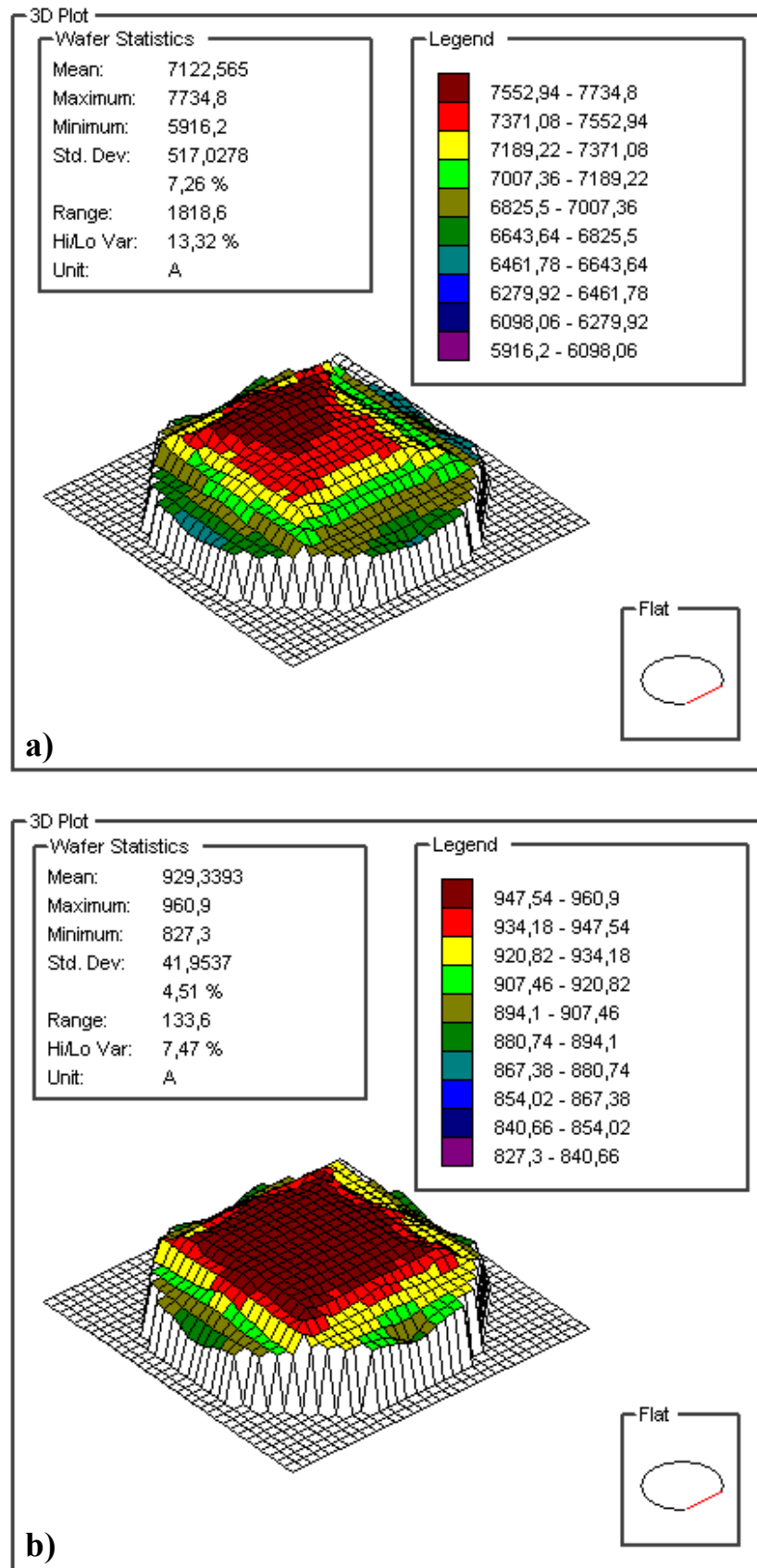


**Figure 5-2:** Film thickness map of PZT films deposited at different pressures:  
a) 1.5 mbar and b) 0.5 mbar.

Film thickness measurements reveal that a pressure of 0.5 mbar appears to be close to the optimum value as a high thickness homogeneity across the wafer is combined with a sufficiently high deposition rate.

Film thickness measurements have been difficult to be performed on the films which are covered with lead oxide crystals. These films are not transparent and, thus, not usable for optical measurements. A slight decrease of the injection rate of the lead precursor during deposition, however, results in transparent and smooth surfaces. At a deposition temperature of 450 °C the growth rate is 5-6 nm/min; a PZT film of 100 nm can be grown in about 20 min.

An increase of the substrate temperature up to 550 °C results in higher deposition rates of the PZT film but also in a higher film thickness inhomogeneity. The value of the standard deviation of the film thickness increases from 4-5 % at 450 °C to more than 10 % at 550 °C, compare figures 5-2b and 5-3.

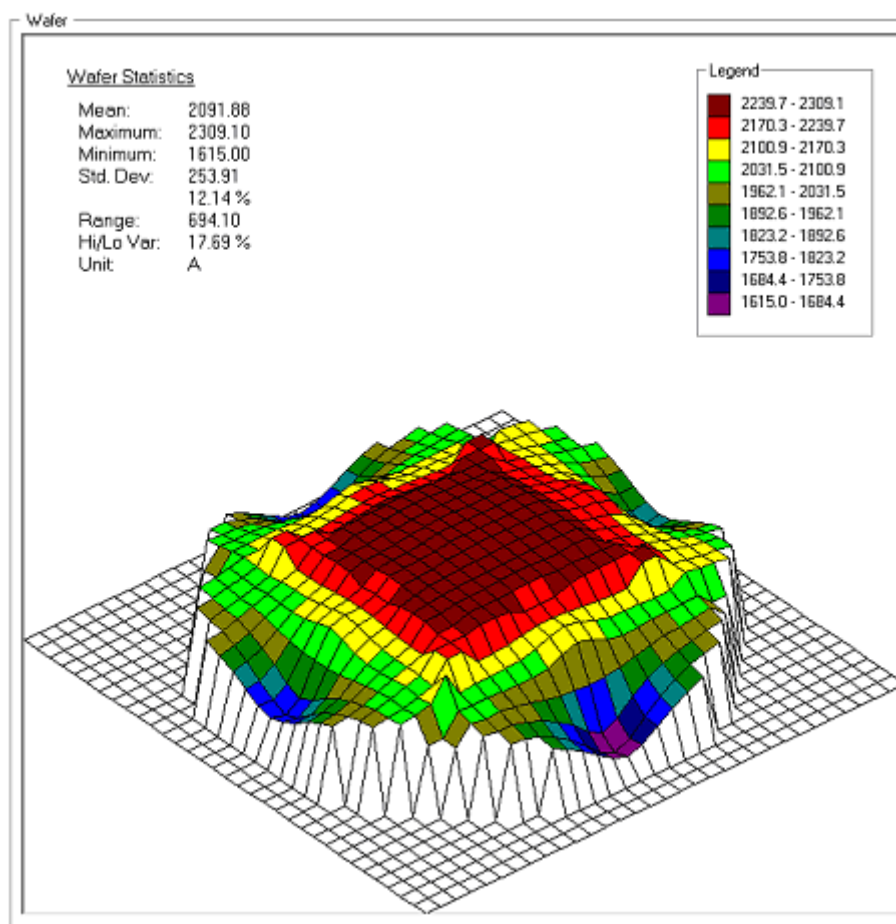


**Figure 5-3:** Dependence of the film thickness on the position at the wafer for a PZT film grown at 550 °C and a pressure of 0.5 mbar.

### 5.1.2 Films Structure

The compositional analysis of PZT films was performed using X-ray photoelectron spectroscopy (XPS). The morphology of the films was characterised using scanning electron microscopy (SEM). The crystal structure of the thin films and their crystallographic orientation were examined by X-ray diffraction (XRD) using Cu-K $\alpha$  radiation. The formation kinetics of PZT films was investigated by an optical method and by atomic force microscopy (AFM).

#### 5.1.2.1 X-ray Photoelectron Spectroscopy Investigation of the Deposited Films

Figure 5-4 shows two XPS spectra taken from an as-deposited surface and from a 60 sec Ar<sup>+</sup>-ion bombarded surface of a thin PZT film deposited on a Si substrate. The spectrum exhibits dominant peaks of Pb, Zr, Ti, O together with a C (1s) peak which is due to the surface contamination with carbon.

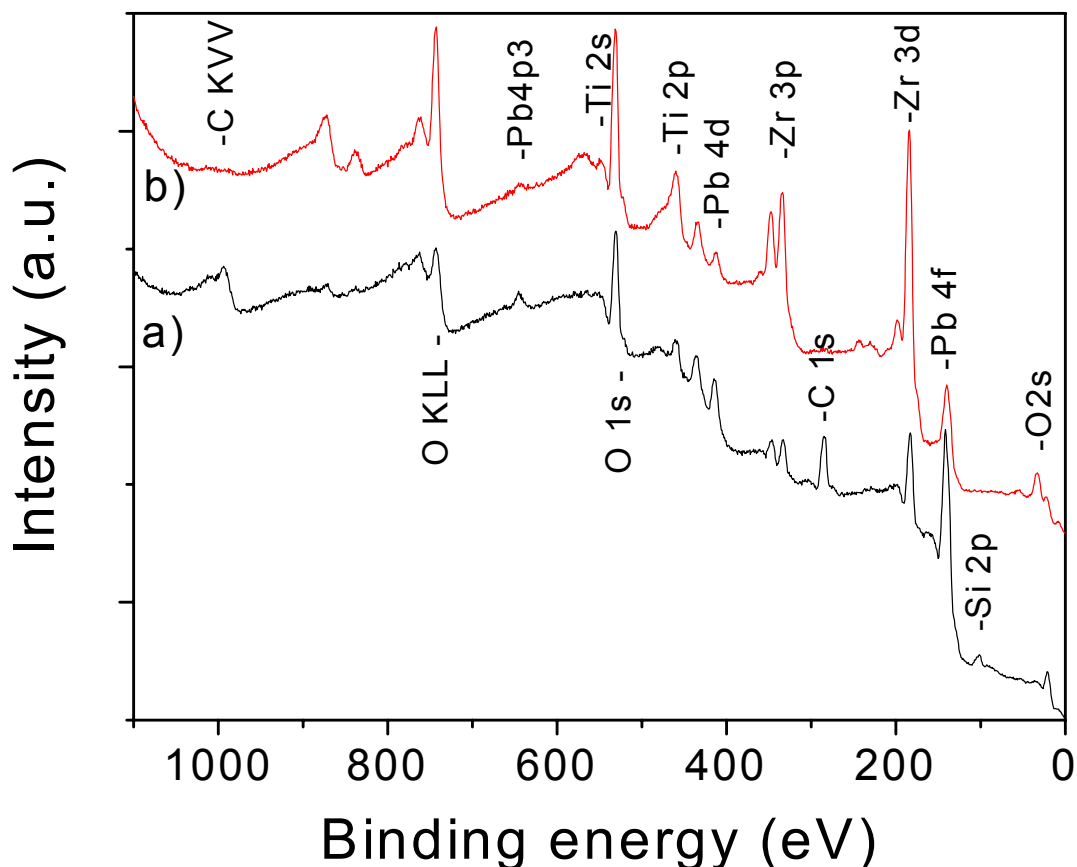


**Figure 5-4:** XPS spectra of a PZT thin film taken from a) the as-deposited surface and b) the surface after Ar<sup>+</sup>-ion sputtering (60 s).

XPS measurements of an as-deposited film indicate that the surface layer of this film contains 40.6 at% carbon, 34 at% oxygen, 5.4 at% lead, 8 at% zirconium and 4.2 at% titanium.

After cleaning the wafer surface from adsorbed contaminations by  $\text{Ar}^+$  sputtering for 60 seconds the measurement has been repeated again. The results of these measurements are shown in figure 5-4b. The elemental composition of the PZT thin film after surface cleaning are as follows: C – 2.5 at%, Pb – 2.4 at%, Zr – 24.9 at%, Ti – 8.8 at%, and O – 61 at%.

Carbon species are only present on the film surface as surface contamination. Substrate temperature and oxygen flow during the film growth have been high enough for fabricating carbon-free films. The surface adsorbed oxygen is reduced after 60 sec  $\text{Ar}^+$ -ion bombardment, but does not disappear entirely. The increase of the oxygen concentration as well as the increase of zirconium and titanium concentration is related to the lack of carbon in comparison to the surface.

The peaks of both spectra have been fitted using a Gauss function in order to get a better insight into the chemical bounding states. For the surface of the as-deposited film, the C (1s) peak (figure 5-5a) can be attributed to hydrocarbon species (C-H) at 284.6 eV and small amount of carboxylate (COO) species at 287.9 eV [72].

The spectrum of figure 5-4 indicates that no contamination, except for hydrocarbon and carboxylate, occurs during the deposition and the analysis processes.

The O (1s) peak (figure 5-5b) can be decomposed into two components at binding energies of 529.4 and 532.9 eV. According to Qu et al. [87], these peaks are assigned to the lattice oxygen and surface adsorbed oxygen, respectively. However, a hydroxyl peak can not be detected.

In figure 5-6 it is shown that the Zr and Ti signals exhibit only one spin-orbit doublet, i.e. Zr (3d) = 183.6 eV, Ti ( $2p_{3/2}$ ) = 457.8 and Ti ( $2P_{1/2}$ ) = 463.5 eV; this observation indicates that Zr and Ti in the deposited film are in the PZT chemical binding state.

The shoulders of the experimentally found peaks in figure 5-7 a) and b) are due to two peaks which lie close together in energy. The fits clearly reveal these two peaks. They represent two spin-orbit doublets of Pb (4f).

The observed Pb (4f) doublet at 137.7 eV and 142.6 eV (a), corresponding to Pb ( $4f_{7/2}$ ) and Pb ( $4f_{5/2}$ ), respectively, represents lead species in PbO while the Pb (4f) doublet with peaks at 135.9 eV and 140.8 eV (b) correspond to the same core levels of lead species in PZT [87,88].

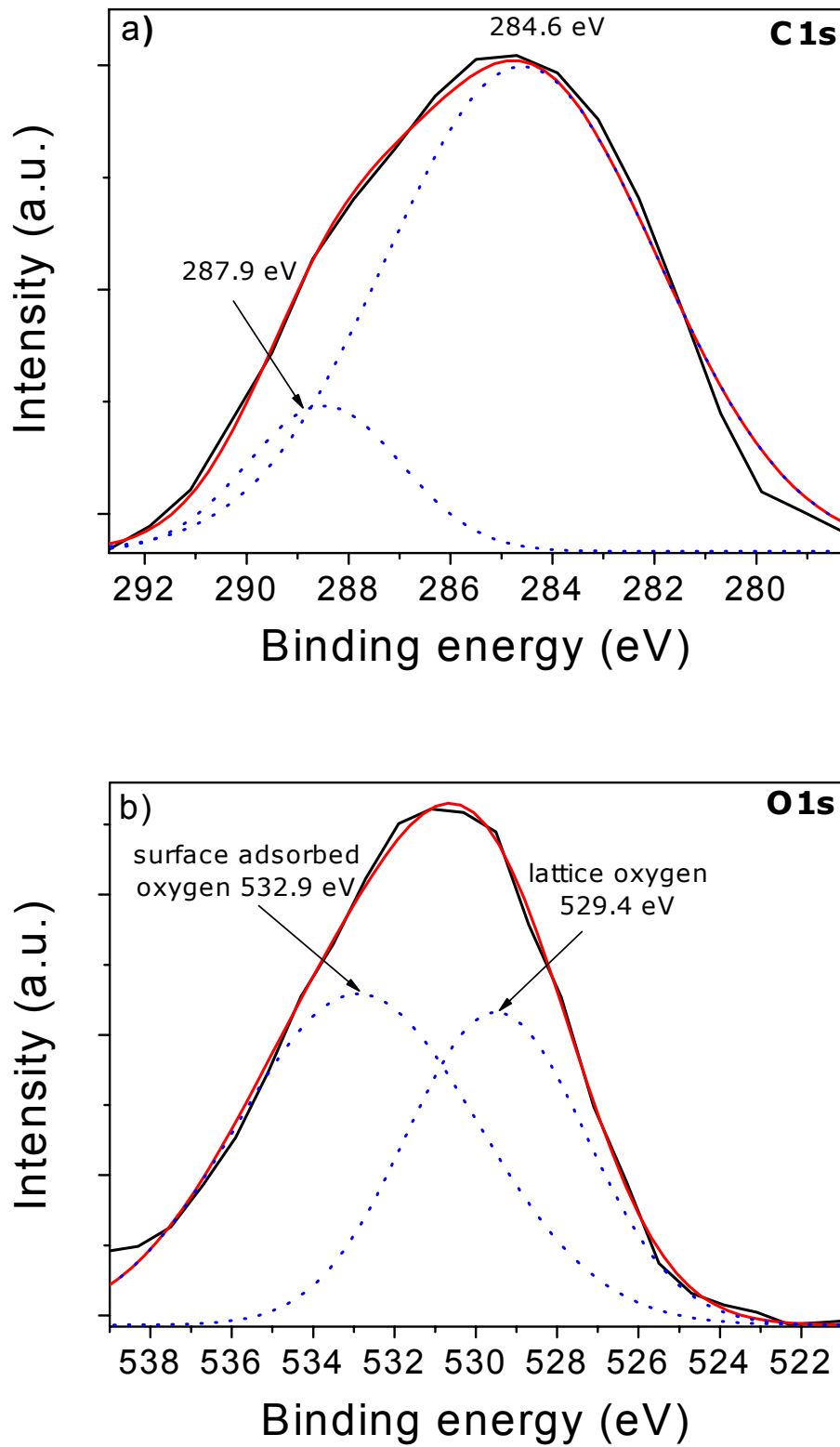


**Figure 5-5:** Fitted details of the XPS spectrum of a PZT thin film; a) C (1s) and b) O (1s).

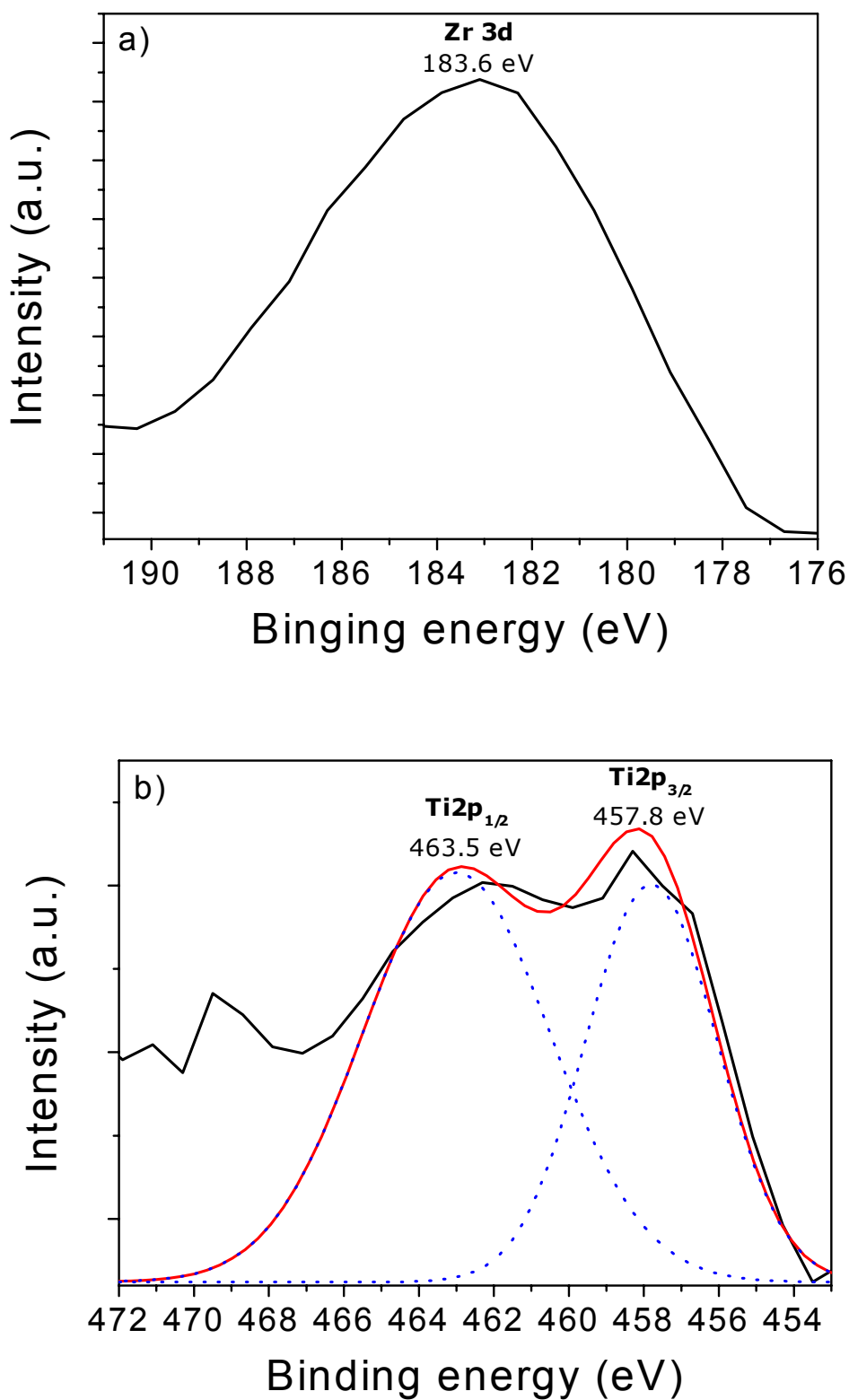


**Figure 5-6:** XPS spectra showing the Zr (3d) peak (a) and the Ti (2p) peaks (b). Included in (b) is a fit of the two Ti (2p) peaks.

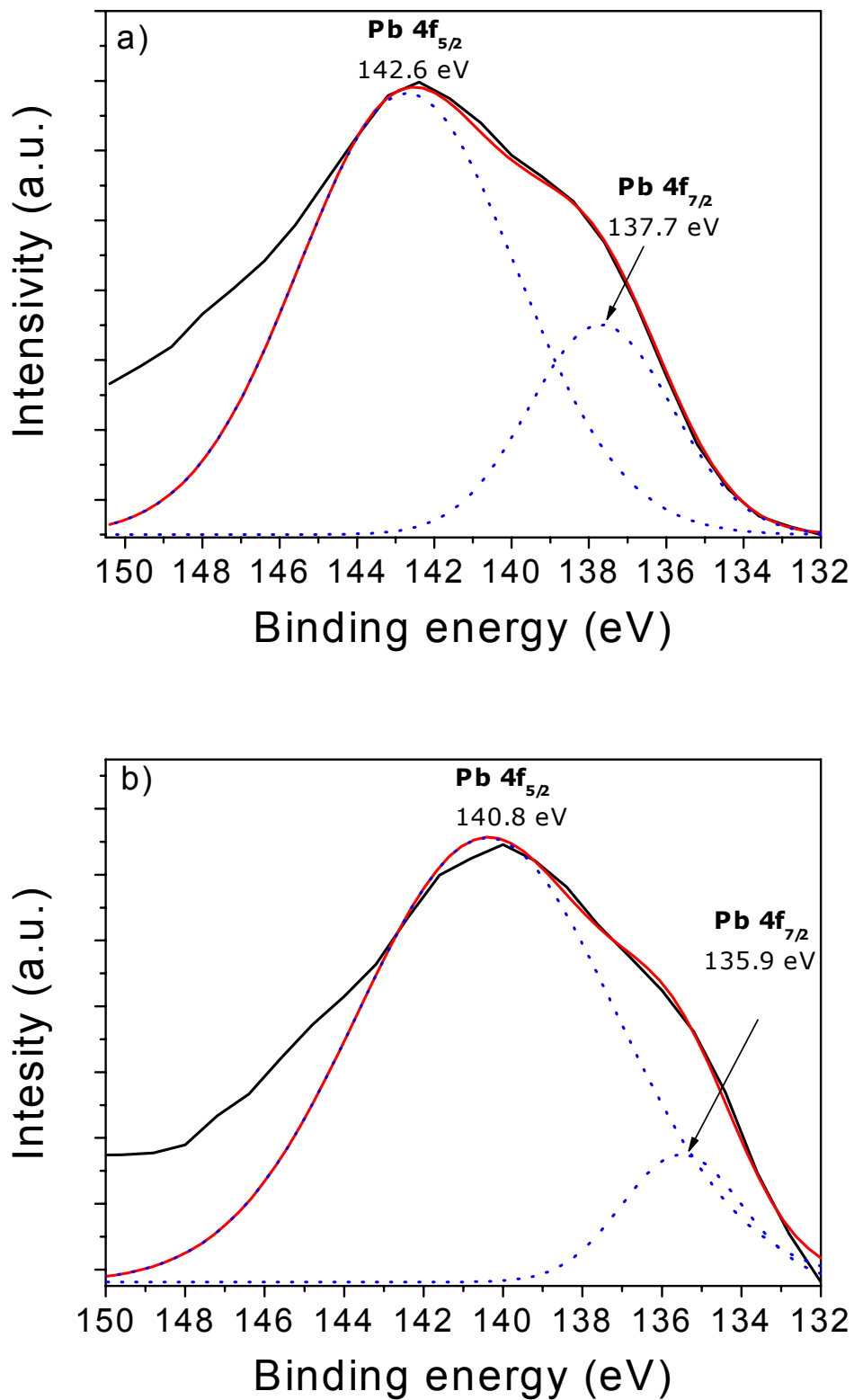


**Figure 5-7:** XPS spectra of the Pb (4f) peak of a PZT thin film; a) before and b) after sputtering. Included in the figure are also fits of these peaks.

The top region of the surface of a PZT film predominantly contains lead species as PbO. This is probably due to lead atoms segregating at the surface of the PZT film which are oxidized to form PbO. After sputtering the amount of lead species in PbO decreases and Pb species in PZT become dominant.

As lead is preferentially sputtered by  $\text{Ar}^+$  ions, a lead deficit is measured. Taking into account this effect a recalculation of the lead content results in a concentration of 15 at%, a too low concentration for a stoichiometric composition.

PZT film grown on iridium covered substrate under different conditions shows different optical and structural properties in comparison to those grown on silicon. XPS analysis shows that these films have a lead content of more than 70 at%, figure 5-8. PZT films with a huge excess of lead are very rough. The high roughness of the deposited films is related to the formation of lead oxide on the substrate surface. This lead oxide consists of leaf-shaped crystals, see figure 5-9. In this case, it is not possible to measure the film thickness by standard optical method as by ellipsometry.

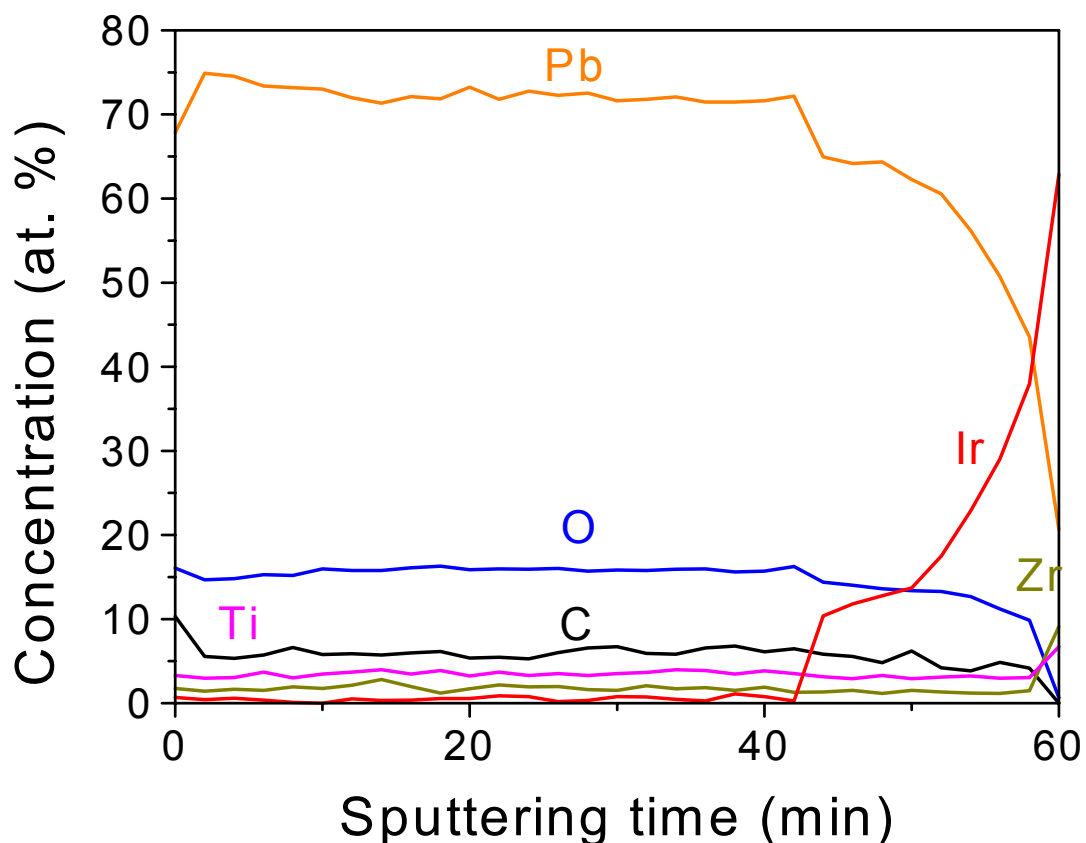


**Figure 5-8:** XPS depth profiles of a PZT film grown on Ir/TiO<sub>2</sub>/SiO<sub>2</sub>/Si substrate at 550 °C.

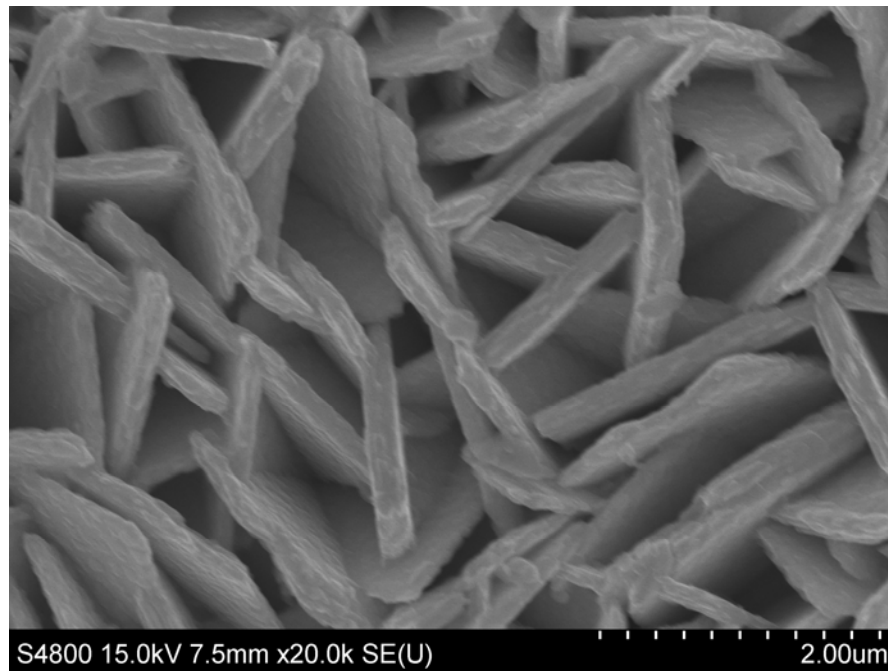


**Figure 5-9:** SEM picture of surface of a PZT film in the case of a huge excess of lead (Pb: 73 at%).

In order to obtain stoichiometric PZT films and to avoid the formation of additional lead oxide the content of lead in the films has to be decreased. The formation of lead oxide on the film surface may be initiated by the increased growth of lead oxide on an Ir surface. The high growth rate of a PZT film on iridium and the increased concentration of lead in it is explained to be due to a strong surface interaction of the lead precursor with the iridium coated substrate [89].

Figure 5-10 shows the elemental composition of a PZT film grown on an Ir/TiO<sub>2</sub>/SiO<sub>2</sub>/Si substrate at 550 °C versus the sputtering time. The injection time of tetraethyl lead has been lowered by a factor of 5, but it is not enough to avoid the formation of lead oxide at the surface. Thus, a PZT layer with only a perovskite phase has not been obtained.

There are five zones in the PZT/Ir/SiO<sub>2</sub>/Si structure: the top surface, the PZT film, the Ir film, the SiO<sub>2</sub> layer, and the underlying Si substrate. The high amount of Pb close to the surface is due to segregation of Pb at the surface of the PZT film; Pb oxidizes and forms PbO. Only a negligible amount of carbon is observed on the surface. After two minutes of sputtering, the concentration of the carbon significantly decreases.

Carbon is not incorporated in the PZT film, but absorbed at the substrate surface probably after film deposition.

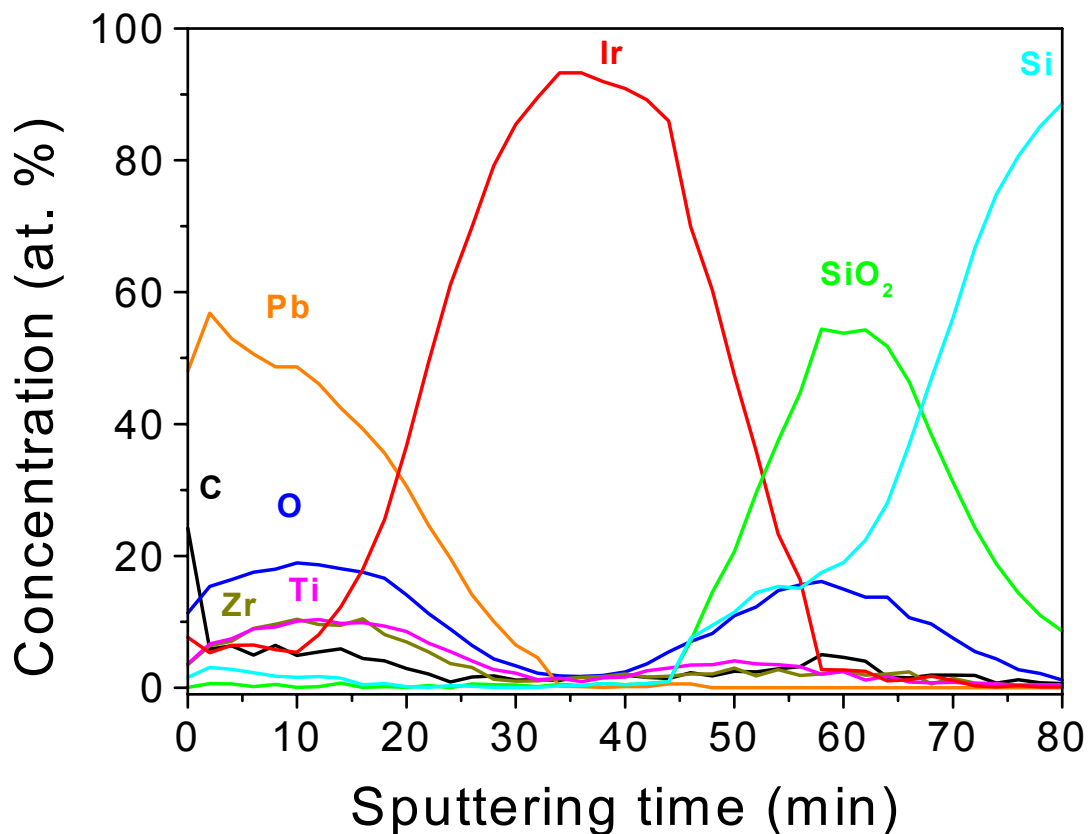


**Figure 5-10:** XPS depth profiles of a PZT film grown on a Ir/TiO<sub>2</sub>/SiO<sub>2</sub>/Si substrate at 550 °C.

As can be seen in figure 5-10, a steady-state composition of the PZT film is reached after two minutes Ar<sup>+</sup> bombardment. After ten minutes of sputtering the concentration of Pb decreases and iridium appears. Possibly iridium diffuses into the PZT layer at the relatively high substrate temperatures.

The XPS spectra of an as-deposited PZT thin film grown on a Ir/TiO<sub>2</sub>/SiO<sub>2</sub>/Si substrate at 450 °C and reactor pressure of 0.5 mbar is shown in figure 5-11. The surface layer of this film contains 22.3 at% carbon, 46.3 at% oxygen, 16.1 at% lead, 8 at% zirconium and 7.4 at% titanium.

After the wafer surface has been cleaned and the adsorbed surface contamination has been removed by Ar<sup>+</sup> sputtering for 60 seconds the elemental composition of this PZT thin film is the following: C – 0 at%, O – 59.5 at%, Pb – 20.69 at%, Zr – 10.28 at%, and Ti – 9.53at%. This film exhibits the lead-enriched morphotropic composition Pb<sub>1.05</sub>(Zr<sub>0.52</sub>Ti<sub>0.48</sub>)O<sub>3</sub>.

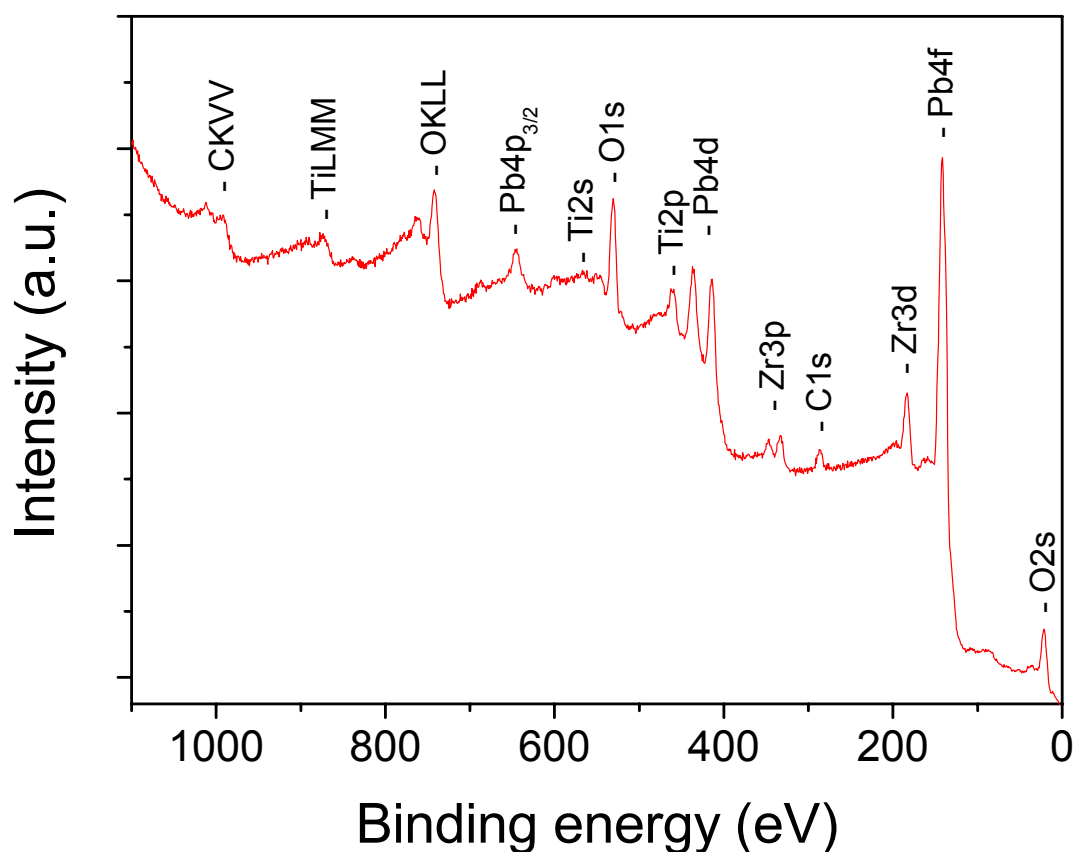


**Figure 5-11:** XPS spectra of a PZT thin film with a morphotropic composition.

In a further deposition process the injection rate has been lowered by an order of magnitude in comparison to the sample discussed above (figure 5-8). The surface of the film is rather smooth. But, a second phase has been observed in the as-deposited film (figure 5-12). The XRD measurements presented in section 5.1.2.2 show that this second phase is crystalline lead oxide.

The XPS-depth profile measurements (not shown) reveal that a high concentration of lead can be observed only at the surface region. This high amount of Pb near the surface may be due to the segregation of Pb at the surface of the PZT film. These excess Pb atoms can be easily oxidized to form PbO.

Therefore, even though excess lead is necessary to stabilize the perovskite structure for this lead-based ceramic, a too high excess of lead in the layer may cause the formation of unwanted second phases.

If the content of lead in the deposited film is lower as it is necessary to stabilize the perovskite structure, about 20 at%, the film will be amorphous and no crystal phases can be observed (see figure 5-13).

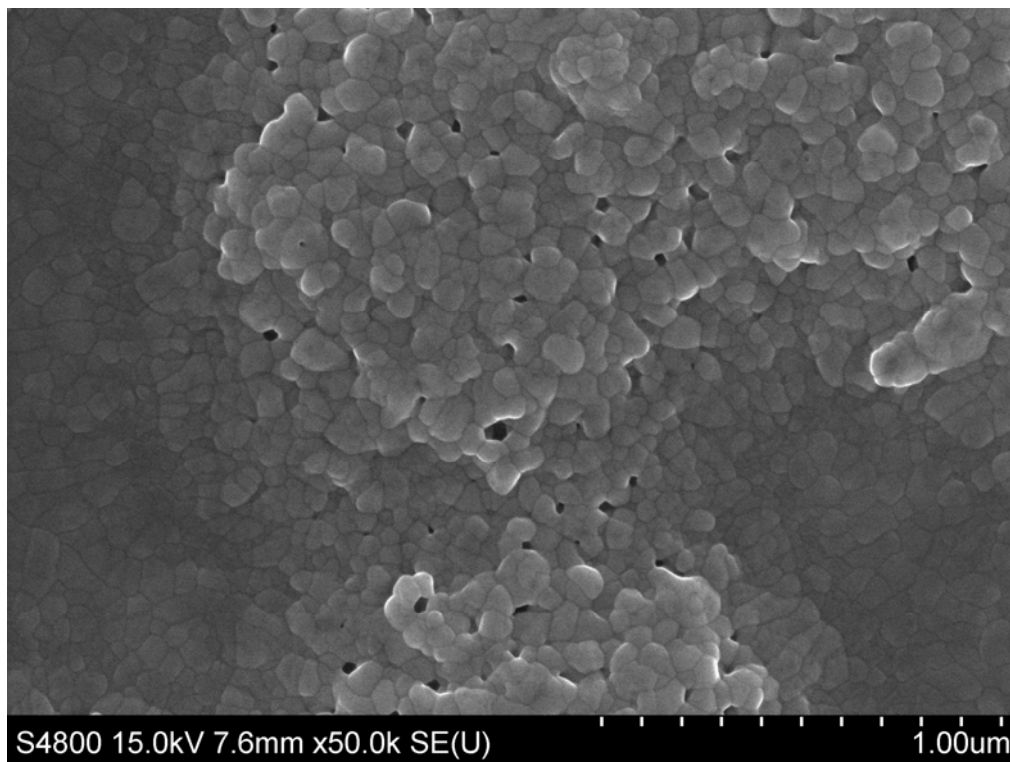


**Figure 5-12:** SEM image of the substrate surface in the case of a negligible excess of lead in the film. Pb concentration is 21 at%.

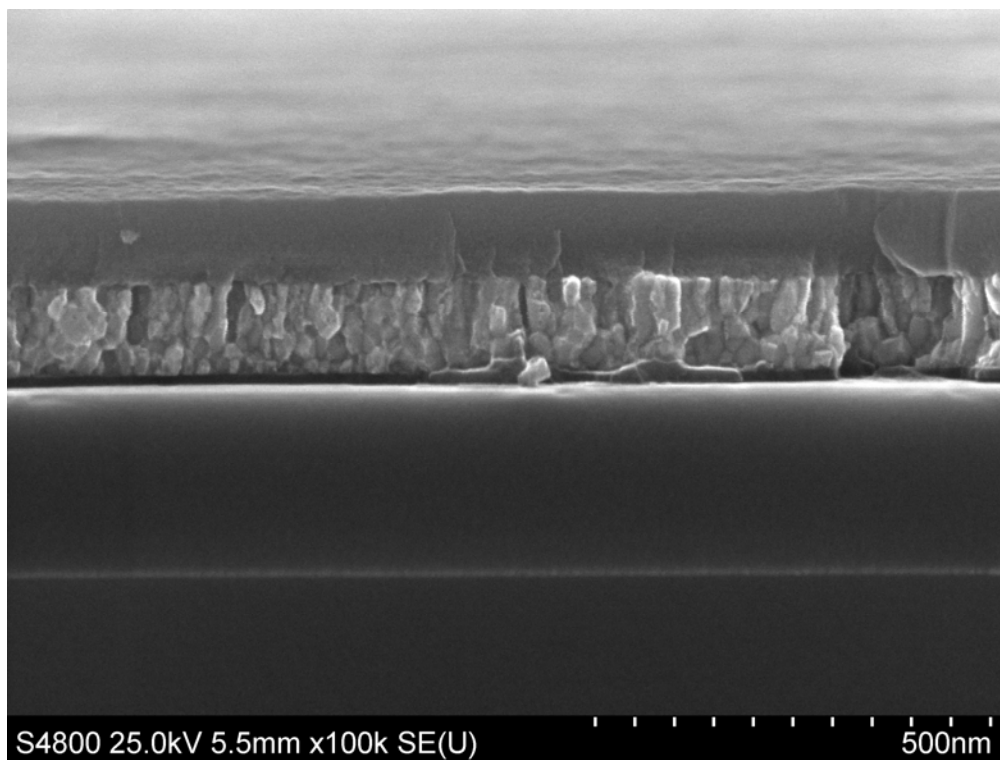


**Figure 5-13:** Cross-sectional view of an amorphous PZT film deposited on a Ir/TiO<sub>2</sub>/SiO<sub>2</sub>/Si substrate. Pb concentration is 17 at%.

### 5.1.2.2 Investigation of the Crystal Structure by X-ray Diffraction

It is well-established that the apparent nucleation energy is much higher than the apparent grain-growth energy in PZT perovskite phase formation [90]. Peng and Desu have investigated the structure growth in PZT films by an optical method and have showed that the effective activation energies for the nucleation of perovskite are much higher than those for its growth [91]. In other words the nucleation energy is the primary barrier for the perovskite crystallization.

In the phase evolution of PZT films, amorphous PZT films are first transformed into the pyrochlore phase, which is non-ferroelectric and metastable at low temperatures. The non-ferroelectric pyrochlore phase is then transformed into the perovskite phase, which is ferroelectric and stable at high temperatures. Since the pyrochlore phase shows non-ferroelectric properties, the pyrochlore phase should be minimized for obtaining high quality ferroelectric films.

The perovskite phase is evolved from the pyrochlore phase by nucleation and grain growth [92]. The nuclei of the perovskite structure originate from the pyrochlore matrix and they grow until the film has completely changed to the ferroelectric perovskite phase.

Figure 5-14 shows the X-ray diffraction patterns of as-deposited PZT films with different content of lead.

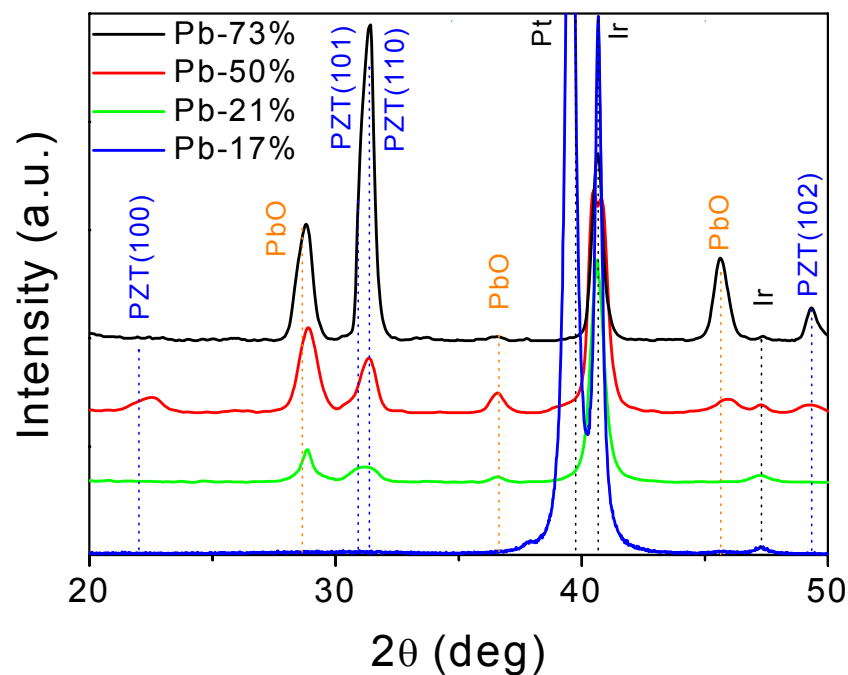


**Figure 5-14:** XRD patterns of PZT films deposited on Ir coated Si substrates for different concentrations of lead.

The XRD analysis confirms our assumption concerning the phase composition of the deposited films in dependence on the dosage of the lead precursor.

The presence of the perovskite phase is observed for all as-deposited films in which the concentration of lead is close or above 20 at%. It is generally known that the pyrochlore phase tends to be formed during PZT film fabrication at lower process temperature. The fact, that the peaks, which correspond to the pyrochlore phase, can not be detected in the XRD patterns of as-deposited films, proves that the thermal energy at a temperature of 450 °C is sufficient to obtain the perovskite phase in PZT films deposited by liquid-delivery MOCVD.

The films with a lead concentration of 73 at% have not a preferred orientation. Additionally to (110), (101), (102)-textured PZT a significant peak at 29° is observed. This peak corresponds to lead oxide. The presence of the lead oxide phase is also observed in a film with 50 at% lead, and even after reducing the lead content down to 21 at%. Furthermore, in the film with a concentration of lead of about 50 at%, the intensity of the (102) peak is lower than for 73 at% lead and additionally the (100) peak appears. This shows that tetragonal and rhombohedral phases are present in the deposited film. The presence of these both phases is possible only close to the morphotropic phase boundary (MPB). The morphotropic phase boundary, therefore, should not be understood as a line but rather as a region in which the tetragonal and rhombohedral phases coexist.

The results of XRD and SEM analyses indicate that the grown films are crystallized during PZT deposition and that the formation of the perovskite phase is completed without additional annealing. Also, the differences between the XRD-spectra of figure 5-14 indicate that the PbO formation depends on the deposition conditions of the MOCVD-PZT films. High lead concentrations may cause the formation of a lead-rich liquid phase during deposition and some of the liquid phase may crystallize to PbO at the surface during cooling down. Such formation of a lead rich liquid phase has been reported by many researchers, such as Kington *et al* (1983), Xu (1991), Kakegawa *et al* (1995) and Akbas *et al* (1995). They attributed the formation of this liquid phase to the low melting point of PbO [93].

If the concentration of lead is lower than it is necessary to stabilize the perovskite structure, the films are amorphous. Two peaks of high intensity near 40° are caused by the Ir-bottom and by the Pt-top electrodes.

Figure 5-15 shows the XRD patterns of a PZT film with a content of lead of 17 at% on a Ir/TiO<sub>2</sub>/SiO<sub>2</sub>/Si substrate which has been annealed at various temperatures ranging from 600 °C to 800 °C.

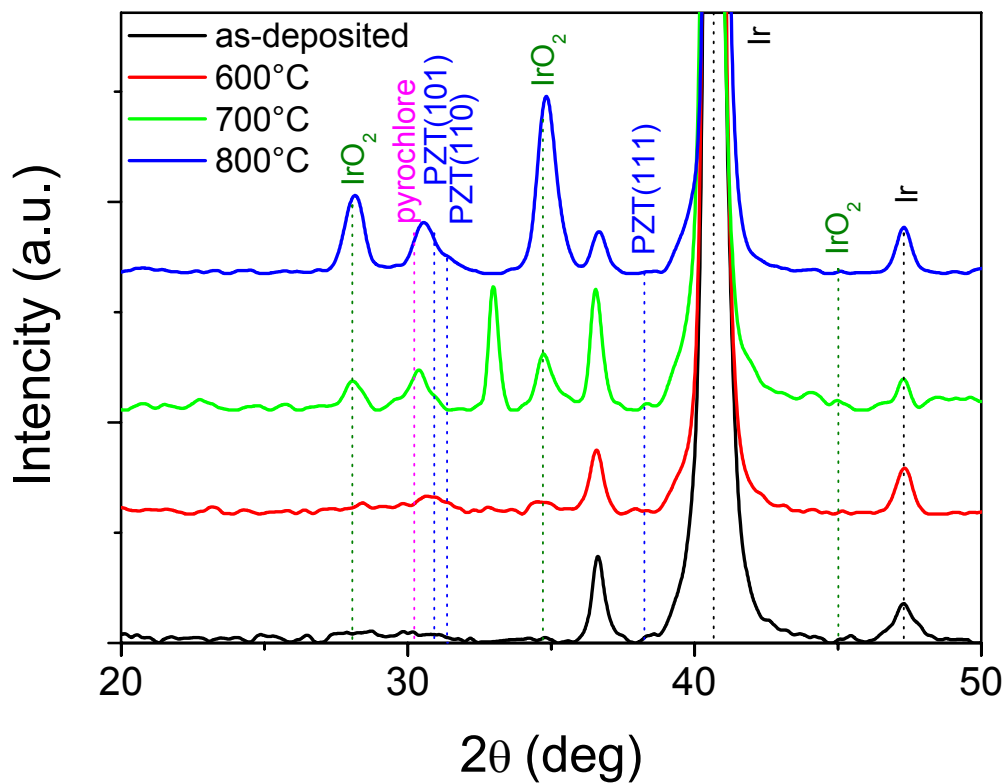


**Figure 5-15:** XRD patterns of PZT films with deficiency of lead before and after annealing.

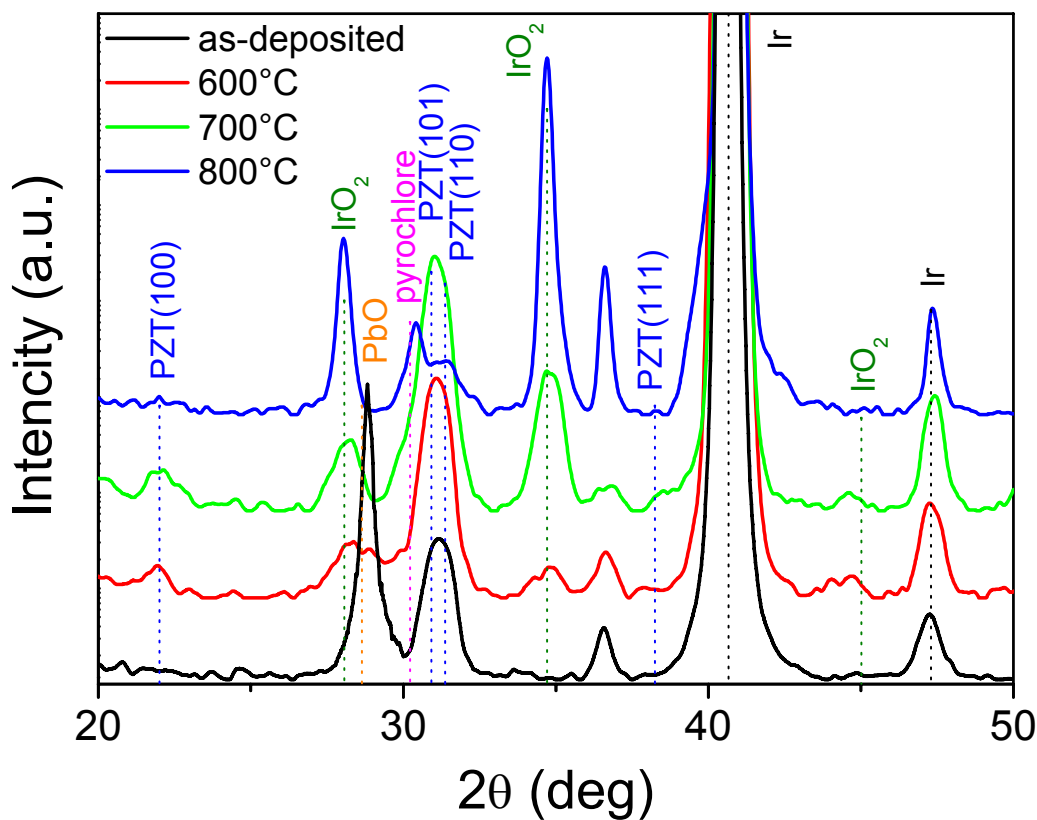
As-deposited films with a deficiency of lead are amorphous and only the peaks caused by the Ir/TiO<sub>2</sub> stack electrode can be observed. The PZT perovskite phase appears after annealing at 600 °C, and the PZT (101) peak is rather small. Additional to the perovskite PZT a pyrochlore phase appears at 600 °C. As the annealing temperature is increased, the (101) peak increases due to a further enhancement in crystallization. After annealing at 700 °C the increase of the peak which corresponds to the oriented pyrochlore phase confirms the preferred growth of the pyrochlore phase in the PZT film with an insufficient amount of lead. After annealing at 800 °C the (101) perovskite peak only increases very slightly while the pyrochlore peak grows strongly. The XRD results reveal that the films contain both, perovskite and pyrochlore phases, in the case of a lead lack. Post deposition annealing at higher temperatures can not vanish the non-ferroelectric pyrochlore phase but in contrary, it promotes the growth of it.

Figure 5-16 shows the XRD patterns for a PZT thin film with 21 at% lead annealed at different temperatures. Already the as-deposited PZT film is crystalline and additionally to the (110) oriented perovskite phase a second phase of lead oxide can be observed due to the small excess of lead. Hendrickson *et al.* [94] report that a PbO layer on the top of the PZT thin films

results in improved properties and helps to prevent the formation of a pyrochlore surface layer during crystallization. After annealing the peak which corresponds to the (101) oriented tetragonal lead oxide has completely disappeared. Thus, post-deposition annealing can reduce a small amount of excess lead. The  $\text{Pb}_{1.05}(\text{Zr}_{0.52}\text{Ti}_{0.48})\text{O}_3$  films prepared on iridium layers are completely crystallized into the perovskite phase at the rather low annealing temperature of 520 °C.

Annealing of the thin films at 600°C results in the formation of the pyrochlore phase. The appearance of the pyrochlore phase in the annealed films is related to a significant decrease of lead concentration during the temperature treatment. The lead loss has also been observed in PZT-films fired in an air atmosphere by Torah *et al.* [95] and is attributed to the increased volatility of the PbO at annealing temperatures above 600 °C.

The peak corresponding to the pyrochlore phase significantly increases after annealing the PZT films at 700 °C and 800 °C. The increase of the pyrochlore peak and the change of the orientation of the perovskite phase from (110) to (101) can be explained by the loss of lead.



**Figure 5-16:** XRD pattern of PZT films with a composition close to the stoichiometric before and after annealing.

The shape of the XRD-pattern of the PZT film annealed at 800 °C is similar to the pattern of a film with a deficiency of lead.

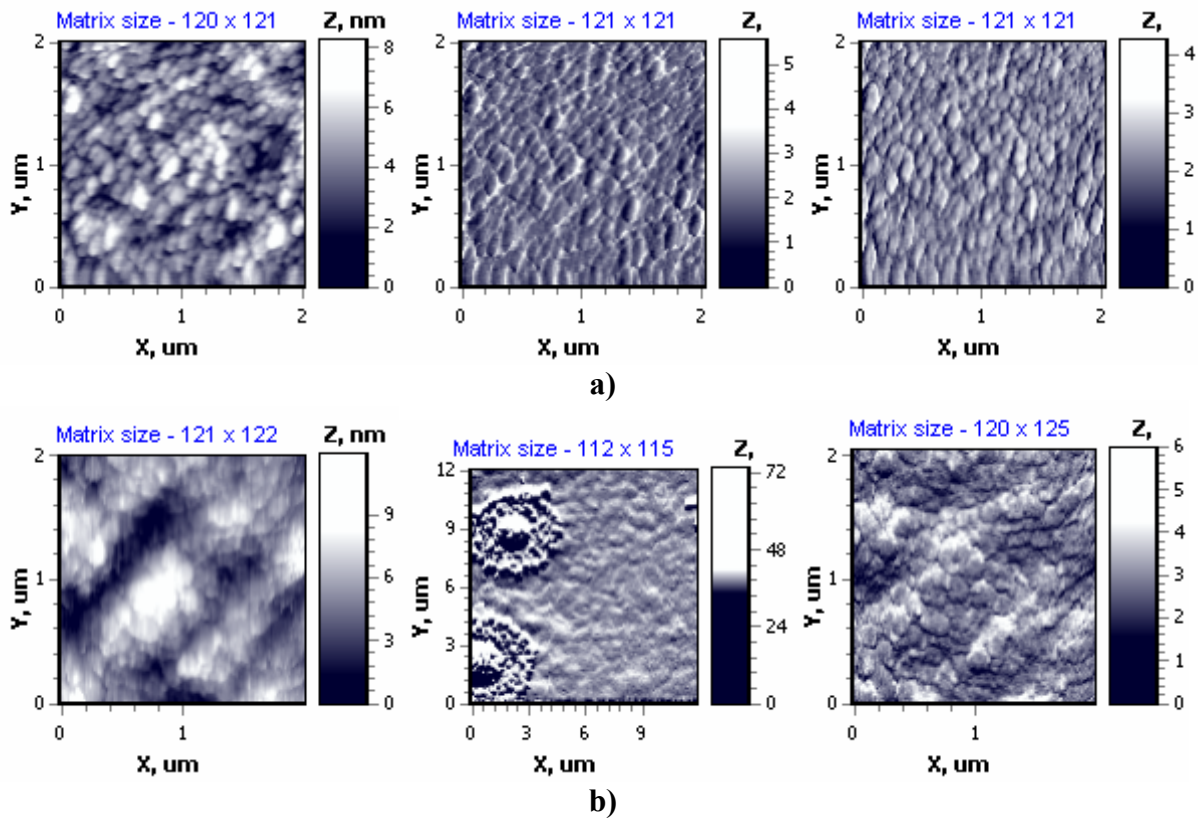
All XRD patterns of the annealed film in figures 5-15 and 5-16 show two strong peaks at 28.05° and 34.7° the height of which increases with the annealing temperature. These two peaks correspond to iridium oxide and indicate the oxidation of the bottom iridium electrode during the post-deposition annealing processes. There are two possible ways for iridium oxidation: thermal diffusion of oxygen from the gas ambient and thermal interdiffusion. It is assumed that the diffusion of oxygen through the PZT from the PZT surface is the oxygen source for the iridium oxidation. Molecular oxygen should be too large to diffuse in the PZT lattice [96]. Cross *et al.* report that the oxygen diffusion rate is related to the concentration of oxygen vacancies within the material and that the diffusion rate is temperature dependent [96]. Therefore one can conclude that oxygen vacancies may be present in the PZT films and that their density increases at elevated annealing temperatures.

Previous studies have shown that oxygen plays a significant role in the growth of the PZT perovskite phase. The lack of oxygen, i.e. the movement of oxygen vacancies in the ferroelectric film have also been postulated to cause fatigue or polarization degradation [97,98].

### 5.1.2.3 Atomic Force Microscopy

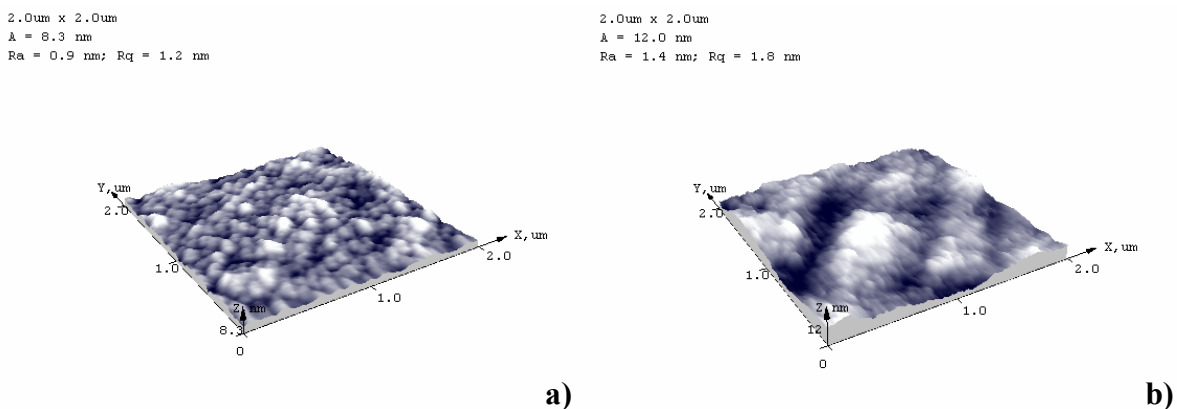
The surface morphology of the films has been characterized by atomic force microscopy (AFM) using contact and tapping modes. Figure 5-17 illustrates the surface morphology of PZT films with 17 at% Pb before and after annealing at 800 °C. Before annealing the films exhibit a dense microstructure with no cracks and voids. However, lot of the pockets of fine grains were observed in the PZT films annealed at 800 °C, which are attributed to the pyrochlore phase [92]. The number of large grains which correspond to the perovskite phase is very low. This confirms the predominant growth of crystals of the pyrochlore phase in the case of a lead deficiency.

Figure 5-17(b) shows that two circular rosettes grow from the surrounding nanoscaled pyrochlore matrix and that a core exists at each rosette's centre [99]. The respective average roughness ( $R_a$ ) for these perovskite rosettes and the matrix are 14.96 and 1.4 nm. Formation of round grain structures, so-called "rosettes", on the surface of PZT thin films prepared by a sol-gel process at a mole ratio  $Zr/Ti = 52/48$  have been also reported by several research groups [100,101]. Atsuki *et al.* attributed the rosette formation to a lead deficiency in the annealed PZT films [101].



**Figure 5-17:** AFM images (plan view) of PZT (Pb: 17 at%) thin film surfaces before (a) and after annealing at 800 °C (b).

The tilted AFM view of figure 5-18 indicates that the root mean square roughness ( $R_q$ ) of the PZT film before annealing is 1.2 nm. After annealing at 800 °C the  $R_q$ -value increases up to 1.8 nm due to the formation of the crystalline perovskite (white area) and pyrochlore (dark area) phases. Crystalline perovskite appears in the AFM image as white area because of its large grain sizes.



**Figure 5-18:** AFM images (tilted view) of PZT (Pb: 17 at%) thin film surfaces before (a) and after annealing at 800 °C (b).

PZT thin films with a Pb content of 21 at% have also been investigated by AFM. Figure 5-19 shows plan-view images of as-deposited and annealed (800 °C) films. The as-grown films show a dense structure without any rosette-type microstructures. The pyrochlore phase pockets can also be observed.

It has been reported for PZT films, that the perovskite phase nucleates between the film and the substrate, and then grows towards the surface of the film [92,102,103].

However, the present films processed at 520 °C exhibit good ferroelectric properties (see section 5.1.3.1), indicating that the pyrochlore phase pockets are only confined to the surface of the films, and the bulk of the film predominantly shows the perovskite phase. As the annealing temperature is increased to 800 °C, a lot of fine grains which are attributed to the pyrochlore phase can be observed additionally to the large grains.

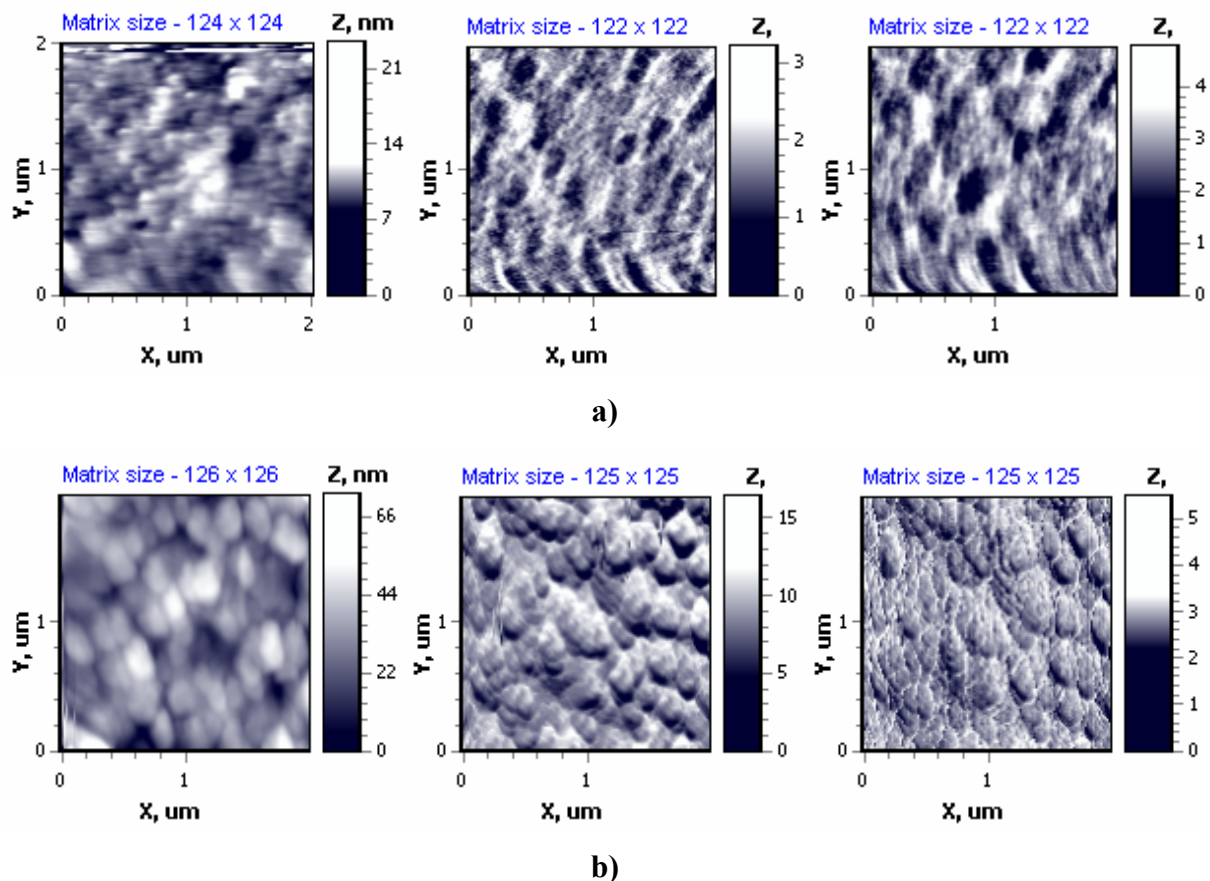
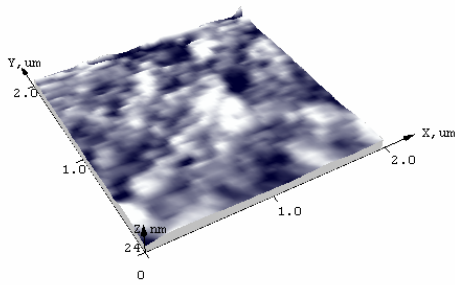


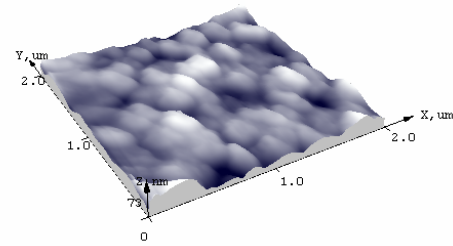
**Figure 5-19:** AFM images (plan view) of PZT (Pb: 21 at%) thin film surfaces before (a) and after annealing at 800 °C (b).

2.0um x 2.0um  
 $\lambda = 23.6 \text{ nm}$   
 $R_a = 0.8 \text{ nm}; R_q = 1.2 \text{ nm}$



a)

2.0um x 2.0um  
 $\lambda = 73.0 \text{ nm}$   
 $R_a = 7.1 \text{ nm}; R_q = 8.9 \text{ nm}$



b)

**Figure 5-20:** AFM images (tilted view) of PZT (Pb: 21 at%) thin film surfaces before (a) and after annealing at 800 °C (b).

The tilted AFM view of figure 5-20 indicates that the root mean square roughness ( $R_q$ ) of the PZT film before annealing was 1.2 nm. The  $R_q$ -value is the same as for PZT films with a lead deficiency. It is much lower as it should be for films with a perovskite structure [104]. This phenomenon can be explained by the presence of lead oxide crystals at the film surface. After annealing at 800 °C the value of the  $R_q$  increases up to 8.9 nm. This is due to disappearance of the lead oxide phase and to the formation of the crystalline perovskite and pyrochlore phases.

### 5.1.3 Electrical Characterization

The metal/PZT/metal structure was used in order to investigate the electrical properties. The top platinum or iridium contacts were deposited by PVD using shadow masks. After metallization, the wafers were divided into chips and the PZT film was etched off in one corner of a chip by an etch solution consisting of  $\text{HNO}_3$ , HF and HCl (6%, 2% and 1%) acids. By doing so the Ir bottom electrode could be contacted.

In the case of a high concentration of lead in the deposited film an electrical characterization could not be performed as the substrate surface of a such film was very rough and the top electrode metal did not adhere on the surface.

Electrical measurements were carried out on films with concentrations of elements close to the stoichiometric (Pb: 21 at%) composition and on films with a small deficiency of lead (Pb: 17 at%).

### 5.1.3.1 Ferroelectric Properties

Polarization versus applied electric field measurements have been carried out using the measurement set-up described in section 4.6.2. Figure 5-21 shows a typical hysteresis loop obtained for an as-deposited PZT thin film which shows a PbO phase additional to the ferroelectric perovskite phase.

In such an as-deposited film the current due to ferroelectric switching is rather low in comparison to the leakage current. This explains the shape of the observed hysteresis loop of figure 5-21. It is severely depending on the Pb content of the film which can be adjusted by annealing and by the annealing temperature [105].

The high values of the leakage current can be understood by the presence of the additional PbO phase and are due to the increased length of the grain boundaries, which are well known as good leakage current paths. The leakage current increases linearly with the length of the grain boundary [106].

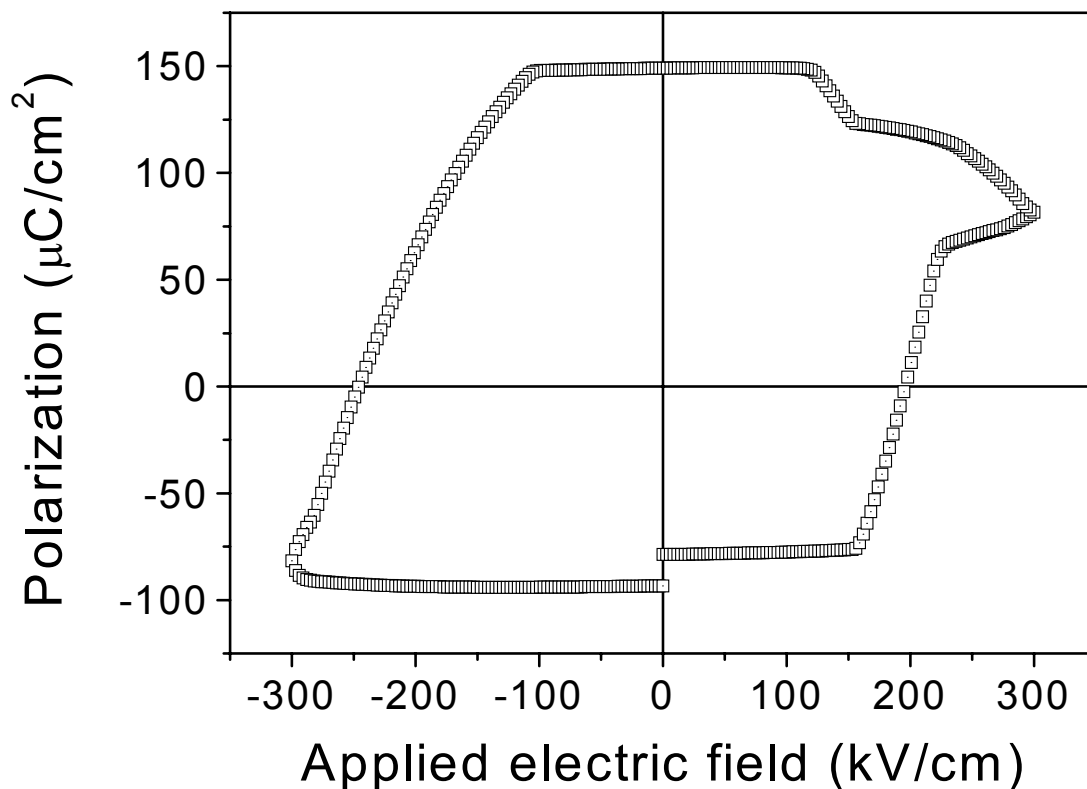


**Figure 5-21:** Hysteresis loop of a capacitor with an as-deposited PZT film which exhibits an additional PbO phase.

After deposition PZT films with a lead content of 21 at% exhibit ferroelectric hysteresis loops as shown in figure 5-22. These films are good insulators with a leakage current density lower than  $10^{-3}$  A/cm<sup>2</sup> at an applied electric field of 200 kV/cm, see also section 5.1.3.2.

A formation of lead oxide can not be observed on such a wafer. Only some small PbO-islands can be found on it. Therefore, good ferroelectric properties are related to PZT films free of lead oxide [105].

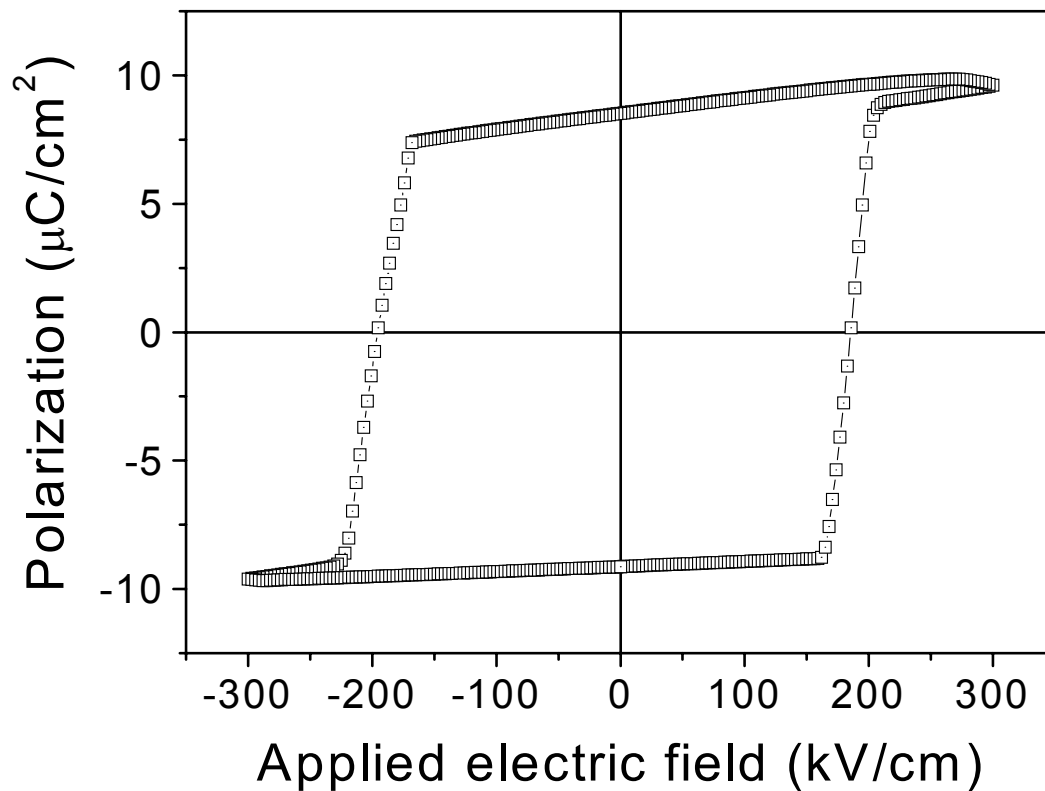


**Figure 5-22:** Hysteresis loop of an as-grown PZT film showing no PbO phase.

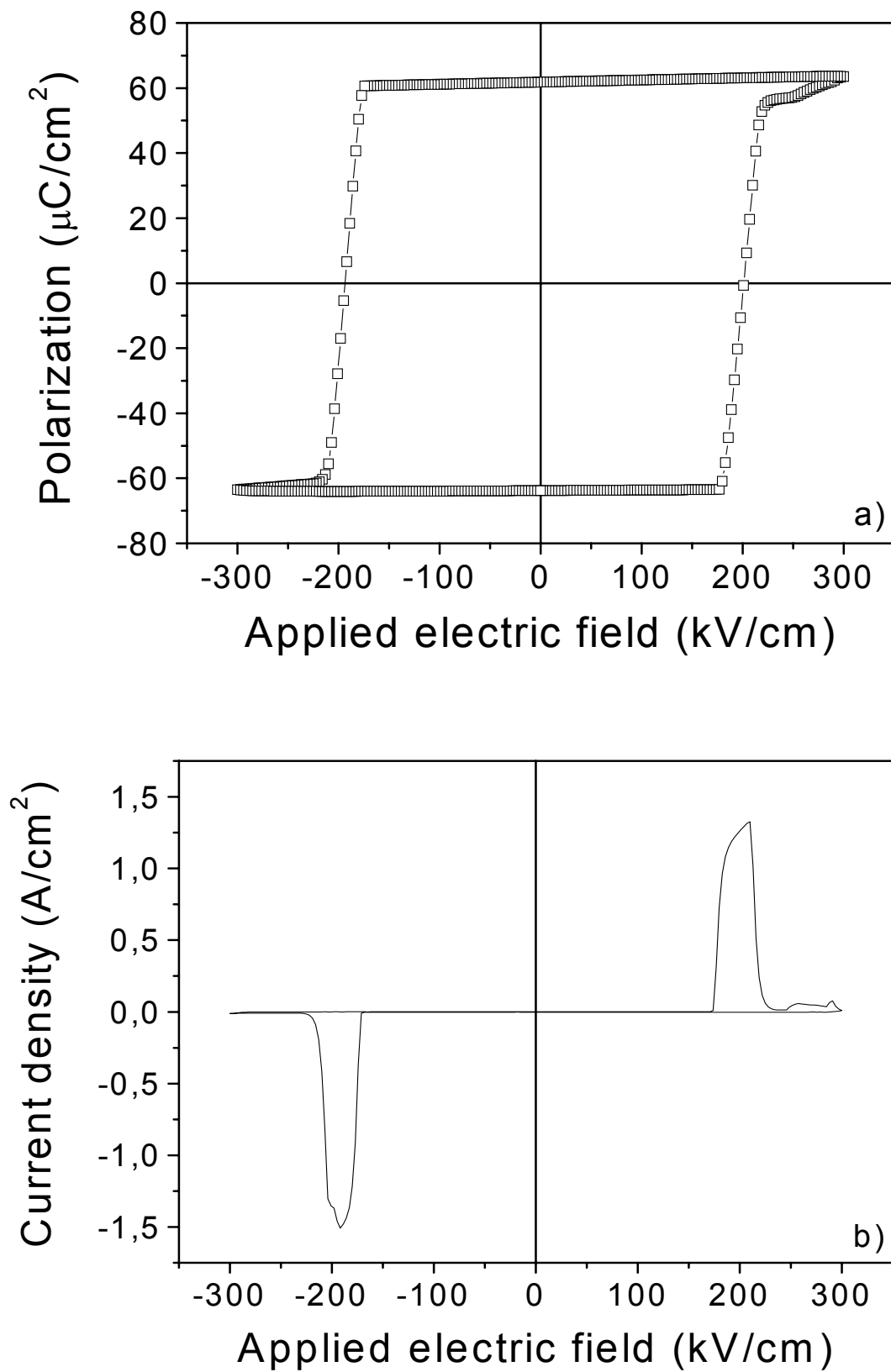


**Figure 5-23:** Ferroelectric hysteresis loop (a) and I-V characteristic (b) of a PZT film on an Ir/TiO<sub>2</sub>/SiO<sub>2</sub>/Si substrate after annealing at 520°C.

The  $\text{Pb}_{1.05}(\text{Zr}_{0.52}\text{Ti}_{0.48})\text{O}_3$  film annealed at  $520\text{ }^\circ\text{C}$  exhibits well-defined P-E hysteresis loops, see figure 5-23(a). This hysteresis loop has an almost rectangular shape, which is typical for Ti-rich PZT films. These films reveal a high remanent polarization of  $P_r = 60\text{ }\mu\text{C}/\text{cm}^2$  and a coercive electric field of  $E_c = 200\text{ kV}/\text{cm}$  at an applied voltage of  $3\text{ V}$ . The well-saturated hysteresis loop of films annealed at  $520\text{ }^\circ\text{C}$  indicates that the films are predominantly in the perovskite phase. These values are much higher in comparison to those reported for PZT films prepared at lower temperatures by sputtering [44] or sol gel [46] techniques.

Figure 5-23(b) shows a current density versus applied electric field strength characteristic of a PZT film annealed at  $520\text{ }^\circ\text{C}$ . This  $j$  versus  $E$  curve is monitored in parallel to the hysteresis curve of figure 5-23(a). It can be easily seen that the switching pulses correspond to the switching of the polarization of the ferroelectric film.

After a subsequent annealing at  $600\text{ }^\circ\text{C}$ , the PZT films behave like a paraelectric with only a small ferroelectric contribution, as can be seen in figure 5-24. This behavior is due to a further phase and compositional change.

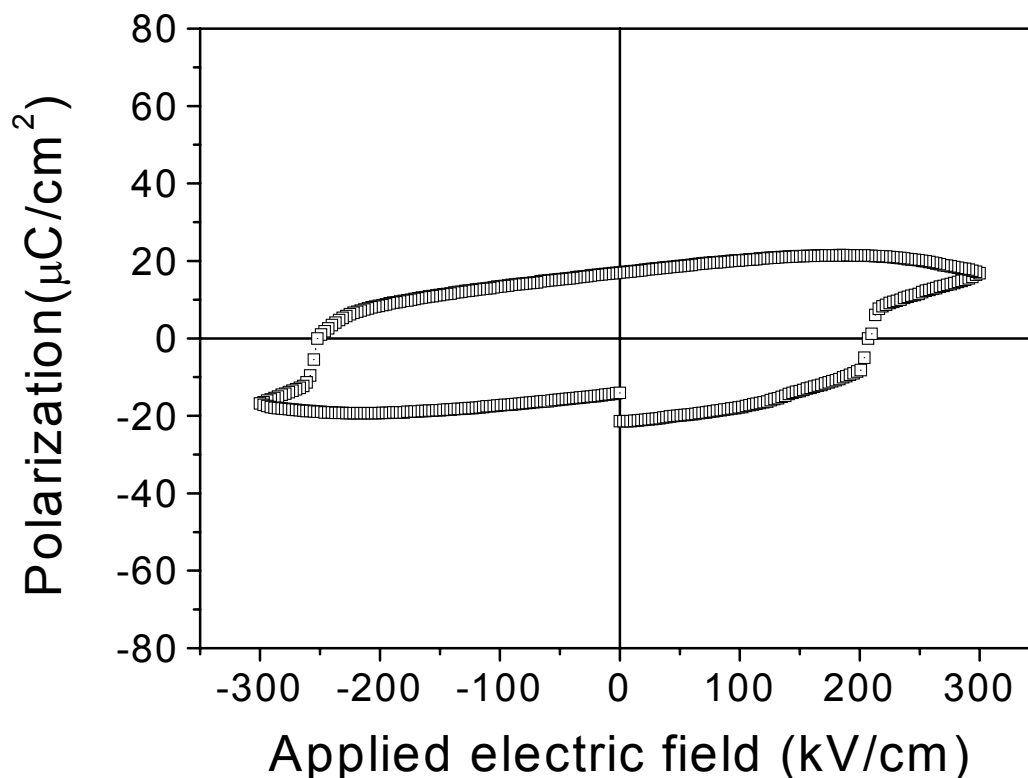


**Figure 5-24:** Typical polarization vs. applied electric field curve of a PZT film annealed at  $600\text{ }^\circ\text{C}$ . The Pb content is 21 at%.

Phase as well as a composition have been investigated by XRD and XPS, respectively. Films annealed at 600 °C show the non-ferroelectric pyrochlore phase combined with a deficiency of lead, see section 5.1.2.1 for XPS and section 5.1.2.2 for XRD results. This non-ferroelectric pyrochlore phase is, therefore, responsible for these observed polarization versus applied electric field curves.

The results of the ferroelectric measurements strongly differ for as-deposited PZT films with a too small lead content. As mentioned above in section 5.1.2.2, for as-grown PZT films with a concentration of lead of about 17 at% no peak which corresponds to crystalline lead zirconate titanate can be observed in the XRD pattern. As-deposited PZT films with 17 at% lead are amorphous.

Figure 5-25 shows a typical polarization vs. applied electric field curve of an as-deposited PZT film with 17 at% lead. It is not possible to recognize the typical ferroelectric loop.

Amorphous films are, however, no good insulator; they conduct to some degree. This conduction is either linear, that is, proportional to the electric field, or nonlinear, then it obeys a power law. In the case of a linear dielectric with linear conduction, the straight line figure changes to an ellipse which is typical for a lossy linear capacitor.

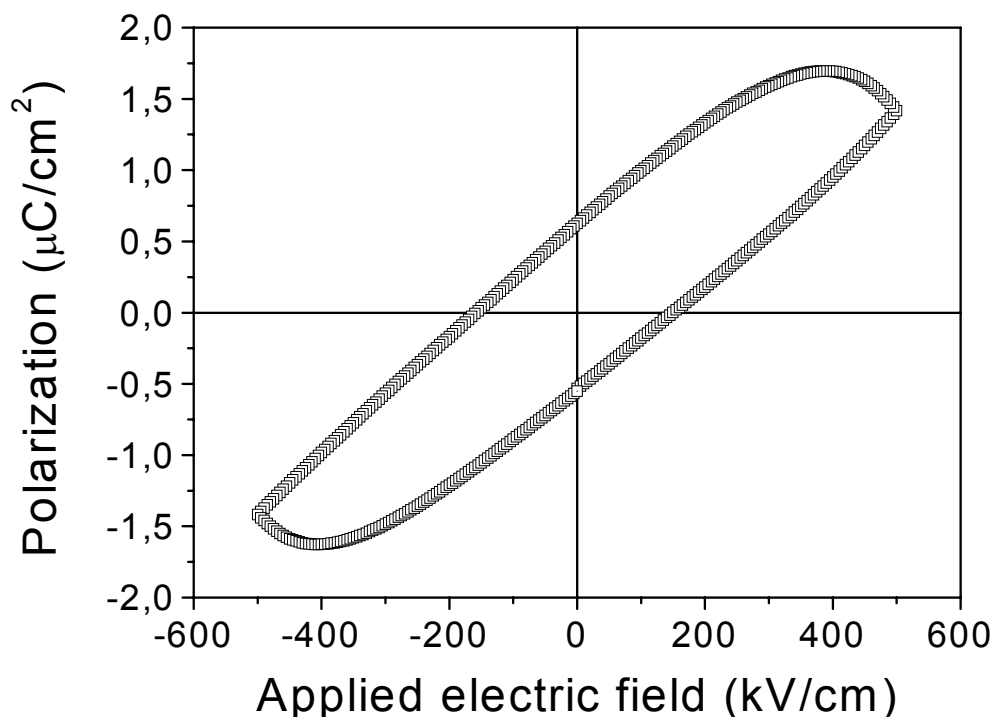
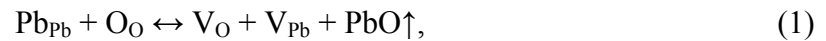


**Figure 5-25:** Typical polarization vs. applied electric field curve of an as-deposited PZT film with 17 at% lead.

Results of the electrical measurements do not show any improvement of the ferroelectric properties after annealing. This can be understood by the preferred growth of the pyrochlore phase in PZT films with a low lead content.

### 5.1.3.2 Fatigue Properties

PZT films which have been investigated in this work show poor fatigue behaviour. Mostly this phenomenon is related to the interface between the PZT film and the electrode [107]. In devices with elemental metal electrodes, the polarization fatigue has been explained by the migration of oxygen to the electrode–ferroelectric interface and by the formation of oxygen vacancy clusters which can inhibit the switching [107]. Thermal interdiffusion of the oxygen in the lead zirconate titanate is proposed in section 5.1.2.2 as the most probable way for oxidation of iridium contacts. Furthermore, Desu *et al.* noted that a high concentration of oxygen vacancies in PZT films can result in PbO volatilization during annealing [108]. This process can be described by a quasi-chemical reaction (in Kroeger-Vink notation) as follows:



where  $\text{Pb}_{\text{Pb}}$  and  $\text{O}_{\text{O}}$  represent occupied Pb and O sites in the lattice, respectively,  $\text{V}_{\text{O}}$  and  $\text{V}_{\text{Pb}}$  represent vacancies of oxygen and lead, respectively [108].

A second possible explanation of fatigue involves the formation of layers at the electrode interfaces which effectively reduce the total electric field applied across the device or inhibit the nucleation of oppositely polarized domains [109,110].

Most probably, fatigue can be minimized by decreasing the oxygen vacancy concentration with donor doping (e.g., Nb) and by the use of conductive oxide electrodes (e.g.,  $\text{RuO}_2$ ), as oxide electrodes do not consume oxygen at the electrode/ferroelectric interface in contrast to pure metal electrodes which can be oxidized during annealing. Formed oxygen vacancies represent potential volume traps and can contribute to a space charge build-up which has a detrimental impact on fatigue.

Insertion of a buffer layers which can prevent thermal interdiffusion between the film and electrodes may be effective for diminution of fatigue [111]. Another important aspect is the lowering of the annealing temperature as much as possible in order to reduce the lead losses.

### 5.1.3.3 Dielectric Properties

The dielectric properties of PZT thin films have been determined with regard to the dielectric constant  $\epsilon$ . The capacitance-voltage (C-V) measurements of the metal-ferroelectric-metal (MFM) structure have been carried out at room temperature by using an Agilent 4284A Precision LCR Meter, for detailed information see section 4.6.2.

For these measurements, Ir electrodes have been deposited on the top of the films through a shadow mask by physical vapor deposition. The area of the circular dots is in the range from  $0.03 \text{ mm}^2$  to  $0.785 \text{ mm}^2$ .

The value of the dielectric constant is strongly depending on the annealing temperature. An as-deposited film has a dielectric constant of about 50. The dielectric constant of an as-deposited PZT film of 21 at% lead seems to be constant regardless on the applied voltage (see figure 5-26). The dielectric constant has been calculated from the C-V characteristic of the Ir-PZT-Ir structures measured in positive ( $\epsilon$ ) and negative ( $\epsilon'$ ) directions of the applied voltage.

Figure 5-27 shows the small signal dielectric constant as a function of the annealing temperature for a 120 nm thick PZT film with a lead content of 21 at%.

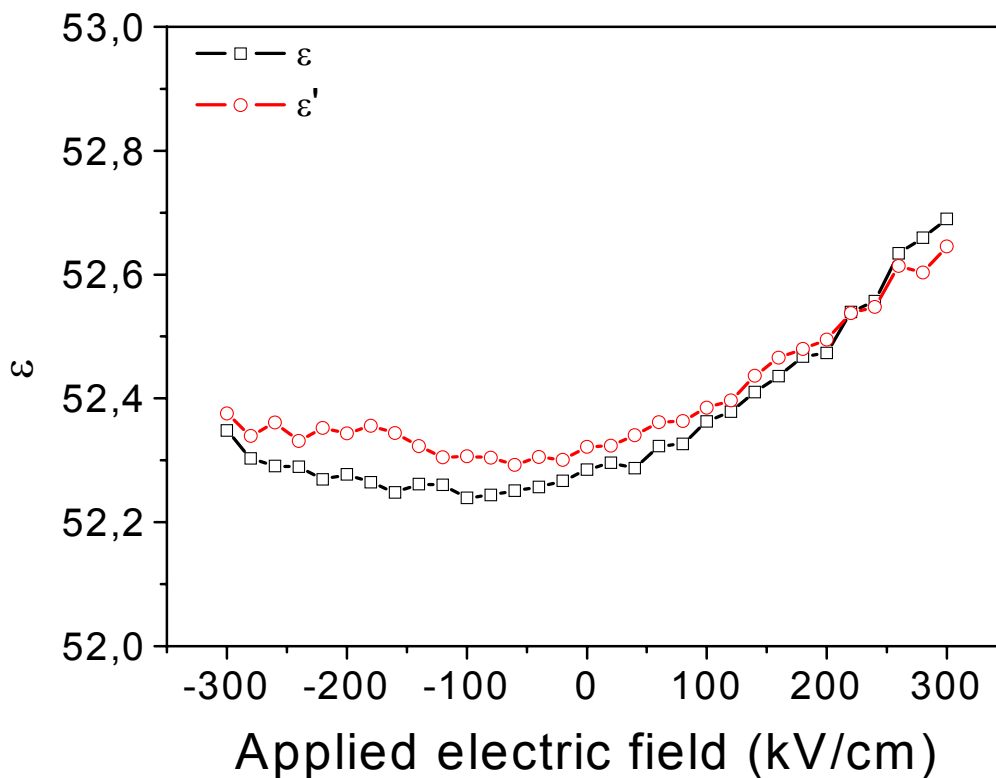


**Figure 5-26:** Dielectric constant of an as-deposited lead zirconate titanate film of 21 at% lead vs. the applied electric field.

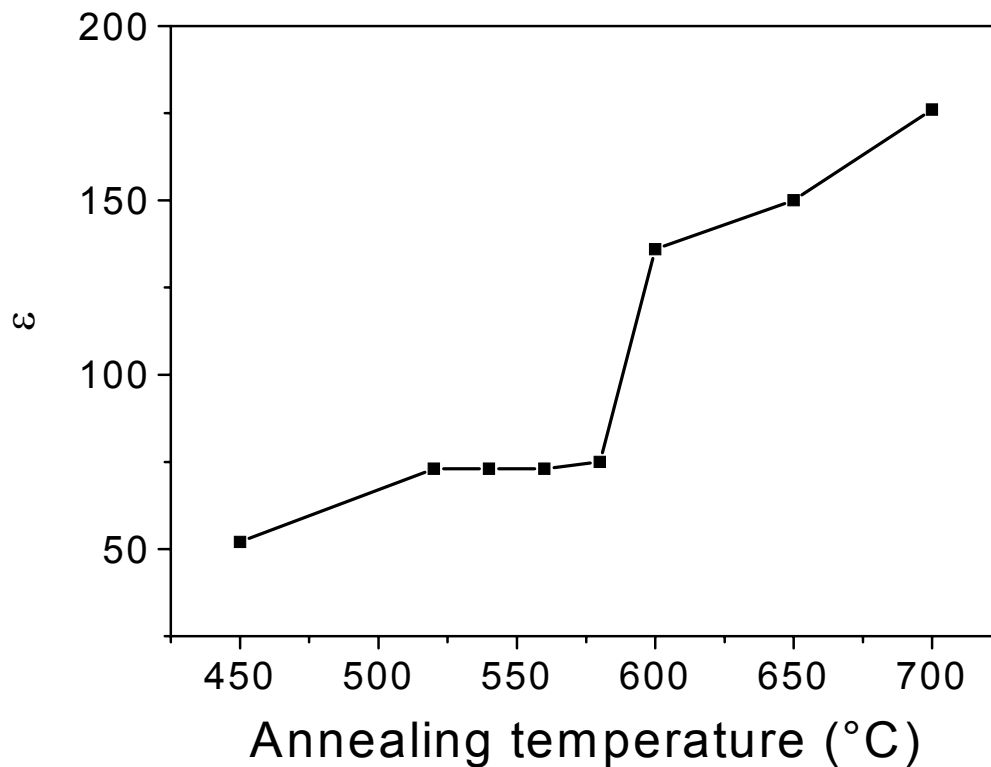


**Figure 5-27:** Dielectric properties of PZT (Pb: 21 at%) thin film at different annealing temperatures.

After annealing the PZT films at 520 °C the dielectric constant slightly increases to  $\epsilon = 70$ . At temperatures ranging from 520 °C to 570 °C the dielectric constant does not change. After annealing at 600 °C there is a significant increase in the dielectric constant, the value of  $\epsilon$  is 140. At the highest annealing temperature investigated the dielectric constant reaches the value of 180.

With the exception of the as-deposited films, for which  $\epsilon$  is independent of the applied voltage (figure 5-26), all annealed PZT films show a hysteretic response in  $\epsilon$ -E curves.

Figure 5-28 presents  $\epsilon$ -E characteristics of Ir/PZT/Ir capacitors annealed at temperatures ranging from 580 °C to 700 °C which have been calculated from C-V characteristics. The arrows indicate the direction of the plot. The butterfly shape of the curves confirms the ferroelectric nature of the film. The two maxima of the loop correspond to domain-switching voltages in forward and reverse directions where the polarization reversal takes place. The slight asymmetry in the  $\epsilon$ -E curve may be due to different electrode/ferroelectric interfaces.

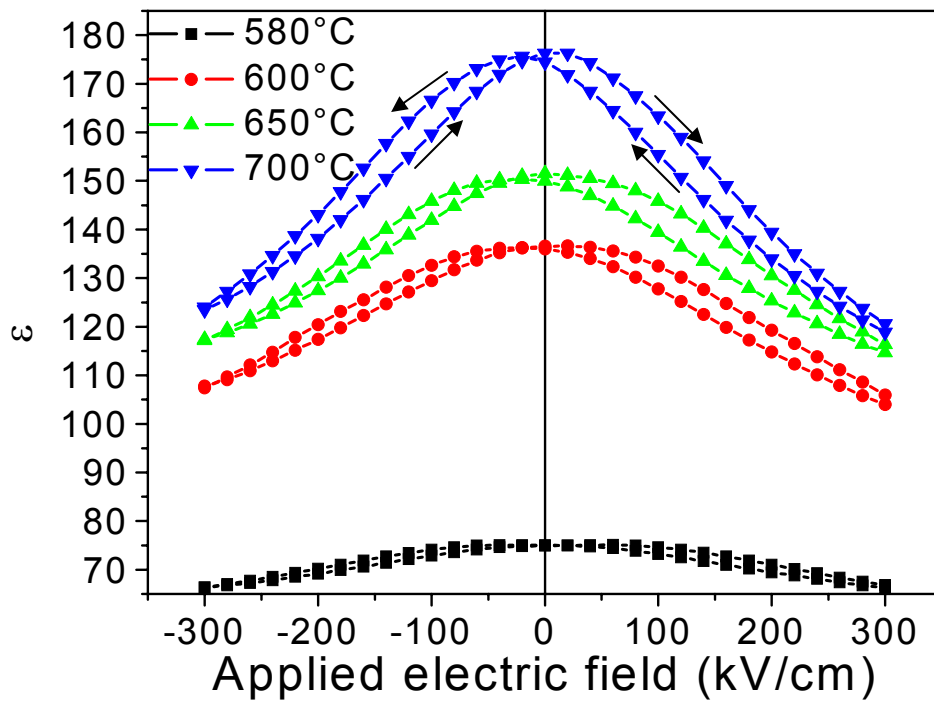


**Figure 5-28:** Dielectric constant vs. electric field of lead zirconate titanate (Pb: 21 at%) capacitors measured at 100 kHz in dependence on annealing temperature.

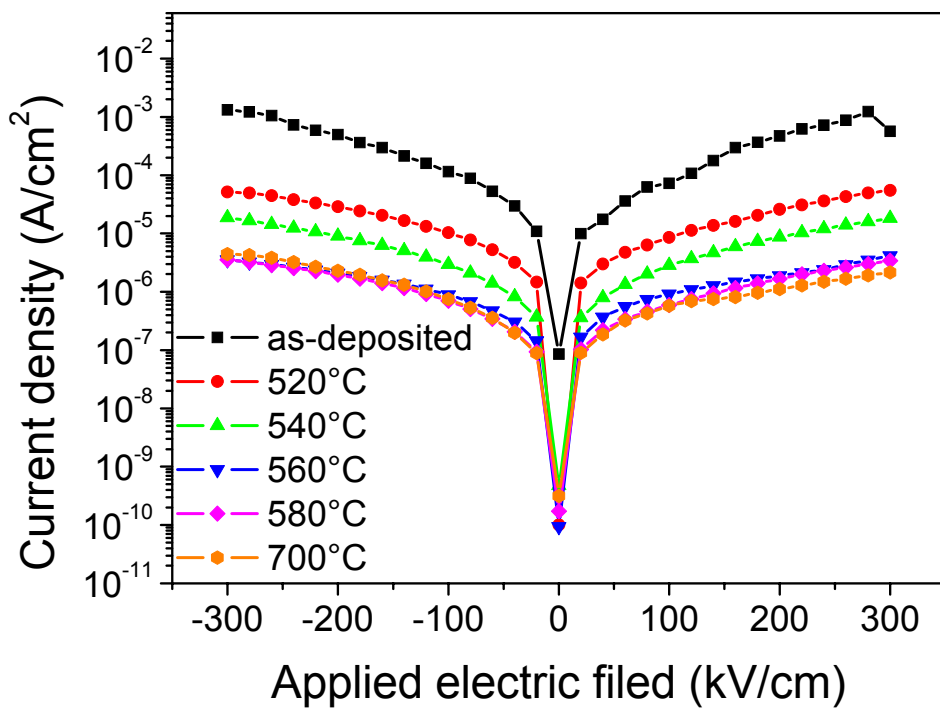


**Figure 5-29:** Leakage current density vs. electric field characteristics of PZT (Pb: 21 at%) capacitors annealed at different temperatures.

The leakage current behavior is another important parameter for device applications. Figure 5-29 shows leakage current density vs. electric field characteristics of PZT capacitors with 21 at% lead before and after annealing. As can be seen in figure 5-29 the leakage current density is depending on the annealing temperature. An as-deposited film has a high value of the leakage current density of about  $10^{-3}$  A/cm<sup>2</sup> at an applied field of 150 kV/cm. The high values of the leakage current can be understood by the presence of the additional PbO phase in as-deposited PZT films with 21 at% lead. It has been shown in section 5.1.2.2 that an annealing of such films at high temperatures can improve their structural properties. Annealed PZT films also exhibit an improvement of the electrical properties. A temperature treatment of the deposited layers decreases the value of the leakage currents. The leakage current density of films annealed at 560 °C is lower than  $10^{-6}$  A/cm<sup>2</sup> at an applied field of 150 kV/cm, which is quite satisfactory for device application (figure 5-29).

After annealing at 560 °C, the value of the leakage current density decreases from  $8 \cdot 10^{-3}$  A/cm<sup>2</sup> for as-deposited PZT films to  $10^{-6}$  A/cm<sup>2</sup>. The decrease of the leakage current in the annealed films can be due to the disappearance of the lead oxide phase and to an improvement of the crystalline structure of the films. Annealing at higher temperatures in the range from 600 to 700 °C does not show any change of the leakage current behavior. Therefore, the electrical properties of PZT films can be improved at a temperature as low as 560 °C.

#### 5.1.4 Summary

After annealing at 520 °C (110) oriented  $\text{Pb}_{1.05}(\text{Zr}_{0.52}\text{Ti}_{0.48})\text{O}_3$  thin films having good structural and electrical properties have been successfully fabricated on Ir/TiO<sub>2</sub>/SiO<sub>2</sub>/Si substrates. This film exhibits a remanent polarization and a coercitive field strength of 60 μC/cm<sup>2</sup> and 200 kV/cm, respectively, at an applied voltage of 3V. The dielectric constant of a PZT film with a lead content of 21 at% is 180. The leakage current density is lower than  $10^{-6}$  A/cm<sup>2</sup> at an applied electric field of 150 kV/cm. The good structural, dielectric, and ferroelectric properties of the films treated at a low annealing temperature of 520 °C promise to solve major problems of PZT integration into high density memory devices.

## 5.2 Strontium Bismuth Tantalate

The MOCVD process development has been carried out for various bismuth precursors. Their impact on composition and on structural and electrical properties of the grown strontium bismuth tantalate (SBT) films has been studied intensively. The one SBT layer of the composition  $\text{Sr}_{0.9}\text{Bi}_{2.2}\text{Ta}_2\text{O}_9$  has been chosen to be the most suitable for applications in FRAM devices.

### 5.2.1 Deposition Kinetics

On the way to develop a MOCVD process for strontium bismuth tantalate, at first the MOCVD processes for Bi and Sr-Ta precursors have been investigated separately. Then SBT films have been grown. Figures 5-30 and 5-31 show the dependencies of the growth rates of bismuth oxide, strontium tantalate and SBT at different reactor temperatures for a reactor pressure of 0.35 mbar.

In the case of triphenylbismuth (figure 5-30a) and triallylbismuth (figure 5-30b), the deposition rates of the bismuth oxide thin films are low, about 10 nm/h, even at elevated temperatures. Therefore, they can be considered to be almost not dependant on the deposition temperature, see figure 5-30. On the contrary, the growth rate of strontium tantalate films depends strongly on the substrate temperature. Three characteristic regimes can be determined for the Sr-Ta precursor. The first one is observed at low temperatures (350 – 450 °C). In this temperature range, the surface is not sufficiently activated; the deposition rate is rather low (about 12 nm/h) and slowly increases at elevated temperatures. In the second temperature range (450 – 550 °C), the process is reaction rate limited. The activation energy has been calculated in this temperature range and equals 45 kJ/mol (0.466 eV). Above 550 °C, the deposition rate saturates at 30 nm/h and a mass transport rate limited regime can be observed.

The deposition rates of the SBT films grown by using triallylbismuth and triphenylbismuth are very low and range from 3 to 11 nm/h (figure 5-30a) and 5 to 8 nm/h (figure 5-30b), respectively. The growth rate vs. deposition temperature behavior is similar to the bismuth oxide deposition that slightly increases with increasing substrate temperature. But the deposition rate of the SBT film is lower than deposition rates of the single metal oxides.

Due to these results these bismuth precursors have not considered for further work. The SBT growth experiments have been continued with the bismuth alkyl precursor tributylbismuth.

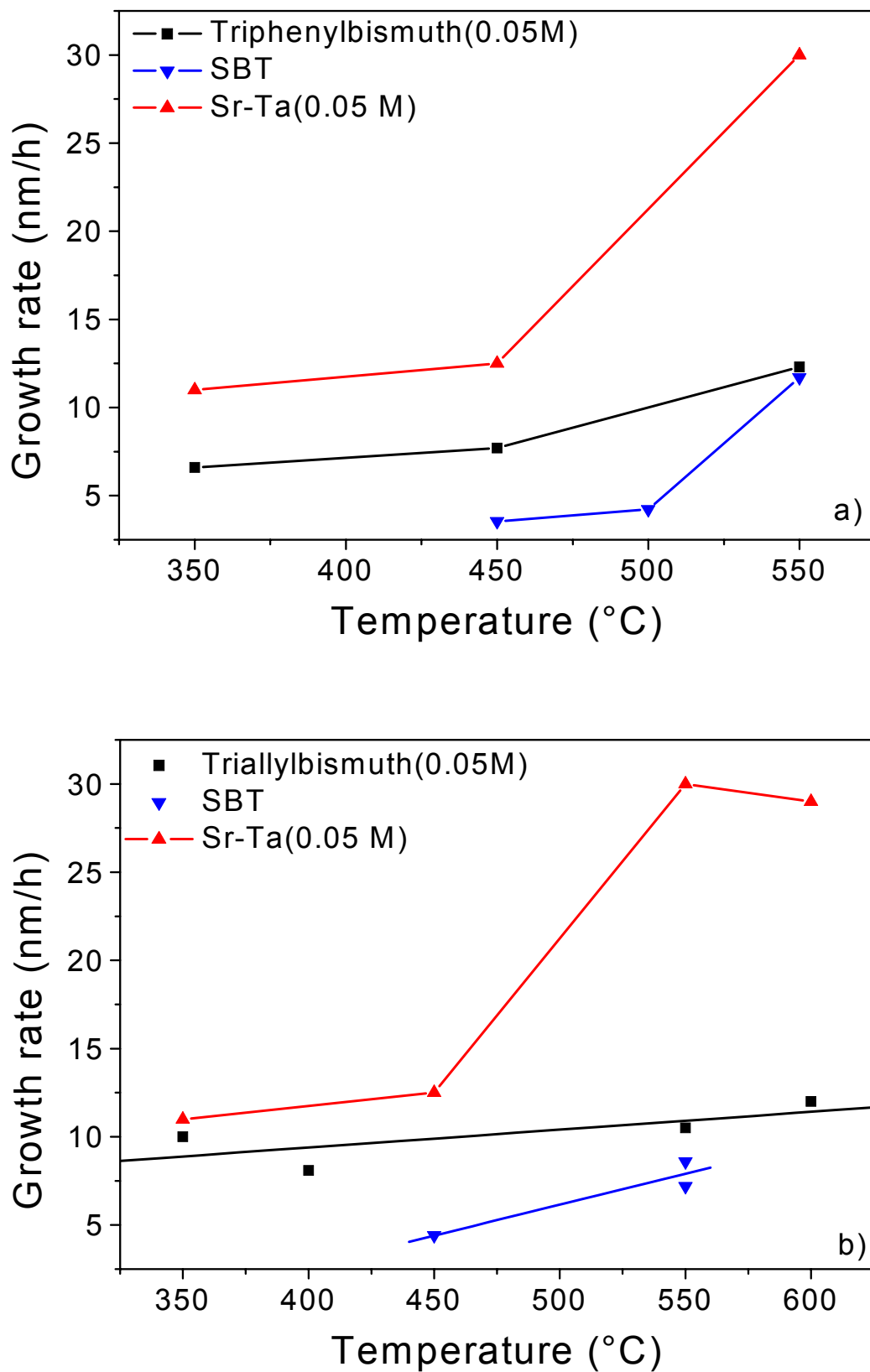


**Figure 5-30:** Growth rate of  $\text{Bi}_2\text{O}_3$ ,  $\text{SrTa}_2\text{O}_6$ , and SBT thin films as a function of the substrate temperature at 0.35 mbar pressure: a) for triphenylbismuth and b) for triallylbismuth.

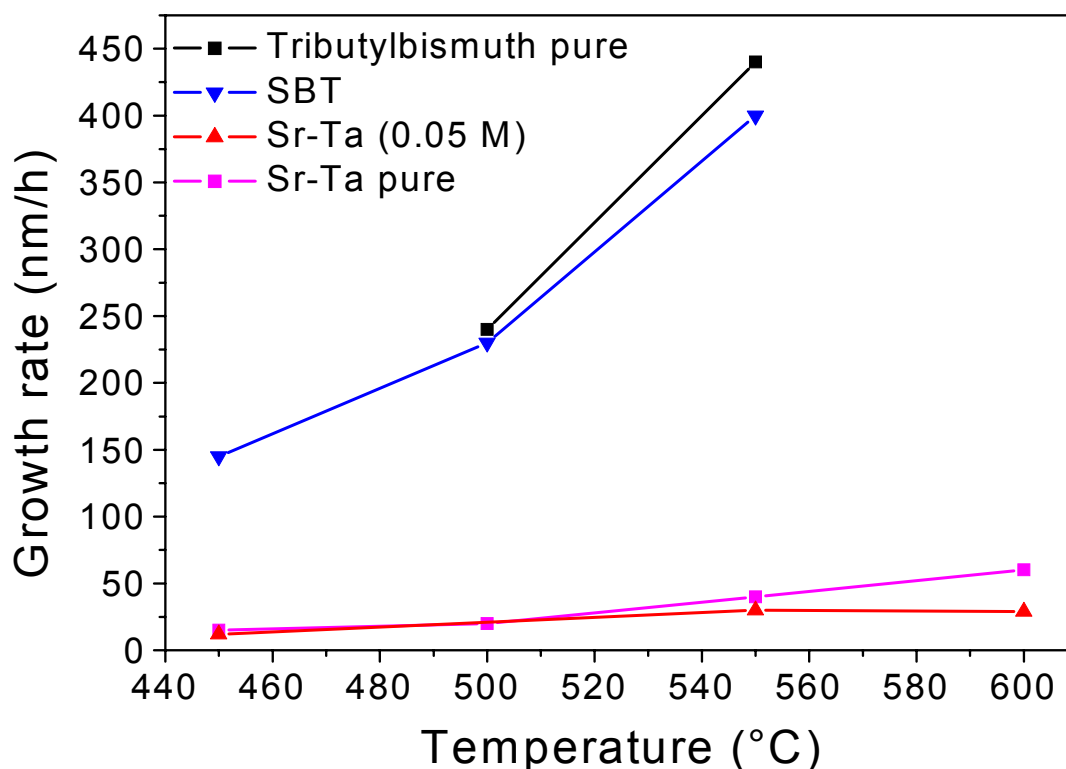


**Figure 5-31:** Growth rate of  $\text{Bi}_2\text{O}_3$ ,  $\text{SrTa}_2\text{O}_6$ , and SBT thin films as a function of the substrate temperature at 0.35 mbar pressure for tributylbismuth.

Tributylbismuth can be used in highly concentrated or pure form because of its higher stability. Contrary to triallylbismuth, the influence of the temperature on the growth rate is much stronger. As can be seen in figure 5-31, deposition rate of bismuth oxide from tributylbismuth varies from about 200 nm/h at a temperature of 500 °C up to 400 nm/h at 550 °C. The growth rate of SBT is lower than the growth rate of the bismuth oxide as well as for triphenyl- and triallylbismuth.

The growth rate of the pure Sr-Ta precursor is about the same as of the diluted Sr-Ta precursor, see figure 5-31. A difference between the pure and the diluted precursor is only evident at elevated temperatures (550 – 600 °C).

Figure 5-32 shows the dependency of the deposition rates of strontium bismuth tantalate and strontium tantalate films on the work pressure in the reactor. Triallylbismuth has been used as a bismuth source.

The growth rates of SBT as well as of  $\text{SrTa}_2\text{O}_6$  thin films significantly depend on the deposition pressure. At 450 °C, the growth rate increases from 5 to 15 nm/h and from 12 to 35 nm/h for SBT and Sr-Ta precursors, respectively (figure 5-32a). The deposition rate of SBT film rises from 7 to 45 nm/h at the temperature of 550 °C by increasing the pressure from

0.35 to 3.5 mbar (figure 5-32b). Figure 5-32b also shows that the growth rate of SBT is lower than the growth rate of strontium tantalate if triallylbismuth has been used as a bismuth source.

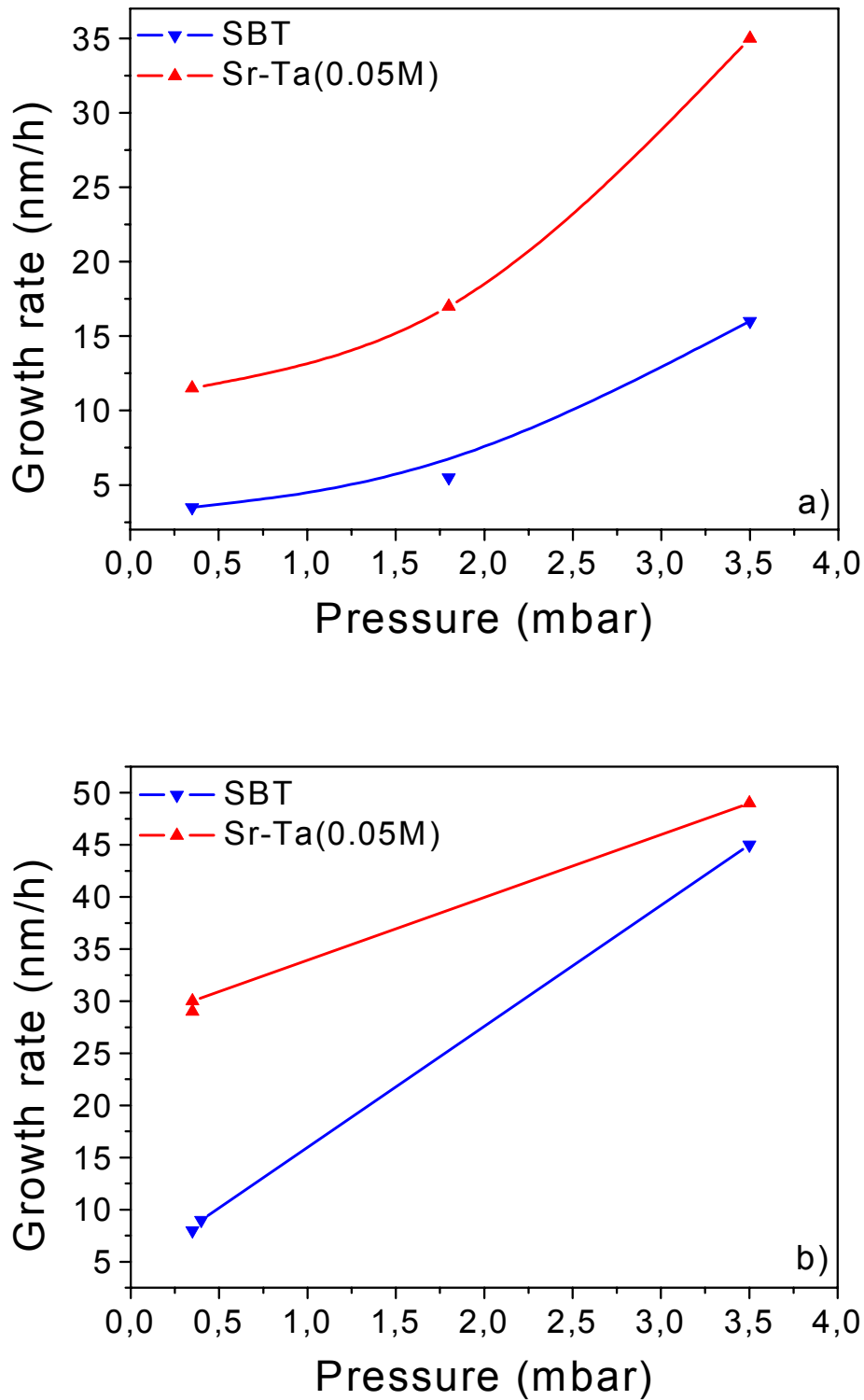


**Figure 5-32:** Growth rate of strontium tantalate and SBT thin films as a function of the pressure at substrate temperature of a) 450 °C and b) 550 °C.

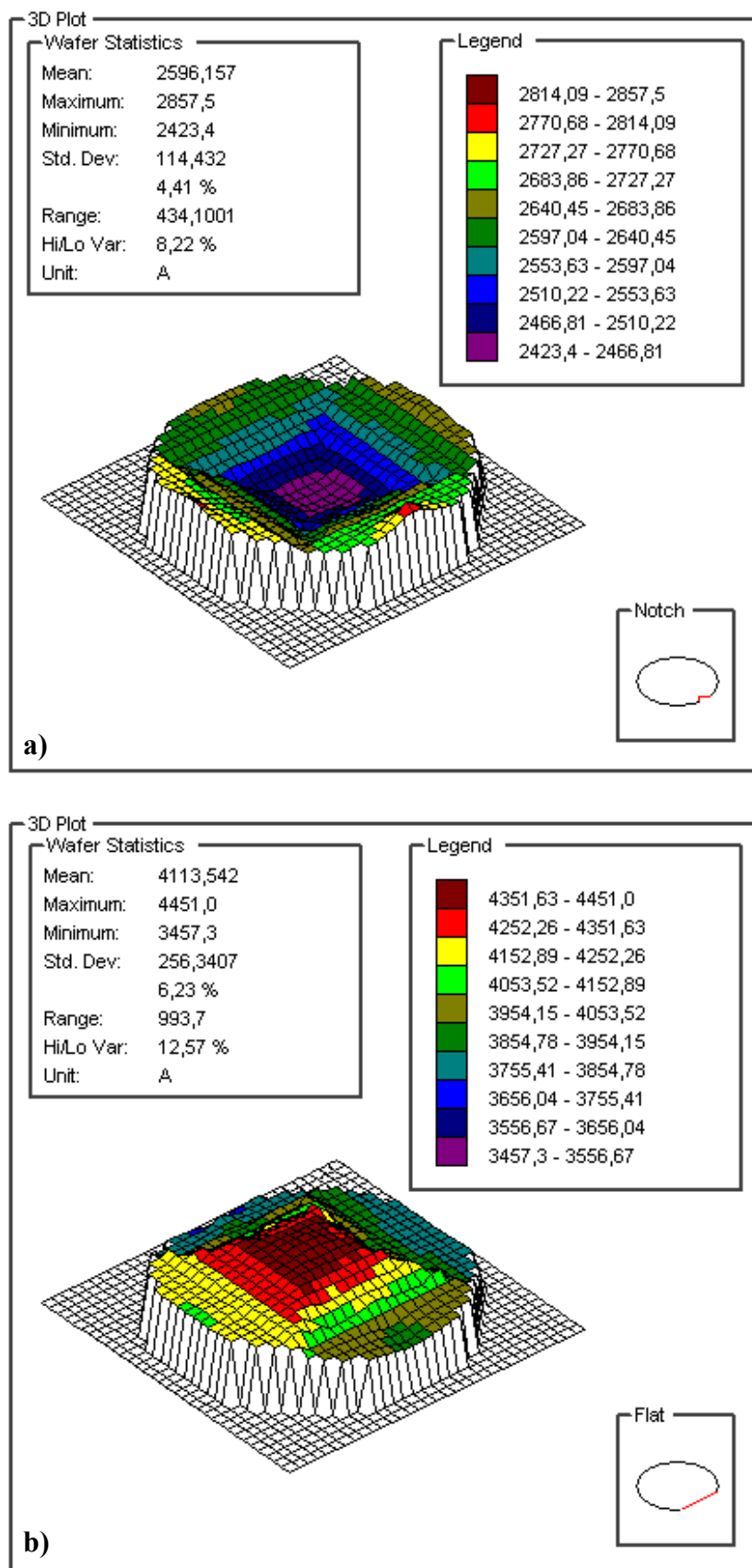


**Figure 5-33:** SBT film thickness as a function of the position on the wafer. The flow rate ratio of the Sr-Ta (0.1M) precursor to tributylbismuth (0.1M) is 1:1 in a) and 1:2 in b).

However, another pressure related effect can be observed. Indeed, the deposition rate is enhanced by increasing the pressure, but the uniformity of the film thickness over the entire wafer is lowered. An increase of the substrate temperature improves the film uniformity only at reduced (0.35 mbar) pressure. The standard deviation of the films thickness decreases from 7% at 350 °C to 3 – 4% at 550 °C.

At higher pressure, the film thickness distribution is less homogeneous and the standard deviation of the film thickness exceeds 40 %. In this case, there is no correlation between the uniformity of the film thickness and the substrate temperature.

The homogeneity of SBT thin films also significant depends on the ratio of the introduced precursors. A negligible excess of tributylbismuth is necessary to obtain thin SBT film with good homogeneity. If the ratio of the introduced precursors is 1:1, the surface of the deposited film has a concave form and the standard deviation of the film thickness is about 5% (figure 5-33a). If the flow rate of tributylbismuth is increased, and its ratio to the Sr-Ta precursor is 2:1, a change of the film thickness distribution from a valley shaped to a hill shaped form is observed (figure 5-33b). After an improvement of the injection parameters, the value of the standard deviation of the film thickness is below 2 %. This optimized film thickness distribution is shown in figure 5-34.

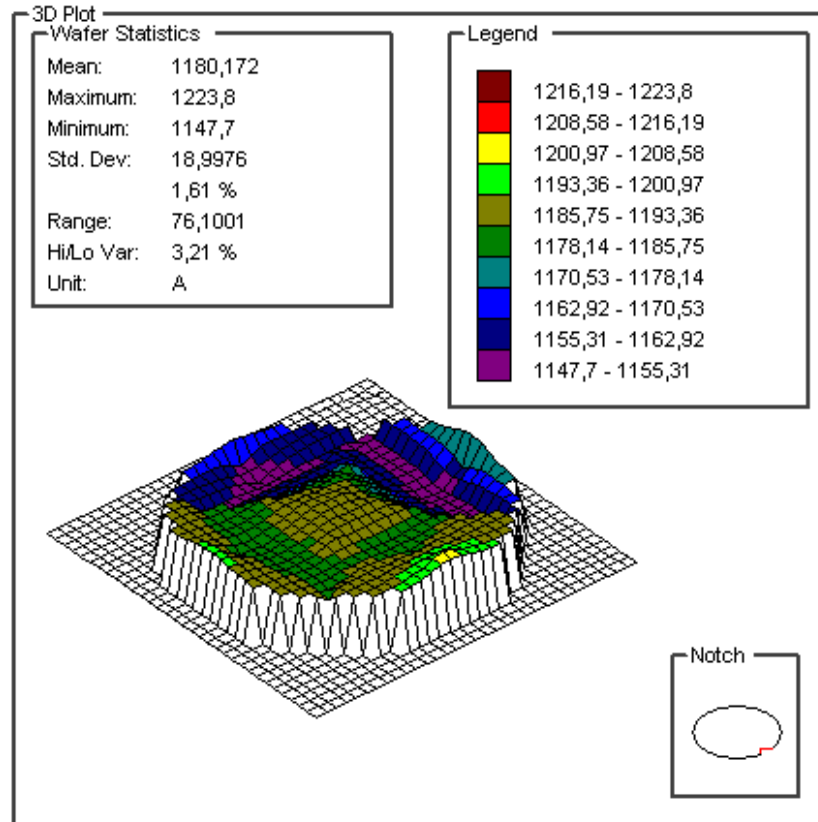


**Figure 5-34:** SBT film thickness as a function of the position on the wafer (150 mm diameter) after optimization of the injection conditions.

### 5.2.2 Chemical Composition

In order to obtain further information about the chemical state of the deposited films, X-ray photoelectron spectroscopy (XPS) has been carried out. For detailed information about this method and applied measurement conditions see section 4.6.1.2. For the XPS analysis, SBT-2 and SBT-3 structures (compare section 4.3) have been prepared.

Figure 5-35 shows the elemental composition of the SBT-2 thin film deposited using triallylbismuth as bismuth precursor. Due to a low thickness of this film, the underlying platinum electrode can be observed through the SBT layer. It has a concentration of about 2 at% in the XPS spectrum. The surface concentrations of the other elements are as follows: Bi – 3 at%, C – 32 at%, Ta – 14 at%, Sr – 8 at%, and O – 41 at%. No more carbon can be observed after an initial  $\text{Ar}^+$  ion bombardment. This means that the substrate temperature and the oxygen content have been high enough for growing carbon-free films.

The other components show a different behavior with increased sputter time. At first, the concentration of Sr, O, and Ta atoms increases, related to the disappearing of carbon. After that, the content of Sr, Ta and O decreases, while the Pt concentration strongly increases with sputtering time and depth.

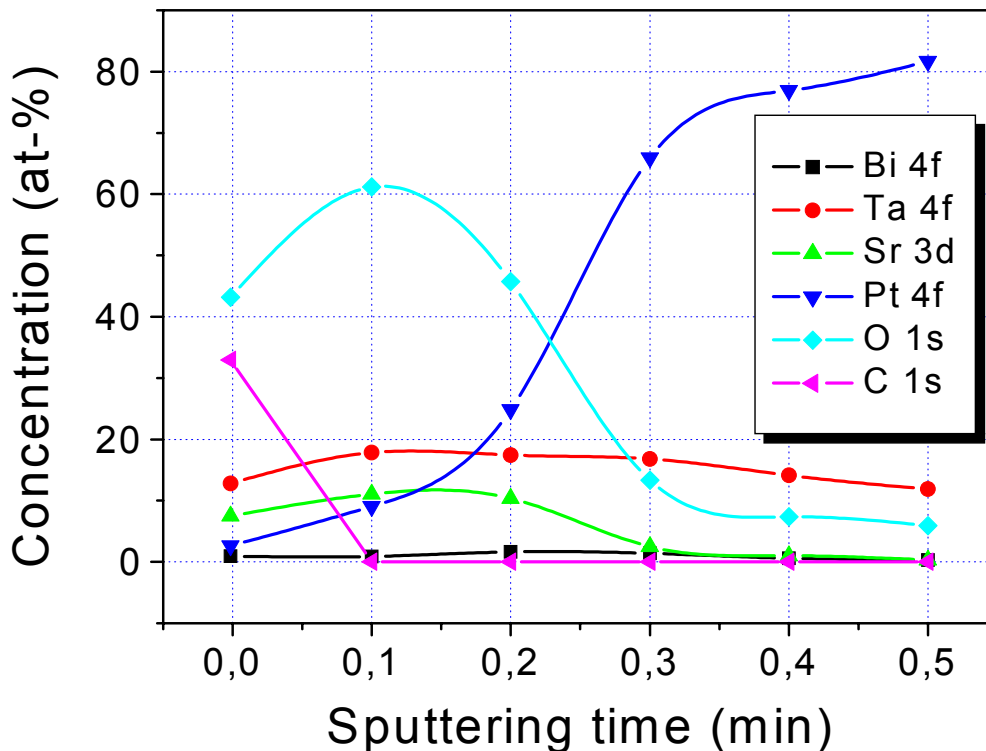


**Figure 5-35:** Elemental composition of SBT-2 thin film (measured by XPS) as a function of  $\text{Ar}^+$  ion sputtering time.

The Ta concentration seems to be almost not affected by the strong increase of the Pt concentration, while the concentration of Sr, O and Bi decrease for sputtering times higher than 0,3 min in figure 5-35. One possible explanation for this high Ta concentration (about 10 at%) in the Pt can be that the sputtering yield of Ta is three times lower than for the other elements and, consequently, Ta atoms are knocked on the Pt film. XPS measurements of SBT films deposited on uncoated silicon wafers (without a Pt electrode layer) also support this observation. A Ta concentration of about 9 at% has been detected in the silicon wafer volume while diffusion can be neglected at the process temperature of 450 °C [112].

The XPS spectra of SBT films grown by using triallylbismuth show a lack of bismuth, i.e. the ratio of the Bi atom concentration to the Ta atom concentration in SBT-2 (Bi/Ta) was only 0.25 ( $\text{SrBi}_{0.5}\text{Ta}_2\text{O}_9$ ), even though the concentration of the Bi precursor (0.1 mol/l) was two times higher than the concentration of the Sr-Ta precursor (0.05 mol/l) (for equal flow rates).

The content of Bi in the SBT thin films depends strongly on the oxygen concentration in the deposition gas mixture. When no oxygen is added during thin film growth, the surface concentration of Bi is lower than 1 at%. The ratio of the bismuth to tantalum atom concentration in the layer has been about 0.05.

According to M.A. Cameron's model proposed for zirconium tetrabutoxide, the surface reaction may be partially poisoned by carbon [82]. After pyrolytic decomposition of the precursor at the surface adsorbed carbon atoms are not able to desorb at the chosen growth temperatures, and block adsorption sites lowering the bismuth oxide growth rate.

In the case of tributylbismuth, the Bi/Ta ratio in the SBT film has been varied from 1.0 to 1.3 ( $\text{Sr}_{0.9}\text{Bi}_{2-2.6}\text{Ta}_2\text{O}_9$ ). The XPS peaks of Sr, Bi, Ta, Pt, O and C after different  $\text{Ar}^+$  ion sputtering times are presented in figure 5-36. The energetic positions of the Ta  $4f_{5/2}$  (27.9 eV), Ta  $4f_{7/2}$  (26.6 eV), Sr  $3d_{3/2}$  (135.1 eV), Sr  $3d_{5/2}$  (133.5 eV), Bi  $4f_{5/2}$  (159.1 eV), and Bi  $4f_{7/2}$  (164.4 eV) peaks indicate that these elements are in the oxidized state.

Different bond characteristics of Ta, Sr, and Bi are observed after  $\text{Ar}^+$  ion bombardment (see figure 5-36). The peaks of Sr, Ta, and Bi shift to lower energies. This means that the chemical state of Sr, Ta, and Bi changes from the oxide state to the metallic. This is due to a preferential sputtering of oxygen atoms [113].

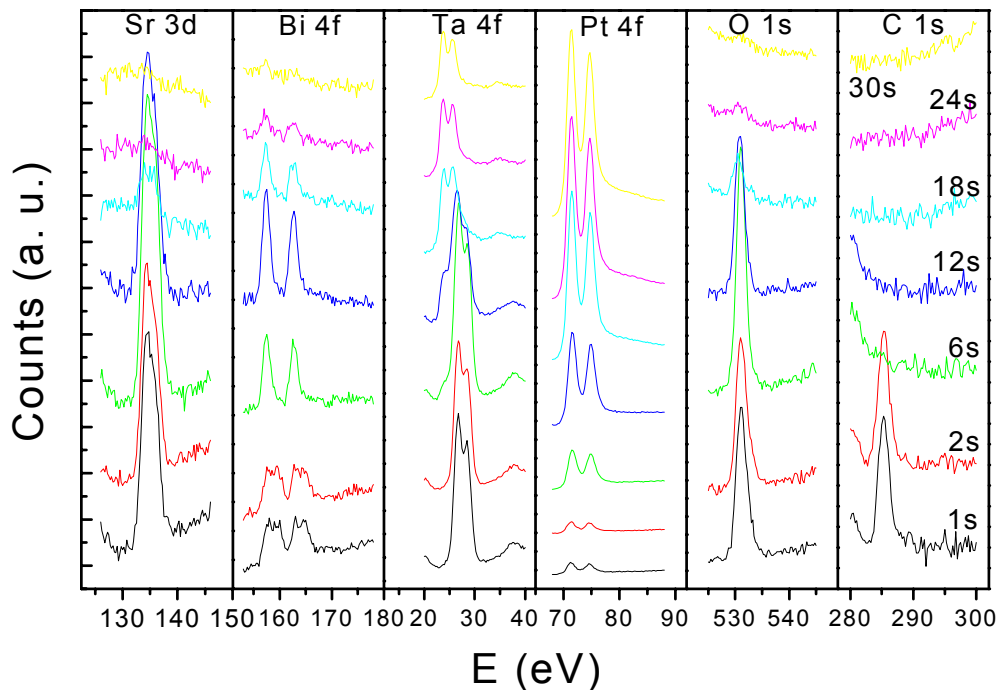


**Figure 5-36:** XPS peaks of Sr 3d, Bi 4f, Ta 4f, Pt 4f, O 1s, and C 1s after different Ar<sup>+</sup> ion sputtering times.

### 5.2.3 Structural Characterization

Three phases, the fluorite, the pyrochlore and the bismuth layer-structured phase are known to exist in the strontium-bismuth-tantalum oxygen thin film system, but only the bismuth layer-structured SBT phase is known to have large ferroelectricity [114]. The crystallization route of SBT has been reported by several groups [115-118]. It is well known that before crystallization of the ferroelectric Aurivillius phase a metastable and non-ferroelectric fluorite phase is obtained [117]. This crystallographic phase transformation from the fluorite to the Aurivillius phase starts at about 650 °C and is accompanied by a morphological change via a coexistence of both phases.

Figure 5-37 shows X-ray diffraction patterns of SBT/Ir/TiO<sub>2</sub>/SiO<sub>2</sub>/Si structures before and after post-annealing processes. The films have been annealed in a conventional furnace at temperatures ranging from 700 °C to 800 °C under oxygen ambient for 15 min. The obtained results show that the crystalline phase of the SBT layers is highly affected by post-annealing.

For the as-deposited state with a deposition temperature of 470 °C, four peaks marked by asterisks are observed together with the substrate peaks (marked by filled circles). Cho *et al.* attributed the two peaks at 33° and 56.05° to SBT (200) and SBT (400), respectively [119].

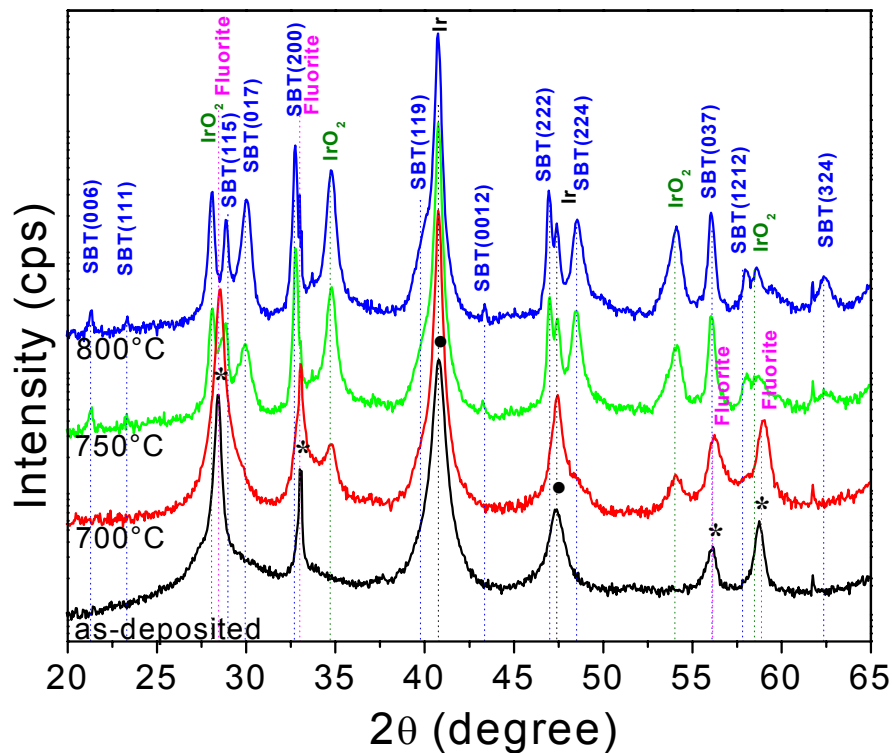


**Figure 5-37:** XRD pattern of a SBT thin film deposited at 470°C; as deposited - fluorite phase → annealed at 750°C - perovskite phase.

However, it was found out by other researchers [120,121] that Cho *et al.* [119] have been fallen into an error in the interpretation of the XRD data. Hyun *et al.* suggested that the as-deposited SBT films consist of a fluorite-like phase [121]. Correspondence of the peaks at 33° and 56.05° to the fluorite phase was also noted by Koiwa *et al.* [122], Lee *et al.* [115], Nukaga *et al.* [114] etc. These authors attribute the formation of the fluorite phase to an excess of bismuth in the grown films. The lack of the diffraction peak at 29.2° indicates that the as-deposited film does not have a pyrochlore structure. Therefore, as-grown SBT thin films show only the crystalline fluorite phase.

After annealing of the obtained structures at 700 °C two strong peaks at  $2\theta=34.7^\circ$  and  $2\theta=54.02^\circ$  appear. These two peaks indicate an oxidation of the bottom electrode and a formation of crystalline iridium oxide. A small change of the peak shapes observed at  $2\theta=29.7^\circ$ ,  $32.8^\circ$ ,  $48.7^\circ$ , and  $57.75^\circ$  indicates the beginning of the crystallization of the SBT film to the polycrystalline perovskite structure. A coexistence of the fluorite and the perovskite SBT phases in the films annealed at 700 °C has also been observed by other researchers [114,115,122].

As can be seen in figure 5-37, SBT films annealed at 750 °C are completely crystallized in the perovskite phase. It is not possible to detect the presence of the fluorite phase by XRD. An increased height of the iridium oxide peaks and the appearance of new peaks at  $2\theta=28.5^\circ$  and  $58.5^\circ$  correspond to a promoted growth of iridium oxide during annealing of the prepared structures at 750 °C.

Annealing at 800 °C does not result in a remarkable change in the XRD profiles of the films in comparison to those annealed at 750 °C. Therefore, it can be concluded that SBT films deposited by MOCVD are completely crystallized in the ferroelectric Aurivillius phase after annealing at temperatures at 750 °C. The absence of the pyrochlore peak after annealing at 800 °C indicates that bismuth has not been lost even after the high temperature treatment. A decrease of the bismuth content and a change from the ferroelectric perovskite to the paraelectric pyrochlore structure have been reported by Takahashi *et al.* [123] for SBT films prepared by the metalorganic decomposition method as they have increased the annealing temperature. Also, the formation of the pyrochlore phase, which is a Bi-deficient phase, has been identified by Jung *et al.* [116] for films annealed at 730 °C for times longer than 40 min.

Figure 5-38 shows the morphology of SBT films annealed at a temperature of 750 °C. The Aurivillius phase consists of large grains. In contrast, the fluorite phase is always represented by very small and circular shaped grains [117]. In the XRD pattern of the as-deposited film the fluorite peaks are higher and broader.

Corresponding to Scherer's formula the broad peaks are related to a very fine crystallite grain size:

$$D_{hkl} = \frac{0.9\lambda}{\beta_{hkl} \cos(\theta_{hkl})}, \quad (2)$$

where  $\lambda$  is the wavelength of the incident radiation,  $\beta_{hkl}$  is the full width at the half maximum of the peak in radians, and  $\theta_{hkl}$  is the Bragg angle.

The grain size has been estimated from the widths at half maximum of the peaks by Scherer's formula. The peaks (115) and (200) of the XRD pattern of the films have been used to calculate the average grain size. The average grain size of SBT films increases with increasing annealing temperature and is approximately 175 nm for SBT thin films annealed at 800 °C. Calculated grain sizes for films of this work agree well with SEM measurements and are close to the results presented by Nukaga *et al.* [118] and Yang *et al.* [124] for well crystallized SBT films.

SEM investigations show also that the grain sizes of SBT films decrease with lower film thickness and deposition temperature.

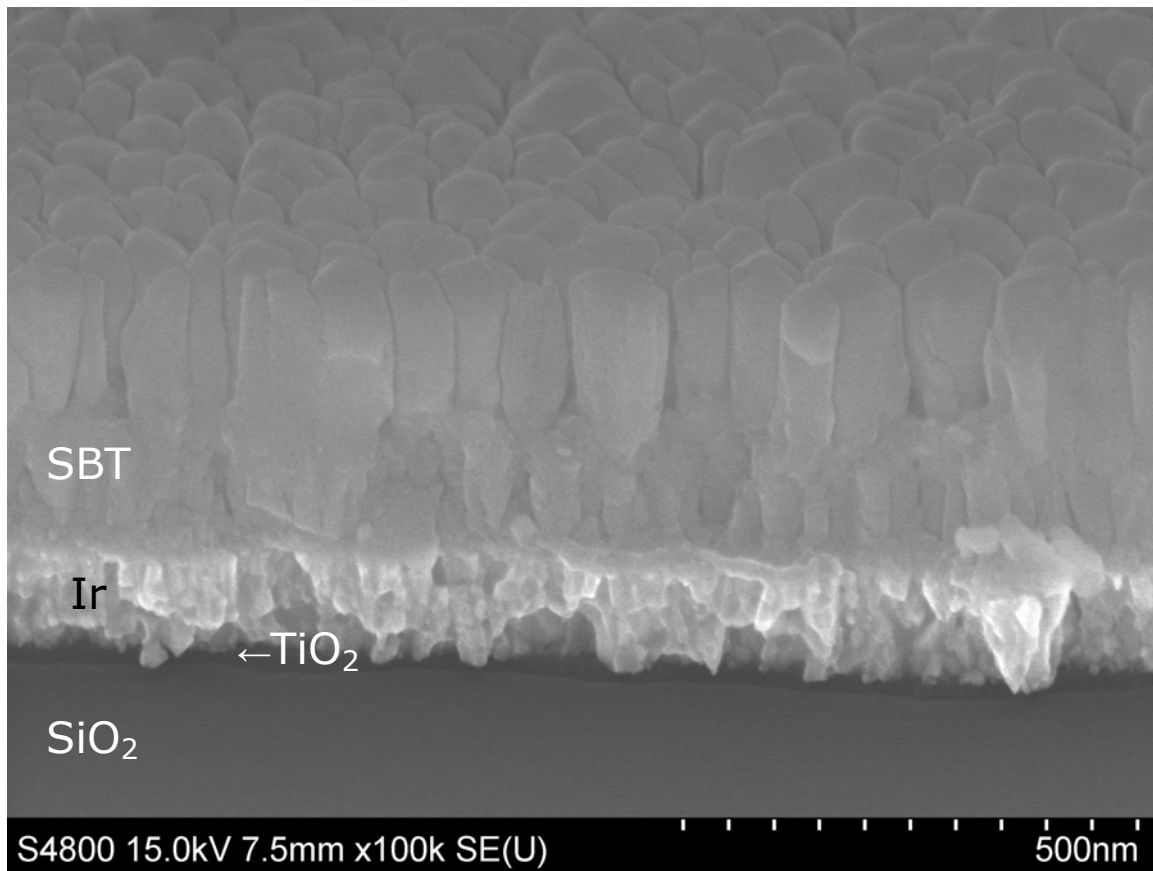
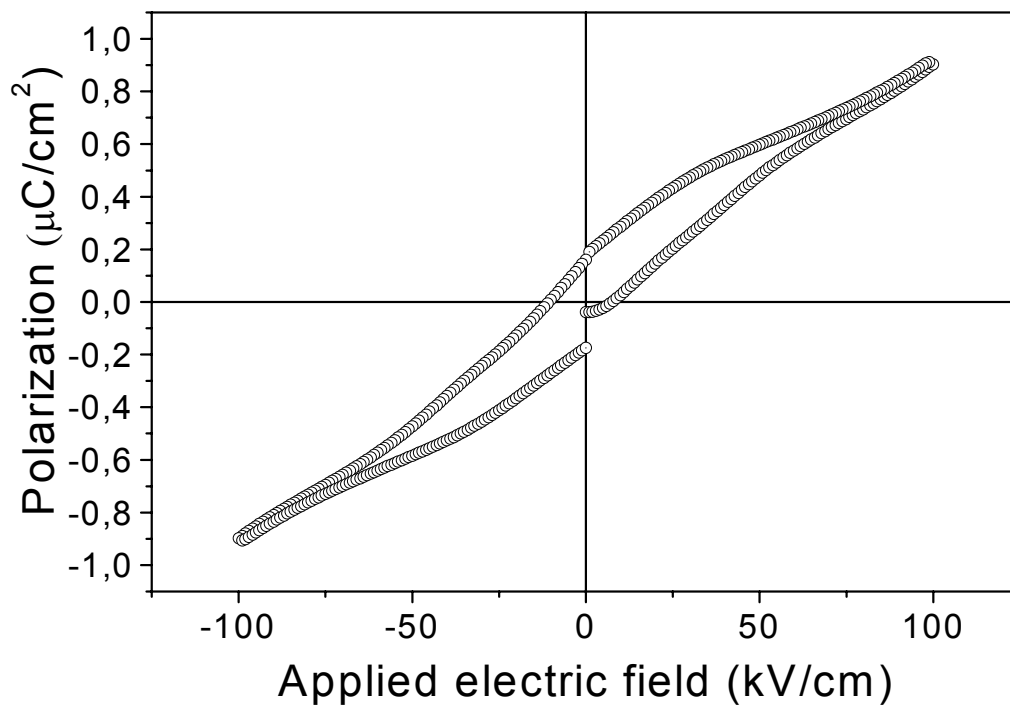


**Figure 5-38:** SEM picture of a SBT thin film grown on a Ir/TiO<sub>2</sub>/SiO<sub>2</sub> bottom electrode and annealed at 750 °C.

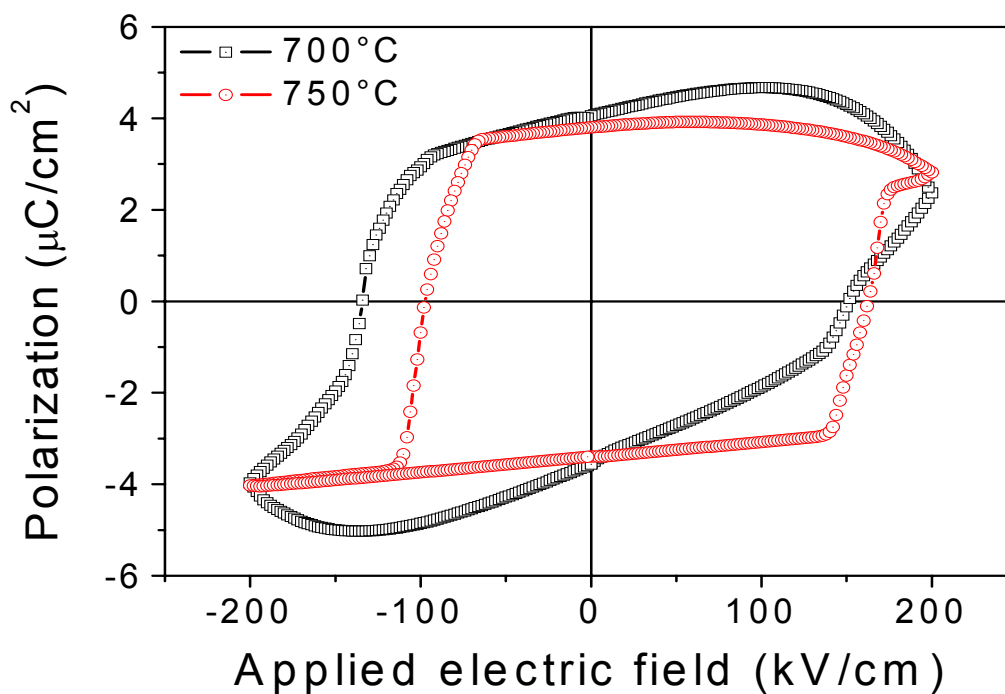
#### 5.2.4 Electrical Characterization

Figure 5-39 shows a typical hysteresis curve of a SBT film deposited with triallylbismuth as Bi precursor. With this precursor the SBT films have a deficit of Bi. As can be seen in the figure 5-39 the loop does not saturate. An annealing of such structures does not result in any improvement of the electrical properties. The poor ferroelectric properties of the SBT films grown by using triallylbismuth can be easily explained by the deficiency of bismuth in the layer. Jung *et al.* [116] and Koiwa *et al.* [125] have noted in their works that the formation of the ferroelectric Aurivillius phase in SBT is only possible in the case of a small excess of bismuth. After annealing at high temperatures the fluorite phase changes to the non-ferroelectric pyrochlore phase if the concentration of bismuth is too low [117,123].

In figure 5-40 a typical hysteresis curve of a SBT film which has been grown with tributylbismuth is presented. The film composition is Sr<sub>0.9</sub>Bi<sub>2.2</sub>Ta<sub>2</sub>O<sub>9</sub>.



**Figure 5-39:** Typical hysteresis loop of SBT films (Bi/Ta ratio – 0.4) deposited from triallylbismuth and annealed at 750 °C temperature in air.



**Figure 5-40:** Hysteresis loops of SBT films deposited from tributylbismuth and annealed at different temperatures in an oxygen containing ambient.

These ferroelectric hysteresis loops of figure 5-40 are obtained for samples which have been annealed at 700 °C and 750 °C. The hysteresis loop of the SBT film annealed at 750 °C is well saturated; the values of the remanent polarization  $2P_r$  and of the coercive field strength are  $7 \mu\text{C}/\text{cm}^2$  and 100 kV/cm, respectively. Obtained results are close to results presented by Nukaga *et al.* [118] for SBT films with a Bi/Ta ratio about 1.2. The slight asymmetry in the P–E curve may be due to different electrode/ferroelectric interfaces.

SBT thin films annealed at 750 °C also exhibit good fatigue properties. Figure 5-41 shows remanent polarization versus switching cycles in a logarithmic scale. Fatigue is found to be about 4% after  $10^9$  cycles.

The oxygen vacancy ordering mechanism which is proposed in this work for perovskite titanates such as PZT (see section 5.1.3.1) is inoperative in Aurivillius layer structures such as  $\text{SrBi}_2\text{Ta}_2\text{O}_9$  (SBT) since the oxygen vacancies in a such system prefer sites in the  $\text{Bi}_2\text{O}_2$  planes. Thus their impact on the polarization is negligible, and does not take place within the  $\text{SrTaO}_3$  octahedra which control the ferroelectric polarization switching of the Ta–O bonds. This is the primary reason why SBT films do not fatigue [126].

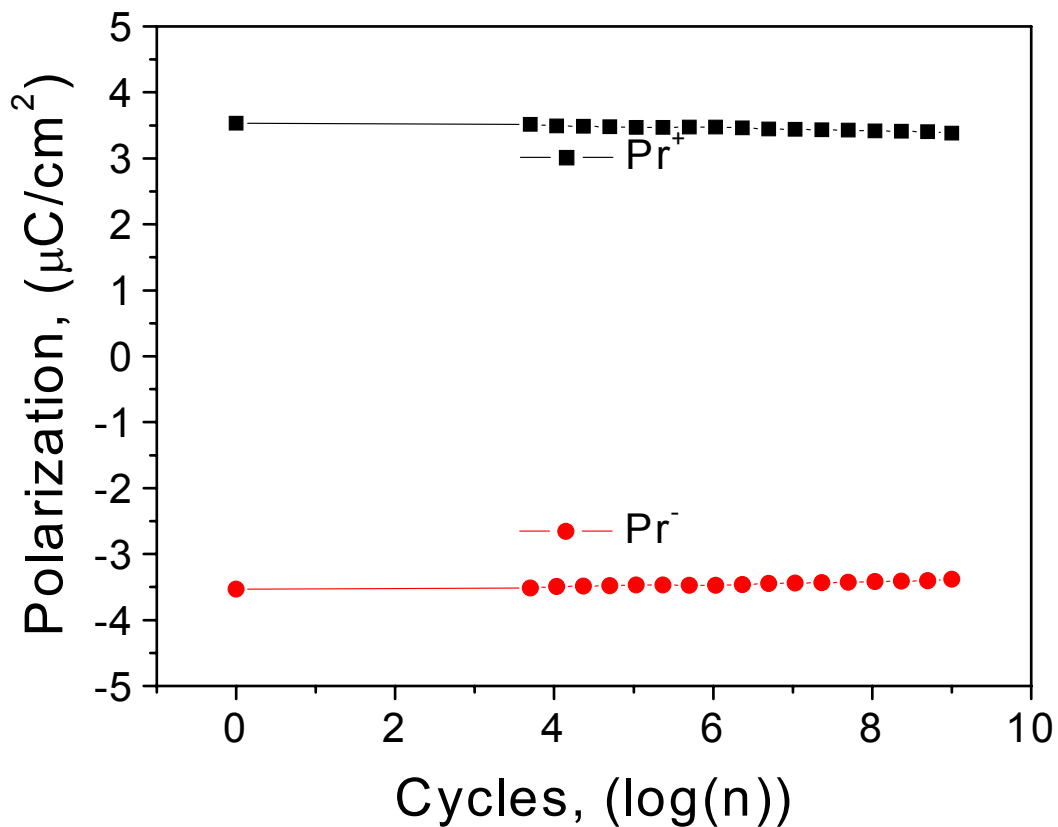


**Figure 5-41:** Fatigue characteristic of a SBT film annealed at 750 °C.

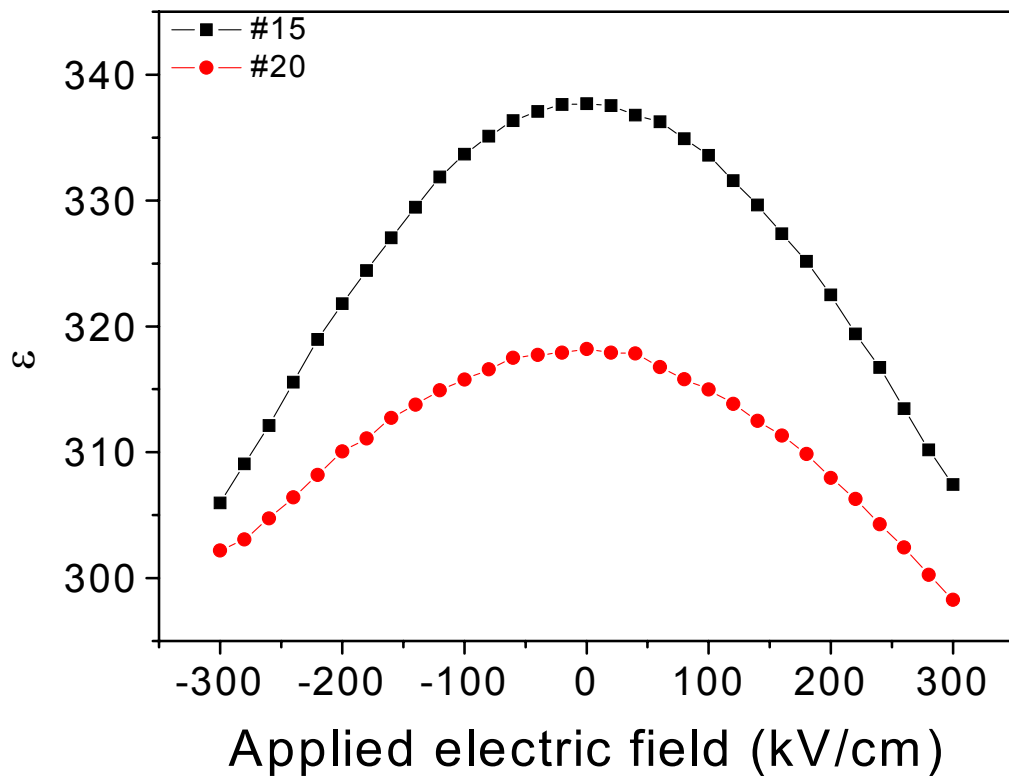


**Figure 5-42:** Dielectric constant of SBT films annealed at 800°C versus the applied voltage, #15 – contact in the center of the chip, #20 – contact in the corner of the chip.

Figure 5-42 shows the dielectric response of Ir/SrBi<sub>2</sub>Ta<sub>2</sub>O<sub>9</sub>/Ir capacitors. The dielectric properties have been measured at a frequency of 100 kHz (for detailed measurement conditions see section 4.6.2). The dielectric constant of SBT thin films is in the range of 300 to 335. These values are found to be close to those reported by Li *et al.* [127] for SrBi<sub>2</sub>Ta<sub>2</sub>O<sub>9</sub> thin films with an excess concentration of bismuth of about 15-25%.

The leakage current of the high  $\epsilon$  oxide materials is a limiting factor for DRAM memory applications as the stored charge can leak through a capacitor due to excessive leakage current making the binary state unrecognizable. The leakage current behavior of SrBi<sub>2</sub>Ta<sub>2</sub>O<sub>9</sub> thin films which also can find an application as high  $\epsilon$  materials has been analyzed by applying dc voltages with a step width of 0.2 V and a measurement time of 30 ms. A typical current density vs. field strength curve of a Sr<sub>0.9</sub>Bi<sub>2.2</sub>Ta<sub>2</sub>O<sub>9</sub> film annealed at 750 °C is presented in figure 5-43. The leakage current density of the films is lower than 10<sup>-6</sup> A/cm<sup>2</sup> up to an applied electric field of 200 kV/cm. The leakage current behavior is similar to those observed by Koiwa *et al.* in their sol-gel derived SBT films [125] and by Li *et al.* in SBT films deposited by metalorganic decomposition technique [127].

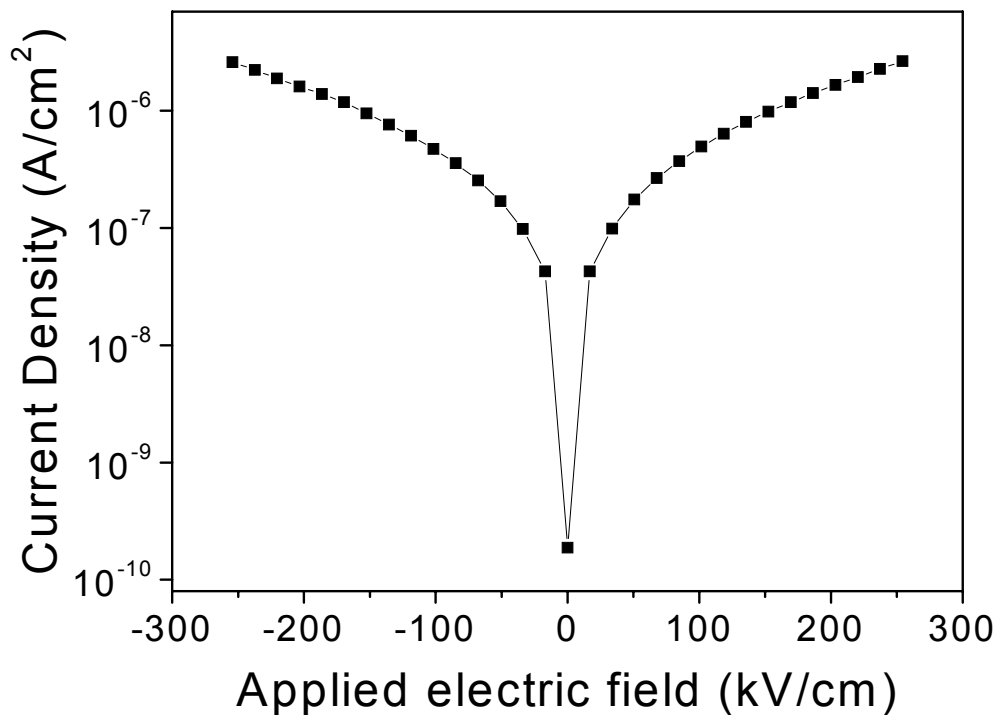


**Figure 5-43.** Leakage current density of  $\text{Sr}_{0.9}\text{Bi}_{2.2}\text{Ta}_2\text{O}_9$  thin films annealed at 750 °C.

### 5.2.5 Summary

The right choice of the bismuth precursors is very important for the fabrication of SBT thin films by MOCVD. The low growth rates of bismuth oxide from triallylbismuth and triphenylbismuth show that these both precursors are not favourable. Stoichiometric SBT-films, however, can be obtained by using tributylbismuth.

As-deposited SBT-films are polycrystalline and only show the presence of the fluorite phase as determined by XRD. The formation of the ferroelectric perovskite phase starts after a temperature treatment at 700 °C. Additionally to the peaks of the perovskite SBT phase strong peaks of iridium oxide can be observed in the XRD patterns of structures annealed at 750 °C and 800 °C.

The value of the remanent polarization  $2P_r$  and coercive field strength are  $7\mu\text{C}/\text{cm}^2$  and 100 kV/cm, respectively. Fatigue is found to be as low as about 4% after  $10^9$  cycles.

## **Chapter 6 Conclusions**

The main objectives of this research have been to develop a low temperature liquid delivery metalorganic chemical vapor deposition process of ferroelectric materials for high density FRAM applications, and to investigate the structural and electrical properties of obtained materials. Two kinds of ferroelectric materials have been investigated as capacitor materials, namely PZT based and SBT based ferroelectric materials.

From the results and discussion given in previous chapters, the following conclusions can be made:

Highly oriented Ti-rich lead zirconate titanate (PZT) films have been successfully prepared on Ir/TiO<sub>2</sub>/SiO<sub>2</sub>/Si substrates at a low annealing temperature of 520 °C by a MOCVD processing. Their structural and electrical properties have been systematically investigated as a function of composition and annealing temperature.

Content of lead in the deposited films plays an important role for obtaining the PZT films with good ferroelectric properties. As-deposited films are amorphous if the concentration of the lead is lower than 20 at%. Annealing of the lead-poor films result in formation of non-ferroelectric pyrochlore phase, leakage currents in annealed films have been so high, that the hysteresis loop has an elliptical shape which is characteristic for “loose capacitors” which are distinguished by their rather high leakage current.

The films are polycrystalline and the formation of a second phase has been observed if content of lead has been too high. The XRD analysis shows that the second phase is lead oxide. In the case of a huge excess of lead the surface of the deposited films is very rough because leaf-shaped lead oxide crystals have grown. The films with such morphology of the surface are not acceptable for the fabrication of the test capacitors and, consequently, for further investigations of their electrical properties.

A negligible excess of lead has been necessary to stabilize the perovskite structure in the deposited PZT films. As mentioned above, in the case of an excess of lead the formation of the lead oxide phase in the deposited films occurs. The XPS analysis and the SEM investigations show that the formation of the lead oxide phase has taken place only at the film surface and has a partial character. After annealing at 520 °C PZT films are preferentially (110) oriented and no second phase can be observed.

Since the volatility of PbO rapidly increases at 600 °C, after annealing of the PZT films at 600 °C a peak appears in the XRD spectra which corresponds to the pyrochlore phase. The pyrochlore phase is formed in the case of a lead deficiency; annealing at higher temperatures leads to the decrease of Pb and, therefore, to an increase of the pyrochlore phase in the films.

Both, an excess and a deficiency of Pb result in inferior ferroelectric properties so that careful control of all parameters of the fabrication process is essential.

The PZT films on Ir/TiO<sub>2</sub>/SiO<sub>2</sub>/Si substrate exhibit good ferroelectric properties. The remanent polarization has a value of 60 μC/cm<sup>2</sup> and coercive electric field a value of 200 kV/cm. The leakage current density at an applied voltage of 150 kV/cm is as low as 1·10<sup>-6</sup> A/cm<sup>2</sup>.

SrBi<sub>2</sub>Ta<sub>2</sub>O<sub>9</sub>, which is one of the bismuth layered-structure compounds, has been successfully prepared on Ir-coated Si and Si (100) substrates at the low processing temperature of 450 °C by liquid delivery metalorganic chemical vapor deposition (LD-MOCVD).

The ferroelectric test capacitors have showed excellent dielectric, insulating, and ferroelectric properties. The dielectric constant does not show any appreciable dispersion with frequency up to about 1 MHz indicating good ferroelectric/electrode-barrier/Si interfacial characteristics.

The typically measured  $2P_r$  and  $E_c$  values are 7 μC/cm<sup>2</sup> and 100 kV/cm, respectively, at an applied electric field of 500 kV/cm. At this field strength, the leakage current density is lower than 10<sup>-6</sup> A/cm<sup>2</sup>. SrBi<sub>2</sub>Ta<sub>2</sub>O<sub>9</sub> films exhibit high dielectric constants of about 300. The switching degradation of the polarization state has been found to be less than 4 % after about 10<sup>9</sup> polarization reversing switching cycles.

The SBT thin films prepared on Ir-coated silicon substrates show a random orientation of their crystalline grains over the whole composition range. SBT films prepared on Si (100) by simple MOCVD technique have not exhibited ferroelectricity, which might be attributed to the extrinsic stress and extremely small grains.

Low processing temperature at 450 °C, good structural, insulating, and ferroelectric properties of SBT thin films are promising results for the further integration of ferroelectric SBT capacitors in the ultra large scale integrated non-volatile random access memory cell structures.

## 7 References

- [1] J. F. Scott and C. A. Paz de Araujo, "Ferroelectric Memories" *Science*, **246**, 1400 (1989).
- [2] S. Y. Lee, D. J. Jung, Y. J. Song, B. J. Koo, S. O. Park, H. J. Cho, S. J. Oh, D. S. Hwang, S. I. Lee, J. K. Lee, Y. S. Park, I. S. Jung and K. Kim: *VLSI Tech. Symp.*, 141 (1999).
- [3] J. F. Scott, IEICE Trans., "Limitations on ULSI FeRAMs", *Electron*, Vol E81-C, No. **4**, 488 (1998).
- [4] H. Toyoshima and H. Kobatake, "Features and Applications of FeRAMs", NEC Research and Development, Vol 40, No. **2**, 206 (1989).
- [5] J. Scott: Ferromagnetic memories *Physics World* February, 4650 (1995).
- [6] B. Jaffe, W. R. Cook Jr., and H. Jaffe, *Piezoelectric Ceramics*, Academic Press (1971).
- [7] S. B. Desu, P. C. Joshi, X. Zhang, and S. O. Ryu, *Appl. Phys. Lett.* **71**, 1041 (1997).
- [8] T. Hase, T. Noguchi, and Y. Miyasaka, *Integrated Ferroelectrics*, **16**, 29 (1997).
- [9] S. Zafar, V. Kaushik, P. Laberge, P. Chu, R. E. Jones, R. L. Hance, P. Zurcher, B. E. White, D. Taylor, B. Melnick, and S. Gillespie, *J. Appl. Phys.* **82** (9), 4469 (1997).
- [10] "FRAM Quality & Reliability" a review, Fujitsu Limited (2001).
- [11] J. Moulson, J. M. Herbert, *Electroceramics*, published by Chapman & Hall, London (1996).
- [12] B. Jaffe, W. R. Cook, Jr., and H. Jaffe, *Piezoelectric Ceramics*, Academic, New York, (1971).
- [13] S. Zahi, R. Bouaziz, N. Abdessalem, A. Boutarfaia, *Ceram. Int.*, **29**, 35–39 (2003).
- [14] S. Zhao, H. Wu, Q. Sun, *Materials Science and Engineering B*, **123**, 203–210 (2005).
- [15] N. Tohge, S. Takahashi, and T. Minami, *J. Am. Ceram. Soc.*, **74**, 67 (1991).
- [16] K. Nagashima, M. Aratani, and H. Funakubo, *J. Appl. Phys.*, **89**, 4517 (2001).
- [17] K. Sreenivas, M. Sayer, and P. Garret, *Thin Solid Films*, **172**, 251 (1989).
- [18] J. Cheng, W. Zhu, N. Li, and L. E. Cross, *J. Appl. Phys.*, **91**, 5997 (2002).
- [19] Y. Sakashita, T. Ono, H. Segawa, K. Tominaga, and M. Okada, *J. Appl. Phys.*, **69**, 8352 (1991).
- [20] H. Watanabe, T. Mihara, and C. Paz de Araujo, *ISIF 92 Proceedings*, 139 (1992).
- [21] M. Dubois, P. Muralt, D. V. Taylor, and S. Hiboux, *Integr. Ferroelectr.*, **22**, 535 (1998).
- [22] J. Yang, L. Jianbin, *Sensors and Actuators A*, **121**, 103 (2005).

- 
- [23] E. Bouyssou, R. Jerisian, N. Cezac, P. Leduc, G. Guegan, C. Anceau, *Materials Science and Engineering B*, **118**, 28 (2005).
- [24] C.C. Mardare, E. Joanni, A.I. Mardare, J.R.A. Fernandes, C.P.M. de Sá and P.B. Tavares, *Applied Surface Science*, **243**, 113 (2005).
- [25] X.-S. Li, T. Tanaka, and Y. Suzuki, *Thin Solid Films*, **375**, 91 (2000).
- [26] C.A. Paz de Araujo, J.D. Cuchiaro, L.D. McMillan, M.C. Scott and J.F. Scott, *Nature* (London) **374**, p.627 (1995).
- [27] S.B. Desu and D.P. Vijay, *Mater. Sci. Engng. B*, **32**, p.75 (1995).
- [28] B. Aurivillius, *Arkiv Khemi*, **1**, 463 (1949).
- [29] E. C. Subbarao, *J. Amer. Ceram. Soc.*, **45**, 166 (1962).
- [30] H. Watanabe, T. Mihara, H. Yoshimori and C. A. Paz de Araujo, *Jpn. J. Appl. Phys.*, **34**, 5240 (1995).
- [31] K. Amanuma, T. Hase, and Y. Miyasaka, *Appl. Phys. Lett.*, **66**, 221 (1995).
- [32] P. Y. Chu, R. E. Jones, P. Zurcher, D. J. Taylor, B. Jiang, S. J. Gillespie, Y. Y. Li, M. Kottke, P. Fejes, and W. Chen, *J. Mater. Res.*, **11**, 1065 (1996).
- [33] A. D. Rae, J. G. Thompson, and R. L. Withers, *Acta. Cryst. Sec. B: Struc. Sci.*, **48**, 418 (1992).
- [34] H. Bachhofer, F. Hintermaier, M. Hauf, O. Spindler, T. Haneder, C. Dehm, R. Wasser, *Mater. Res. Soc. Symp. Proc.*, 596 (2000).
- [35] J. Ricote, M. L. Calzada, A. Gonzales, C. Ocal, *J. Amer. Ceram. Soc.*, **87**, 143 (2004).
- [36] T. Nakamura, Y. Nakao, A. Kamisawa and H. Takasu: *Jpn. J. Appl. Phys.*, **33**, 5207 (1994).
- [37] K. Numata, K. Aoki, Y. Fukuda and A. Nishimura: *Electron. Lett.*, **29**, 2099 (1993).
- [38] K. Aoki, Y. Fukuda, K. Numata and A. Nishimura: *Jpn. J. Appl. Phys.*, **34**, 5250 (1995).
- [39] D. J. Jung, S. Y. Lee, B. J. Koo, Y. S. Hwang, D. W. Shin, J. W. Lee, Y. S. Chun, S. H. Shin, M. H. Lee, H. B. Park, S. I. Lee, K. Kim, and J. G. Lee: *VLSI Tech. Symp.*, 122 (1998).
- [40] B. Yang, Y. M. Kang, S. S. Lee, K. H. Noh, N. K. Kim, S. J. Yeom, N. S. Kang, and H. G. Yoon: *Int. Electron Device Meet. Tech. Dig.*, 791 (2001).
- [41] F. Chu and G. Fox: *Integr. Ferroelec.*, **33**, 19 (2001).
- [42] X. Zheng, Y. Zhou, and Z. Yan, *Materials Research*, **6**, 551 (2003).
- [43] K. Torii, H. Kawakami, H. Miki, K. Kushida, and Y. Fujisaki: *J. of Appl. Phys.*, Vol. **81**, 2755-2759 (1997).
-

- 
- [44] C.C. Chang, J. H. Wang, M. D. Jeng, C. C. Lin, AND K. H. Chen: *Proc. Natl. Sci. Counc. ROC(A)*, Vol. **24**, No. 4, 287-292 (2000).
- [45] H. Kidoh, T. Ogawa, H. Yashima, A. Morimoto, and T. Shimizu: *Jpn. J. Appl. Phys.*, Vol. **31**, 2965-2967 (1992).
- [46] C. S. Park, S. W. Kim, G. T. Park, J. J. Choi, and H. E. Kim: *J. Mater. Res.*, Vol. **20**, No. 1, (2005).
- [47] H. Funakubo and T. Ozeki: *Key Engineering Materials*, Vol. **248**, 57-60 (2003).
- [48] A. C. Jones, T. J. Leedham, J. Brooks and H. O. Davies: *J. Phys. IV (France)*, **9**, 553 (1999).
- [49] F. Maury: *Chem. Vapor Deposition*, **2**, 113 (1996).
- [50] A. C. Jones, T. J. Leedham, P. J. Wright, M. J. Crosbie, D. J. Williams, H. O. Davies, K. A. Fleeting, P. O'Brien and M. E. Pemble: *Mater. Sci. Semicond. Processing*, **2**, 165 (1999).
- [51] M. Tiitta and L. Niinisto: *Chem. Vapor Deposition*, **3**, 167 (1997).
- [52] P. Kirilin, S. Bilodeau and P. Van Buskirk: *Integr. Ferroelectr.*, **7**, 307 (1995).
- [53] Handbook of Low and High Dielectric Constant Materials and Their Application, edited by H.S. Nalwa, Vol. **2**: Phenomena, Properties, and Applications, 130 (1999).
- [54] S.B. Desu, T. Shi, and C.K. Kwok, in *Chemical Vapor Deposition of Refractory Metals and Ceramics*, edited by T.M. Besmann and B.M. Gallois. *Mater. Res. Symp. Proc.*, Vol. **168**, 349 (1990).
- [55] EURO CVD 11 edited by M.D. Allendorf and C. Bernard. *Electrochem. Soc. Proc.*, **97** (25), 960 (1997).
- [56] R. Dat, J.K. Lee, O. Auciello, A.I. Kingon, *Appl. Phys. Lett.*, **67**, 572 (1995).
- [57] T. Li, Y. Zhu, S.B. Desu, C.H. Peng, M. Nagata, *Appl. Phys. Lett.*, **68**, 616 (1996).
- [58] S.S. Park, C.H. Yang, S.G. Toon, *J. Electrochem. Soc.*, **8**, 2855 (1997).
- [59] M. Huffman, *Integrated Ferroelectrics*, **10**, 39 (1995).
- [60] C. Isobe, T. Ami, K. Hironaka, K. Watanabe, M. Sugiyama, N. Nagel, K. Katori, C.D. Gutleben, M. Tanaka, H. Yamoto, H. Yagi, *Integrated Ferroelectrics*, **14**, 95 (1997).
- [61] J. Si, S.B. Desu, and C.Y. Tsai, *J. Mater. Res.*, Vol. **9**, No. 7, 1721 (1996).
- [62] G. Malandrino, F. Castelli, I.L. Fragala, *Inorg. Chim. Acta*, **224**, 203 (1994).
- [63] C.P. Fictorie, J.F. Evans, and W.L. Gladfelter, *J. Vac. Sci. Technol. A*, **12**, 1108 (1994).
- [64] M. Moert, T. Mikolajick, G. Schindler, N. Nagel, I. Kasko, W. Hartner, C. Dehm, H. Kohlstedt, R. Waser, *Thin Solid Films*, **473**, 328-334 (2005).

- 
- [65] Gas P, d'Heurle FM. In: Maex K, Rossum MV, editors. Properties of metal silicides. London: INSPEC, 279 (1995).
- [66] J.-D. Kim, K. Sasaki, T. Hata: *Vakuum*, **59**, 559-566 (2000).
- [67] Microanalysis of solids / edited by B.G. Yacobi, D.B. Holt, and L.L. Kazmerski, Plenum Press, New York, 1994.
- [68] W. Katz, *Proceedings of the 16<sup>th</sup> Annual Conference on Microbeam Analysis*, (R.G. Geiss, ed.), San Francisco Press, San Francisco, 1981.
- [69] J. F. Moulder, W. F. Stickle, P. E. Sobol, and K. D. Bomben, *Handbook of X-ray Photoelectron Spectroscopy*, Perkin Elmer, Eden Prairie, MN, 1992.
- [70] N. Wakiya, K. Kuroyanagi, Y. Xuan, K. Shinozaki, and N. Mizutani, *Thin Solid Films*, **372**, 156-162 (2000).
- [71] P. Verardi, F. Craciun, L. Mirengi, M. Dinescu, and V. Sandu, *Appl. Surf. Sci.*, **138-139**, 552-556 (1999).
- [72] J.N. Kim, K.S. Shin, D.H. Kim, B.O. Park, N.K. Kim, and S.H. Cho, *Appl. Surf. Sci.*, **206**, 119-128 (2003).
- [73] An introduction to X-ray crystallography / M.M. Woolfson – 2<sup>nd</sup> ed., Univeristy Press, Cambrige 1997.
- [74] C. B. Sawyer, and C. H. Tower, *Phys. Rev.*, **35**, 269 (1930).
- [75] A.C. Jones, P. O'Brien, *CVD of compound Semiconductors*, sixth ed., VCH Verlagsgesellschaft mbH, 23 (1997).
- [76] A.C. Jones, T.J. Leedham, P.J. Wright, *J. Mater. Chem.*, **8**, 1773 (1998).
- [77] H. Funakubo, K. Nagashima, K. Shinozaki, and N. Mizutani, *Thin Solid Films*, **368**, 261 (2000).
- [78] H. Funakubo, T. Hioki, K. Matsuyama, K. Shinozaki, and N. Mizutani, *J. Chem. Vap. Dep.*, **2**, 218 (1994).
- [79] S. Krumdieck, and R. Raj, *Surf. and Coat. Technol.*, **141**, 7 (2001).
- [80] B.C. Kang, S.B. Lee, and J.H. Boo, *Surf. and Technol.*, **131**, 88 (2000).
- [81] M. Cassir, F. Goubin, C. Bernay, P. Vernoux, and D. Lincot, *Appl. Surf. Sci.*, **193**, 120 (2002).
- [82] M. A. Cameron and S. M. George, *Thin Solid Films*, **348**, 90 (1999).
- [83] P.A. Coon, M.L. Wise, A.C. Dillon, M.B. Robinson and S.M. George. *J. Vac. Sci. Technol. B*, **10** 221 (1992).
- [84] M.L. Wise, O. Sneh, L.A. Okada and S.M. George. *J. Vac. Sci. Technol. B*, **13** 865 (1995).

- 
- [85] M. Putkonen, *Development of low-temperature deposition processes by atomic layer epitaxy for binary and ternary oxide thin films*, Helsinki University of Technology (2002).
- [86] T.J. Zhu, and L. Lu, *J. Appl. Phys.*, **95**, 241-247 (2004).
- [87] B.D. Qu, Y.G. Wang, W.L. Zhong, K.M. Wang, and Z.L. Wang, *J. Appl. Phys.*, **71**, 3467-3470 (1992).
- [88] N.J. Wu, A. Ignatiev, A.W. Mesarwi, H. Lin, K. Xie, and H.D. Shih, *Jpn. J. Appl. Phys.*, **32**, 5019-5023 (1993).
- [89] W.Y. Cheng, L.S. Hong, *Thin Solid Films*, **415**, 94 (2002).
- [90] C. Kwock and S. Desu, *Ceramic Transactions: Ferroelectric Films*, **25**, A. Bhalla, ed., ACS, Westerville, OH, 73-84 (1992).
- [91] C. Peng and S. Desu, *Mat. Res. Soc. Symp. Proc.*, **243**, 335 (1992).
- [92] A. H. Carim, B. A. Tuttle, D. H. Doughty, and S. L. Martinez, *J. Am. Ceram. Soc.*, **74**, 1455 (1991).
- [93] Z. Wang, Q. Jiang, G. S. White and A. K. Richardson, *Smart Mater. Struct.*, **7**, 867–873 (1998).
- [94] M. Hendrickson, T. Su, S. Trolier-McKinstry, B. Rod, and R. Zeto, *IEEE International Symposium on Applications of Ferroelectrics*, **2**, 683 (1996).
- [95] R.N. Torah, S.P. Beeby, and N.M. White, *Sensors and Actuators A*, **110**, 378 (2004).
- [96] J. S. Cross, K. Kurihara, N. Kamehara, H. Haneda and I. Sakaguchi, *Appl. Phys. Lett.*, **S 86**, 141909 (2005).
- [97] L. F. Schloss, H. Kim, and P. C. McIntyre, *J. Mater. Res.*, **19**, 1265 (2004).
- [98] J. F. Scott and M. E. Dawber, *Appl. Phys. Lett.*, **76**, 3801 (2000).
- [99] W. Zhu, Z.Q. Liu, W. Lu, M.S. Tse, H.S. Tan, and X. Yao, *J. Appl. Phys.*, **79**, 4283 (1996).
- [100] L.N. Chaplin, and S.A. Myers, *Mater. Res. Soc. Symp. Proc.*, **200**, 153 (1990).
- [101] T. Atsuki, N. Soyama, G. Sasaki, T. Yonezawa, K. Ogi, K. Sameshima, K. Hoshiba, Y. Nakao, and A. Kamisawa, *Jpn. J. Appl. Phys.*, **33**, 5196 (1994).
- [102] Y.H Lee, S.G. Park, I.G. Bae, and S.G. Lee, *Proceedings of 1998 International Symposium on Electrical Insulating Materials*, 35 (1998).
- [103] J.S. Vartuli, M. Özenbas, C.M. Chun, M. Trau, and I.A. Aksay, *J. Mater. Res.*, **18**, 1259 (2003).
- [104] N. Wakiya, K. Kuroyanagi, Y. Xuan, K. Shinozaki, and N. Mizutani, *Thin Solid Films*, **357**, 166 (1999).

- 
- [105] J.K. Lee, M.S. Lee, S. Hong, W. Lee, Y.K. Lee, S. Shin, and Y. Park, *Jpn. J. Appl. Phys.*, **41**, 6690 (2002).
- [106] J.S. Lee, and S.K. Joo, *Appl. Phys. Lett.*, **81**, 2602 (2002).
- [107] M. Dawber, and J. Scott, *Appl. Phys. Lett.* **76**, 1060 (2000).
- [108] S.B. Desu, D.P. Vijay, and I.K. Yoo, *Mat. Res. Soc. Symp. Proc.*, **335**, 53 (1994).
- [109] A.K. Tagantsev, I. Stolichnov, E.L. Colla, and N. Setter, *J. Appl. Phys.* **90**, 1387 (2001).
- [110] P.K. Larsen, G.J.M. Dormans, D.J. Taylor, and P.J. van Veldhoven, *J. Appl. Phys.* **76**, 2405 (1994).
- [111] H. Doi, T. Atsuki, *Jpn. J. Appl. Phys.*, **34**, 5105 (1995).
- [112] R. Büngener, PhD Thesis, *Diffusion von Strontium, Wismut und Tantal in Siliziumdioxid*, Mathematisch-Naturwissenschaftlich-Technischen Fakultät der Martin-Luther-Universität Halle-Wittenberg (2003).
- [113] Y.B. Park, K.Y. Min, K.J. Cho, S. Heo, C.H. Lim, M.K. Lee, T.K. Lee, H.J. Kim, S.Y. Lee, and Y.W. Kim, *J. Vac. Sci. Technol. A*, **19**, 916 (2001).
- [114] N. Nukaga, M. Mitsuya, T. Suzuki, Y. Nishi, M. Fujimoto, and H. Funakubo, *Jpn. J. Appl. Phys.*, **40** 5595 (2001).
- [115] J.S. Lee, H.J. Kwon, Y.W. Jeong, H.H. Kim, S.J. Hyun, and T.W. Noh, *Appl. Phys. Lett.*, **74**, 2690 (1999).
- [116] S.E. Jung, S.J. Hwang, and Y.M. Sung, *J. Cryst. Growth*, **254**, 92 (2003).
- [117] T. Osaka, A. Sakakibara, T. Seki, S. Ono, I. Koiwa, and A. Hashimoto, *Jpn. J. Appl. Phys.*, **37**, 597 (1998).
- [118] N. Nukaga, K. Ishikawa, and H. Funakubo, *Jpn. J. Appl. Phys.*, **38**, 5428 (1999).
- [119] J.H. Cho, S.H. Bang, J.Y. Son, and Q.X. Jia, *Appl. Phys. Lett.*, **72**, 665 (1995).
- [120] J. Lettieri, C.I. Weber, and D.G. Schlom, *Appl. Phys. Lett.*, **73**, 2057 (1998).
- [121] S.J. Hyun, B.H. Park, S.D. Bu, J.H. Jung, and T.W. Noh, *Appl. Phys. Lett.*, **73** (2518 (1998).
- [122] I. Koiwa, T. Kanehara, J. Mita, T. Iwabuchi, T. Osaka, S. Ono, and M. Maeda, *Jpn. J. Appl. Phys.*, **35**, 4946 (1996).
- [123] M. Takahashi, M. Noda, and M. Okuyama, *J. Appl. Phys.*, **94**, 6729 (2003).
- [124] P. Yang, N. Zhou, L. Zheng, H. Lu, and C. Lin, *J. Phys. D: Appl. Phys.* **30** 527 (1997).
- [125] I. Koiwa, Y. Okada, J. Mita, A. Hashimoto, and Y. Sawada, *Jpn. J. Appl. Phys.*, **36**, 5904 (1997).

- [126] C. A. Paz de Araujo, J. D. Cuchiaro, L. D. McMillan, M. C. Scott, and J.F. Scott, *Nature* (London) **374**, 627 (1995).
- [127] A. Li, D. Wu, H. Ling, T. Yu, M. Wang, X. Yin, Z. Liu and N. Ming, *Thin Solid Films*, **375**, 215-219 (2000).

## **Danksagung**

An dieser Stelle möchte ich allen danken, die mich bei der Erstellung dieser Arbeit unterstützt haben. Mein erster und ganz besonderer Dank geht an Prof. Dr. Edmund P. Burte, der das Projekt nicht nur exzellent betreute, sondern mir in der vorbildlichen Manier eines Doktorvaters mit Rat und Tat vielfach beistand.

Grossen Dank dem Prof. Dr. Frank T. Edelmann (Institut für Chemie) für seine Freundlichkeit uns Bismut Precursoren synthetisieren.

Ich bedanke mich auch bei Dr. Marco Lisker der mich in diese Arbeit eingeweiht hat und mir ständig zur Seite stand mit Rat und Antwort. Durch persönliche Wärme sowie tiefgründige Fachkenntnisse brachte er mir den Dialog und eine breite Verständigung des MOCVD-Processes nahe. Entscheidend für die mannigfaltigen Qualitäten der Arbeit waren seine konstruktive Kritik, die wertvollen methodischen Hinweise und ein stets offenes Ohr für meine zahlreichen unkonventionellen Vorschläge in diesem Dissertationsprojekt.

Dr. Mindaugas Silinskas danke ich herzlich für die wertvollen und freundlichen Gespräche sowie für die entscheidende Unterstützung bei Realisierung der Performance.

Ein besonderes Dankeschön geht auch an Herrn Bodo Kalkofen für seine Unterstützung im Kolloquium und die interessierten Nachfragen sowie für wertvolle Hinweise jenseits meines Interessengebiets.

Jörg Vierhaus danke ich für seine praktische Hilfsbereitschaft und logische sowie logistische Unterstützung. Mein Dank geht auch an die hier nicht erwähnten MitarbeiterInnen und KollegInnen am Institut, und an der Fakultät.

An alle meine Kollegen in verschiedenen Arbeitskreisen geht ein dickes Dankeschön für ihre Gesellschaft und Solidarität.

Mein abschließender Dank geht an meine Eltern und meine Familie für ihre Unterstützung meiner vielfachen Entwicklungen und ihren Glauben an mich.

Einem jeden Doktoranden und Menschen wünsche ich insgesamt eine ähnlich herausfordernde, kreative und unterstützende Arbeitsumgebung sowie warme Gesellschaft. Es gibt nach wie vor kein wirklich objektgerechtes Dankbarkeitsmedium.

**Lebenslauf**

Name: Matichyn, Serhiy

Geburtsdatum: 14.07.1979

Staatsangehörigkeit: ukrainisch

Familienstand: verheiratet

Ausbildung: 1996-2000 Lwiw Polytechnik Staatsuniversität Ukraine,  
Fakultät für Elektrophysik,  
Lehrstuhl Halbleitertechnologie,  
Bachelor

2000-2001 Lwiw Polytechnik Nationaluniversität Ukraine,  
Fakultät für Elektrophysik,  
Lehrstuhl Halbleitertechnologie,  
Master (Diplom)

01.01.2002-  
01.05.2002 Wissenschaftlicher Mitarbeiter in Labor für  
magnetischen Sensoren,  
Lehrstuhl Halbleitertechnologie,  
Fakultät für Elektrophysik,  
Lviv Polytechnic National University Ukraine

07.05.2002 Wissenschaftlicher Mitarbeiter am Institut für  
Mikro- und Sensorsysteme (IMOS),  
Lehrstuhl Halbleitertechnologie,  
Fakultät für Elektrotechnik,  
Otto-von-Guericke-Universität Magdeburg

01.01.2004-  
31.08.2006 Doktorand an der Otto-von-Guericke-Universität  
Magdeburg, Institut für Mikro- und Sensorsysteme  
(IMOS), Lehrstuhl Halbleitertechnologie,  
Fakultät für Elektrotechnik,  
Promotionsstipendium des Landes Sachsen-Anhalt

Magdeburg, 26.07.2006

Serhiy Matichyn